Experimental tests of quantum nonlinear dynamics in atom optics

2003 J. Opt. B: Quantum Semiclass. Opt. 5 R83

(http://iopscience.iop.org/1464-4266/5/2/202)

INSTITUTE OF PHYSICS PUBLISHING JOURNAL OF OPTICS B: QUANTUM AND SEMICLASSICAL OPTICS

J. Opt. B: Quantum Semiclass. Opt. **5** (2003) R83–R120 PII: S1464-4266(03)54868-6

PhD TUTORIAL

Experimental tests of quantum nonlinear dynamics in atom optics

Winfried K Hensinger, Norman R Heckenberg, Gerard J Milburn and Halina Rubinsztein-Dunlop

Centre for Biophotonics and Laser Science, Department of Physics, The University of Queensland, Brisbane, Queensland 4072, Australia

E-mail: hensinge@physics.uq.edu.au

Received 27 September 2002, in final form 2 February 2003
Published 3 April 2003
Online at stacks.iop.org/JOptB/5/R83

Abstract

Cold atoms in optical potentials provide an ideal test bed to explore quantum nonlinear dynamics. Atoms are prepared in a magneto-optic trap or as a dilute Bose–Einstein condensate and subjected to a far detuned optical standing wave that is modulated. They exhibit a wide range of dynamics, some of which can be explained by classical theory while other aspects show the underlying quantum nature of the system. The atoms have a mixed phase space containing regions of regular motion which appear as distinct peaks in the atomic momentum distribution embedded in a sea of chaos. The action of the atoms is of the order of Planck's constant, making quantum effects significant. This tutorial presents a detailed description of experiments measuring the evolution of atoms in time-dependent optical potentials. Experimental methods are developed providing means for the observation and selective loading of regions of regular motion. The dependence of the atomic dynamics on the system parameters is explored and distinct changes in the atomic momentum distribution are observed which are explained by the applicable quantum and classical theory. The observation of a bifurcation sequence is reported and explained using classical perturbation theory. Experimental methods for the accurate control of the momentum of an ensemble of atoms are developed. They use phase space resonances and chaotic transients providing novel ensemble atomic beamsplitters. The divergence between quantum and classical nonlinear dynamics is manifest in the experimental observation of dynamical tunnelling. It involves no potential barrier. However a constant of motion other than energy still forbids classically this quantum allowed motion. Atoms coherently tunnel back and forth between their initial state of oscillatory motion and the state 180° out of phase with the initial state.

Keywords: Mechanical effects of light on atoms, optical cooling of atoms, trapping, quantum chaos, tunnelling, Bose–Einstein condensate

1. Introduction

1.1. Quantum nonlinear dynamics and quantum chaos

Quantum nonlinear dynamics is an exciting field of modern physics investigating the quantum nature of dynamical systems. One of the key questions is what happens to classical motion in the quantum world. In fact the quantum–classical correspondence for dynamical systems is still unclear and a subject of discussion. Part of quantum nonlinear dynamics is the study of 'quantum chaos' [1]. It is the desire to

understand the quantum mechanical origin of the observed chaos which drives this area of research. The field of quantum chaos was born in 1917 when Albert Einstein tried to unravel which mechanical systems could be subjected to the Bohr–Sommerfeld–Epstein quantization rules [2]. He concluded that, in the absence of invariant tori in phase space, these quantization rules cannot be used and that, moreover, this absence applies to most systems. Chaos is associated with a rapid divergence of arbitrarily close points in phase space [3]. Classical chaos can be described as the emergence of complexity on infinitely fine scales in classical phase space. Until recently it was argued that there could be no such thing as chaos in quantum physics as an infinitely fine level of detail is needed to describe the trajectories of a classical chaotic system and it was thought that quantum mechanics structure is smoothed away in an area below the size of $\hbar$ [3, 4] as Heisenberg's uncertainty relation requires the product of position and momentum uncertainties in a measurement of both these quantities to be larger than Planck's constant[1]. However, only very recently it has been shown that even features in the phase space of a system that are distinctly smaller than Planck's constant can have an effect on the dynamics of a system [5]. During the years since the birth of quantum chaos, significant amounts of theory have been created to give a better description of chaotic physical systems in a quantum dynamical context. In 1970 Gutzwiller succeeded in semiclassically quantizing a classical chaotic system using his approach, known as periodic orbit theory [6]. Bohigas was able to obtain a universal relationship between the statistical properties of the spectra of a quantum system and the dynamics of the corresponding classical chaotic system using random matrix theory [7, 8], which was originally developed for nuclear physics [9, 10].

The key question in quantum chaos is, what happens to classical chaos in the quantum world? One approach is to seek generic features of quantum dynamics for a system whose classical description exhibits chaotic dynamics. An example of such features is dynamical localization, a quantum suppression of classical diffusion, which was discovered by Fishman *et al* [11] in numerical studies of the periodically kicked quantum rotor. Conductance fluctuations in ballistic micro-structures associated with complex electron trajectories constitute another example of the occurrence of quantum chaos [12]. Finally, molecular excitation experiments can show interesting quantum features (e.g. Anderson localization, an effect related to dynamical localization) if the scaled Planck's constant $\bar{k}$ (see section 2.4) is kept finite but exhibit chaotic dynamics in the classical limit ($\bar{k} = 0$) [13]. To gain a different perspective on the quantum nature of classical chaos some experiments look at the manifestations of classical chaos in wave propagation. Chaotic systems are often so complicated that they defy intuitive understanding. Therefore it is helpful to choose relatively simple systems which exhibit chaos. One example is billiards. A ball on a pool-hall table does not exhibit chaotic motion. However, if one adds a circular rail which is placed at the centre of the table the dynamics become chaotic. This can be illustrated by the fact that two trajectories with different initial conditions diverge at a rate that is exponential. Using a microwave cavity one can simulate a quantum billiard system because the time-independent wave equation, the Helmholtz equation, is mathematically equivalent to the time-independent Schrödinger equation for a particle trapped inside a two-dimensional potential with infinitely high walls, a billiard [14]. In billiard-shaped cavities eigenfrequencies and eigenfunctions can be measured by microwave absorption. In 1991 quantum scars, which are concentrations of probability along periodic orbits, were experimentally observed by Sridhar [15]. The idea of chaos participating in tunnelling phenomena was first introduced by Lin and Ballentine in 1990 [16] and further developed by Tomsovic and Ullmo [17], who termed it 'chaos-assisted tunnelling'. The first experimental evidence for chaos-assisted tunnelling in a microwave annular billiard was observed by Dembowski *et al* [18] utilizing a superconducting cavity. This observation was predicted earlier by Frischat and Doron [19]. In chaos-assisted tunnelling a state which is localized on the classical chaotic phase space region can interact with the tunnelling doublet (two states of opposite parity) resulting in an enhanced tunnelling rate. Chaos-assisted tunnelling for the driven pendulum was studied by Latka *et al* [20] and later for a cold-atom-driven pendulum implementation by Mouchet *et al* [21]. Experiments to study the quantum dynamics of classically chaotic systems have been carried out on Rydberg atoms, measuring microwave ionization of highly excited hydrogen atoms [22, 23]. The potentials involved in the Rydberg-atom ionization experiments are hard to approximate by one-dimensional potentials. At present the three-dimensional quantum simulations needed for these highly excited atoms are not feasible without severe approximations [23]. In the Rydberg-atom experiments the Coulomb potential dictates the dynamics and the system is complicated due to electron–electron interactions (the chaotic trajectory of the outer electron in a Rydberg atom can closely approach the shell of inner electrons). One result of these experiments is the recognition of different regimes determined by how well classical and quantum mechanics agree with each other. These regimes are characterized by the scaled microwave frequency given by $\Omega_0 = n_0\Omega$, where n_0 is the principal quantum number of the initial state and Ω is the microwave frequency.

1.2. Cold atom experiments

1.2.1. Cold atoms in optical lattices. This tutorial shows how experiments on cold atoms in optical lattices can be used to study quantum nonlinear dynamics. There are many different effects that can occur when atoms are subjected to a standing wave of light. A standing wave can be used to diffract atoms to act as a coherent beamsplitter [24]. This interaction is similar to Bragg diffraction of light by a crystal [25] and is used for interferometry applications. Anderson *et al* [26] have used cold atoms in a standing wave to demonstrate an effect similar to the AC Josephson effect. In this experiment the interference of atoms tunnelling through light potentials was observed. To observe a Wannier–Stark ladder Raizen's group has subjected cold atoms to a phase modulated accelerating standing wave [27]. Distinct peaks in the spectrum of the

[1] It has also been argued that there cannot be chaos in quantum mechanics because the Schrödinger equation is linear. This argument is misleading as the corresponding classical equation, the Liouville equation, is also linear.

first excited state population as a function of the modulation frequency correspond to resonant excitation of atoms to the first excited (unbound) band of the standing wave wells. An accelerating standing wave was utilized to separate bound and unbound atoms. Quantum state preparation and a one-dimensional optical lattice of double wells were proposed and experimentally implemented by Deutsch, Jessen and his group [28, 29]. Most recently quantum computing using a neutral atom optical lattice has been proposed [30] and evaluated [31]. Only very recently the transition from superfluidity to the Mott insulator phase was observed using a Bose–Einstein condensate which is held in a three-dimensional optical lattice [32]. In the insulating phase exact numbers of atoms are localized at individual lattice sites with no phase coherence across the lattice.

1.2.2. Quantum nonlinear dynamics with cold atoms. It was first proposed by Graham *et al* [33] to use atom manipulation experiments to experimentally investigate quantum nonlinear dynamics and quantum chaos. Atoms in optical potentials provide an ideal test bed to explore quantum nonlinear dynamics and the effects of decoherence. The de Broglie wavelength of cold atoms is sufficiently large that the wave nature of atoms needs to be taken into consideration when analysing their dynamics. There are many advantages of using cold atoms to study quantum nonlinear dynamics. Firstly, the potentials that are used are extremely well approximated as one-dimensional potentials, which makes an accurate theoretical description feasible. Secondly, in atom optics there is considerable control over the potentials. One can tailor the potentials to match the theoretical description and, indeed, achieve simple nonlinear potentials such as the nonlinear pendulum which will be considered in more detail in this tutorial. One can also achieve a considerable variety of modulation dynamics. Finally, dissipation and noise can be made insignificant by operating at low temperatures and operating far from the atomic resonance frequency. Hence atom optical systems can be well approximated by Hamiltonian dynamics. The system can be isolated from the environment providing a good approximation of a closed quantum system. This enables the observation of quantum effects and provides the exciting possibility to learn about controlling decoherence by introducing it in a defined way into the system.

Laser-cooled atoms moving in far-off-resonant optical dipole potentials have provided a clean and versatile experimental context for the investigation of the quantum dynamics of nonlinear Hamiltonian systems. Previous work [34–37] has demonstrated the ability to achieve non-dissipative dynamics in the quantum domain with well controlled time-dependent potentials. Sinusoidal potentials with a periodically modulated phase were used [33, 34] to achieve quantum localization of the momentum, a quantum suppression of chaotic diffusion. Trajectories of atoms can interfere destructively hindering the atomic diffusion. Dynamical localization can be observed by measuring the kinetic energy of atoms as a function of the number of kicks (periods of the phase modulation). While classically one would expect to observe linear growth proportional to the classical diffusion constant, it is observed in the experiment that, after the 'quantum break time', the measured energy stops growing, in agreement with the quantum prediction. In this system decoherence was applied in a controlled way using amplitude noise and spontaneous emission which was induced using near-resonant optical molasses [38, 39]. It was found that both factors led to the destruction of dynamical localization. Therefore decoherence might be the link between the classical and quantum worlds, validating the quantum–classical correspondence principle. A detailed comparison was made of the classical phase space structure and quantum dynamics with experiments, as a function of the driving strength, in the work of Robinson *et al* [36] for cold atoms in a phase modulated standing wave. In particular, momentum distributions were observed that are due to atoms being trapped in a central region of regular motion at the origin of momentum–position phase space. Experiments to test the resonance overlap criteria where atoms were subjected to an amplitude modulated standing wave for one modulation period [37] showed that the phase space changed from globally stable to chaotic. This could be concluded from an analysis of the atomic momentum distribution. Subsequently a close approximation to the δ-kicked rotor was implemented by using an amplitude modulated standing wave [35, 38]. The atoms were subjected to a periodic sequence of short pulses of a standing wave, with the pulse width much shorter than the repetition period. Effectively this corresponds to broadband amplitude modulation centred on the pulse frequency. Ghose *et al* [40] proposed atomic motion in magneto-optic double-well potentials as a testing ground for quantum chaos. Preliminary evidence for coherent tunnelling in a double well was reported by Deutsch *et al* [29]. Entanglement between the internal and motional degrees of freedom provided means to access the tunnelling dynamics by Stern–Gerlach measurements of the ground state magnetic population.

1.3. Rationale and structure

This tutorial presents an investigation into the dynamics of cold atoms moving in a sinusoidal optical dipole potential with amplitude modulation at a single frequency. This corresponds to the classical driven pendulum, a paradigm for the study of quantum nonlinear dynamics and quantum chaos. One of the most fascinating phenomena considered in this tutorial is the experimental observation of dynamical tunnelling. Both experimental and theoretical results are presented, illustrating the dynamics of the driven pendulum. One of the key questions considered here is whether classical physics can accurately describe the experiments and to what extent quantum mechanics is required to understand and explain the dynamics of the driven pendulum in atom optics. By conducting experiments and analysing them in the framework of quantum and classical physics this question will be addressed. To gain a better insight into the correspondence of quantum and classical nonlinear dynamics, it is of considerable interest to conduct an experiment where one can vary and control the effective Planck's constant of the system, taking the system from the classical to the quantum regime. As will be shown in section 2.4 the effective Planck's constant $\bar{k}$ provides a measure of how 'quantum' the system behaves on a given timescale. The classical limit is given by $\bar{k} = 0$. As will be explained in section 2.4, the effective Planck's

constant for the driven pendulum is inversely proportional to the modulation frequency of the standing wave, which can be varied to investigate the transition from the classical to the quantum regime. This is one of the reasons for using the atom-optics-driven pendulum to investigate the divergence of quantum and classical physics.

Distinct quantum features of the driven pendulum are known. Dyrting and co-workers [41] made a theoretical study of cold atoms that are subjected to a single-frequency amplitude modulated standing wave. They predicted quantum tunnelling between two phase space resonances for this system, (in this case two oscillatory regular motions), a process referred to as dynamical tunnelling (for a detailed description of phase space resonances see section 2.3). Atoms can coherently tunnel from one region of regular motion to another. To do this the atoms have to cross Kolmogorov, Arnold and Moser (KAM) surfaces (see section 2.3), a process that is forbidden classically [42, 43]. Atoms tunnel from one kind of oscillatory motion to an oscillatory motion which is 180° out of phase with their initial motion. Dynamical tunnelling was accomplished and will be discussed in section 9. The experimental realization of dynamical tunnelling opens up a fundamental test bed for quantum nonlinear dynamics. It is not energy but a different constant of motion which classically forbids dynamical tunnelling. For most tunnelling phenomena which have been observed in the past, for example α-particle decay, conservation of energy forbids the process classically. Furthermore, Hug and Milburn [44] showed that quantum mechanical velocity predictions for phase space resonances disagree by up to 20% with classical predictions in the atom-optics-driven pendulum. Experimental results which may possibly be linked to this phenomenon will be discussed in section 5.

Section 2 introduces the set-up for the experiments with a rubidium magneto-optic trap (MOT) and provides an overview of important concepts which are needed to understand the fundamental aspects of the system. Section 3 provides the theoretical framework for the experiments. In particular, quantum trajectory and master equation simulations are introduced. The work described in this tutorial investigates whether classical Hamiltonian perturbation theory can accurately describe the dynamics qualitatively when the scaled Planck's constant and the timescales are sufficiently small. To do that, atomic momentum distributions which result from phase space resonances are analysed and theoretical predictions are presented. An overview of the resonance dynamics is given for different parameter regimes in order to characterize the atomic dynamics qualitatively and quantitatively. A surprising range of dynamics arises which will be described in detail in section 4. In section 5 an experimental and theoretical study of the classical phase space structure, and its bifurcations, is carried out as a function of the system parameters, providing another test of quantum and classical nonlinear dynamics. In the experiments, a bifurcation sequence is observed as distinct peaks in the atomic momentum distribution which appear and disappear when one of the control parameters of the system is changed. It will be shown that the observation of multiple bifurcations can be explained by classical Hamiltonian theory.

Quantum dynamics can be applied to develop new methods to manipulate cold atoms. An optical standing wave can be used to manipulate atoms and prepare them to have a certain momentum and momentum spread or to produce an atomic beamsplitter. Experimental implementations using the driven pendulum dynamics or chaotic transients resulting in efficient momentum phase space preparation and ensemble beamsplitting methods will be introduced in section 6.

In order to observe dynamical tunnelling experimentally, methods needed to be developed to load regions of regular motion selectively and to observe long term dynamics. Details of the set-up along with experimental results are shown in section 7. Most of the experiments which are presented in this tutorial were carried out at the University of Queensland using a rubidium MOT. However, to observe dynamical tunnelling unambiguously it is important to be able to access lower temperatures than possible with a standard MOT. Therefore some of the experiments were carried out using a sodium Bose–Einstein condensate (at the National Institute of Standards and Technology in Gaithersburg, MD, USA). The experimental set-up for these measurements is described in section 8 and results are presented in section 9.

2. The driven pendulum in atom optics

2.1. Experimental set-up for the experiments with cold Rb atoms

In order to explore the dynamics of cold atoms in an optical standing wave a standard MOT is utilized. A more detailed description of the set-up can be found in [45]. In the experiments rubidium atoms are cooled down to a temperature of around 8 μK (corresponding to a $1/e$ momentum spread of 13 recoil momenta). The pressure in the vacuum chamber is around 10^{-9} Torr. The magnetic field coils produce a magnetic field gradient of 10^{-1} T m^{-1} in an anti-Helmholtz configuration.

An injection locking scheme is utilized to decrease the linewidth of the trapping diode laser down to 100 kHz, while allowing all the power of the laser to be used in the trapping experiment [46, 47].

Around 10^6 rubidium atoms are polarization gradient cooled [48, 49] for 10 ms. Then the MOT is turned off but the repumping beam is left on so that the atoms accumulate in the $F = 3$ ground state. A period of 500 μs is implemented to allow for effective repumping. After the repumping has occurred the standing wave (to be described in detail below) is turned on for a precise duration and is intensity modulated using an acousto-optic modulator. Both the beginning and end phases of the amplitude modulation have to be carefully chosen as will be discussed in section 2.5. After the standing wave is switched off, the atoms undergo a period of ballistic expansion (between 3 and 20 ms). Following this, an image of the cloud is taken using a freezing molasses technique [35, 50]. In this technique the optical molasses is turned on again with the magnetic field still turned off. As a result of this, the atomic distribution is frozen at its current position and the fluorescence resulting from the 'frozen' atoms is viewed with a 16-bit charge coupled device (CCD) camera (Apogee AP7, 512 × 512). The CCD array of the camera is cooled, leading to a quantum efficiency of around 80% and a RMS read noise of 6.7 electrons. The experiment is repeated multiple times

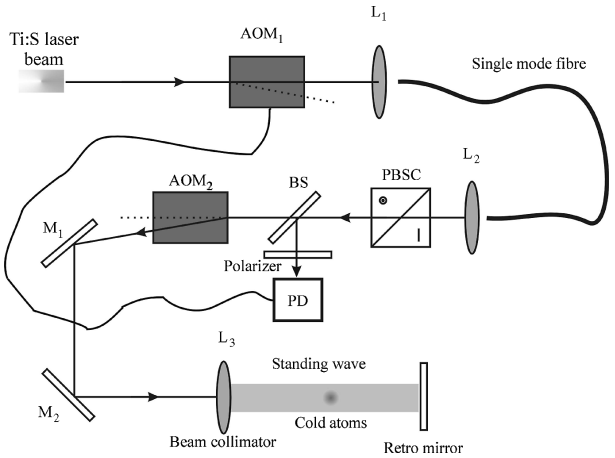

Figure 1. Set-up which is used to produce the optical standing wave. A titanium:sapphire laser beam is fed through a single-mode polarization preserving fibre which is used to optimize the pointing stability and to improve the quality of the laser beam. The acousto-optic modulator AOM_1 and the photodetector PD are used to stabilize the light intensity of the standing wave. The polarizing beamsplitter cube PBSC is used to keep the direction of linear polarization in the standing wave constant. AOM_2 provides the light intensity modulation.

with different ballistic expansion times to allow a statistical measurement of the velocity of the atoms with high precision.

The experimental set-up for the optical standing wave is shown in figure 1. The standing wave is produced using a frequency stabilized titanium:sapphire ring laser (Ti:S, Coherent 899-21). This laser produces up to 2.7 W of light at 780 nm with a linewidth of less than 1 MHz and a frequency drift of approximately 50 MHz h^{-1}. To reduce the intensity noise, polarization noise and pointing instability to less than 1% the following technique is implemented. The Ti:S beam is first passed through an 80 MHz acousto-optic modulator (denoted AOM_1 in figure 1) and the zeroth-order beam is fed into a polarization preserving single-mode optical fibre. Part of the output beam from the fibre is leaked through a mirror and through a polarizer to a photodetector, which gives an electronic feedback signal to acousto-optic modulator AOM_1 on the other end of the fibre to compensate for light intensity fluctuations. In the experiments the intensity of the optical standing wave is modulated. Acousto-optic modulator AOM_2 (as seen in figure 1) produces an intensity modulation of the form $I_0(1-2\varepsilon\sin(\omega t+\phi))$, where ε is the depth of modulation, ω is the modulation angular frequency, I_0 is the unmodulated intensity and ϕ determines the start phase of the amplitude modulation. After the light has passed through acousto-optic modulator AOM_2 and the vacuum chamber the beam quality is regularly monitored in the far field utilizing a lens to expand the beam to ensure that a clean Gaussian profile is maintained. To test the spectral purity of the modulated standing wave the modulated light wave was observed on a fast photodetector and subsequent Fourier analysis of this signal indicated a spectral impurity of about 1 part in a thousand. The light after AOM_2 was collimated to a $1/e$ width of 2.85 mm (in some experiments 3.25 mm). The width was chosen so it would be maximized, but also sufficiently small so that the resulting light intensity was large enough to provide the required value of the scaled well depth κ (well depth of the standing wave, see section 2.2) when the detuning from the atomic resonance is sufficiently large for the adiabatic elimination (see section 3.1) to hold. The beam passes through the vacuum chamber and through the atomic cloud and is retroreflected to form the one-dimensional periodic optical potential.

There are several procedures to centre the beam on the cloud. In one method the light frequency is tuned close to the spectral resonance of the trapped atoms. The beam is then moved until it blows the trapped atoms out of the centre of the trap, which can be observed on a CCD camera. This is good for rough alignment. The light is then further detuned and the alignment is improved by ensuring that all the atoms are blown out of the trap again. Subsequent iterations of this procedure lead to a precise alignment of the incoming beam. The retroreflection is aligned using an aperture located far away from the retro mirror just before the output of the single-mode polarization preserving fibre. A beamsplitter, located right between the aperture and fibre output, reflects light only if the retroreflection passes through the aperture. The alignment of the retroreflection was measured to be good to approximately 0.02°. The variation of the scaled well depth κ over the extent of the atomic cloud was determined to be approximately 2% by measuring the $1/e$ beam diameter of the standing wave and the size of the atomic cloud. The final maximum irradiance of the standing wave in the region of the atomic cloud is of the order of 12 W cm^{-2}. A telescope before acousto-optic modulator AOM_2 is used to decrease the beam diameter and therefore to increase the efficiency of the modulator. Using another telescope after acousto-optic modulator AOM_2, the beam diameter is controlled and the beam is carefully collimated. The whole experiment is computer controlled using the LabVIEW programming environment and a GPIB interface.

2.2. The fundamental Hamiltonian

As described above the experiments are carried out using cold rubidium atoms (or sodium atoms, see section 8) which are positioned in a far detuned optical standing wave. The one-dimensional system can be described in the corresponding two-dimensional phase space which is spanned by momentum and position coordinates along the standing wave. Single-frequency modulation of the intensity of the standing wave leads to an effective Hamiltonian for the centre-of-mass motion (a thorough derivation will be given in section 3) given by

$$H = \frac{p_x^2}{2m} + \frac{\hbar\Omega_{\text{eff}}}{4}(1 - 2\varepsilon\sin(\omega t + \phi))\sin^2(kx) \qquad (1)$$

where the effective Rabi frequency is $\Omega_{\text{eff}} = \Omega^2/\delta$, $\Omega = \Gamma\sqrt{I/I_{\text{sat}}}$ is the resonant Rabi frequency, ε is the modulation parameter, ω is the modulation angular frequency, Γ is the inverse spontaneous lifetime, δ is the detuning of the standing wave, t is the time, p_x is the momentum component of the atom along the standing wave and k is the wavenumber. Here I is the spatial mean of the intensity of the unmodulated standing wave (which is half of the peak intensity) so $\Omega = \Gamma\sqrt{I_{\text{peak}}/2I_{\text{sat}}}$ and $I_{\text{sat}} = hc\Gamma/\lambda^3$ is the saturation intensity. λ is the wavelength of the standing wave. ϕ determines the start

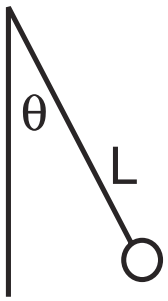

Figure 2. Classical pendulum, consisting of a point mass m suspended at the end of a rigid (but massless) rod of length L. θ is the angle relative to the stable equilibrium position.

phase of the amplitude modulation. Using scaled variables [35] the Hamiltonian is given by

$$\mathcal{H} = p^2/2 + 2\kappa(1 - 2\varepsilon \sin(\tau + \phi)) \sin^2(q/2) \tag{2}$$

where $\mathcal{H} = (4k^2/m\omega^2)H$, $q = 2kx$ and $p = (2k/m\omega)p_x$. The driving amplitude is given by

$$\kappa = \omega_r \Omega_{\text{eff}}/\omega^2 = \frac{\hbar k^2 \Omega_{\text{eff}}}{2\omega^2 m} = \frac{4U_0\omega_r^2}{\omega^2}, \tag{3}$$

where $\omega_r = \hbar k^2/2m$ is the recoil frequency, $\tau = t\omega$ is the scaled time variable and U_0 is the well depth in units of $\hbar\omega_r$. The commutator of scaled position and momentum is given by

$$[p, q] = \mathrm{i}\bar{k}, \tag{4}$$

where the scaled Planck's constant is $\bar{k} = 8\omega_r/\omega$. The first term in equation (2) corresponds to the kinetic energy and the second one corresponds to the potential energy whose amplitude is modulated in time, hence $\mathcal{H}$ is not conserved.

To see the connection of this Hamiltonian to a classical pendulum one can consider a point mass m suspended at the end of a rigid (but massless) rod of length L as shown in figure 2. The rod is free to pivot about an axis at the other end of the rod. The Hamiltonian of this classical pendulum is given by

$$\mathcal{H} = \frac{p^2}{2m} + mgL(1 - \cos\theta) \tag{5}$$

where θ is the angle relative to the stable equilibrium position and g is the acceleration due to gravity. The first term is the kinetic energy and the second term is the potential energy. Using a trigonometric identity this can be rewritten as

$$\mathcal{H} = \frac{p^2}{2m} + 2mgL \sin^2\frac{\theta}{2}. \tag{6}$$

It can be easily seen from the above equation that the effective Hamiltonian for the centre-of-mass motion of cold atoms in an modulated standing wave given in equation (2) is equivalent to that of a classical driven pendulum where the length of the pendulum L or the acceleration due to gravity g is modulated in time.

2.3. The classical picture

Jules Henri Poincaré invented a very convenient means to analyse the phase space of a driven dynamical system utilizing

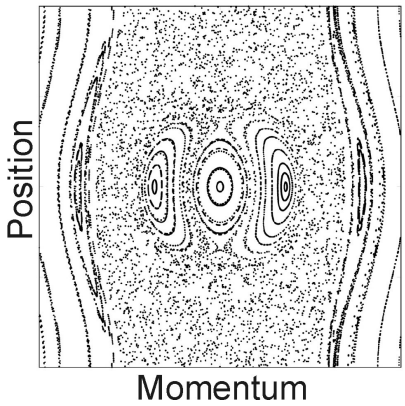

Figure 3. Poincaré section for a classical particle in an amplitude-modulated optical standing wave. Momentum and position (one well of the standing wave) of the particle along the standing wave are plotted stroboscopically, with the stroboscopic period being equal to the modulation period. The central region near the origin consists of small amplitude motion. Chaos (dotted region) separates this region from two period-1 regions of regular motion (represented in the Poincaré section as sets of closed curves) located left and right of the centre along position $q = 0$. Further out in momentum are two stable regions of motion known as librations. At the edges are bands of regular motion corresponding to above barrier motion.

classical equations, known as a Poincaré section [43]. This classical picture treats atoms as point objects without the inherent position and momentum width that is required in quantum mechanics by Heisenberg's uncertainty relation. Momentum and position of a particle inside each well in the direction of the standing wave are plotted stroboscopically, with the stroboscopic period being equal to the modulation period for different initial position and momentum coordinates (randomly spread initial conditions). The dynamics are calculated using Hamilton's equations:

$$\frac{\mathrm{d}q}{\mathrm{d}t} = \frac{\partial\mathcal{H}}{\partial p} \tag{7}$$

$$\frac{\mathrm{d}p}{\mathrm{d}t} = -\frac{\partial\mathcal{H}}{\partial q}. \tag{8}$$

Figure 3 shows a Poincaré section for the driven pendulum. A particle can exhibit either chaotic or regular motion. Which type of motion applies depends on the particle's initial position in phase space. The presence of closed curves in the Poincaré section indicates the existence of KAM surfaces [42, 43, 51]. The KAM theorem states that, if a previously integrable system is made slightly non-integrable by inclusion of a small perturbation, then some phase space tori (in particular those where the ratio of the natural nonlinear frequency of the unperturbed system to the modulation frequency is irrational) survive but may be deformed. The crossing of these surfaces by an atom is forbidden by classical mechanics [43]. Two islands of regular motion appear in the Poincaré section as a set of closed curves right and left of the centre of the section and correspond to atoms which oscillate in phase with the standing wave modulation. The period of a region of regular motion determines how many modulation periods it takes for the atoms to complete one oscillation period and return to their initial position. In this case they are period-1 regions of regular

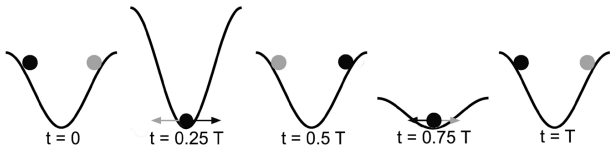

Figure 4. Diagram of period-1 resonances for atoms in an amplitude modulated sinusoidal potential. The black and the grey ball each corresponds to an atom contained in one of the two period-1 resonances. The position of these atoms is shown for fractions of one modulation period. The resonances correspond to atomic motion that remains in phase with the modulation frequency. The period-1 character of motion becomes apparent as the atoms take one modulation period to return to their initial position. The anharmonicity of the sinusoidal potential is compensated by the amplitude modulation for atoms around these resonances, creating the regions of regular period-1 motion shown in figure 3. T is the modulation period and t is the time.

motion, because a particle located inside takes one modulation period to complete one oscillation period inside the well. Each of the two period-1 regions of regular motion corresponds to a group of atoms oscillating in phase with the standing wave but they differ in that they oscillate 180° out of phase relative to each other. A graphic representation of this motion is shown in figure 4. In the Poincaré section the closed rings making up the islands of regular motion are centred around a point known as the phase space resonance. A particle positioned on a phase space resonance will return to exactly the same phase space coordinate after one oscillation period. Particles that are part of the island of regular motion will return after one oscillation period to phase space coordinates located on the same closed curve from which they had started (a closed curve in the Poincaré section represents a KAM surface). The inner island of regular motion corresponds to atoms that are approximately stationary at the bottom of the well. The sea of chaotic motion (dotted region) corresponds to atoms bouncing chaotically inside the well and it is bounded in momentum by the region of regular unbound motion that consists of atoms having enough kinetic energy to travel from one well of the standing wave to the next. The islands of regular motion near the region of unbound regular motion are librations: atoms which take multiples of one modulation period to hop from one well to another, constantly moving in the same direction. The size and position of the islands of regular motion depend very strongly on the system parameters. Using scaled variables the phase space depends only on the scaled well depth κ and the modulation parameter ε.

Phase space resonances and regions of regular motion are distinct features of the dynamics of the driven pendulum. They are the origin of distinct peaks in the atomic momentum distribution, as will be discussed in section 2.5. Resonances and their associated islands of regular motion have also been seen in other physical systems. For example, they have been reported in plasma physics. Sinclair, Hosea and Sheffield [52] mapped a toroidal magnetic field in a stellarator using phase stabilized electrons. Islands of stability emerged in the phase space dynamics of the electrons. In fluid flow experiments particle motion in the fluid was shown to have chaotic and regular phase space regions [53]. In experiments on microwave ionization of Rydberg atoms strong classical resonance effects in the final-bound-state quantum number distribution were found by Bayfield and Sokol [54].

2.4. The scaled Planck's constant

To understand the nature of the atomic dynamics it is best to estimate first when they can be explained classically and when one has to use a full quantum simulation to successfully predict the experiments. How 'quantum' the system behaves on a given timescale depends on the magnitude of the scaled Planck's constant $\bar{k}$ [33] for the system. The scaled Planck's constant can be rewritten as

$$\bar{k} = \frac{4\hbar k^2}{\omega m} = 4\hbar\frac{4\pi^2}{\lambda^2\omega m} = 2\hbar\pi\left(\frac{1}{\frac{\lambda}{2}\left(\frac{\lambda}{2T}m\right)}\right) = \frac{2\hbar\pi}{2\pi I_0} = \frac{\hbar}{I_0} \tag{9}$$

where T is the modulation period, $\hbar$ is Planck's constant, λ is the wavelength and I_0 is the action of a free particle over the distance $\lambda/2$ in the time T. The action of the system, multiplied by 2π, is given by the area in phase space that is encircled by the trajectory of a particle. $\bar{k}$ can therefore be interpreted as the ratio of Planck's constant to the action of a particle in the system described. If the phase space area of a region of regular motion is of the same order as $\hbar$ we know that Heisenberg's uncertainty relation forbids simulation of the dynamics using classical trajectories but it rather requires the atoms to be treated as wavepackets. Thus $\bar{k}$ will indicate in which regime the experiment is carried out. Therefore there is some minimum order of magnitude of $\bar{k}$ which must be exceeded before one expects to see significant differences between quantum and classical dynamics on a given timescale. The timescales τ_Q where the expectation value of some observable begins to show noticeable deviation from the classical evolution scale with the inverse logarithm of the scaled Planck's constant in classical chaotic systems ($\tau_Q \propto \ln(1/\bar{k})$) while classically regular systems scale as an inverse polynomial of the scaled Planck's constant ($\tau_Q \propto (1/\bar{k})^\alpha$, with α being an integer) [55]. Quantum effects are therefore much easier to observe in classical chaotic systems as they occur on much shorter timescales.

Decoherence is the mechanism where a closed quantum system is coupled to the environment [55, 56]. It has been argued that decoherence can produce a smooth quantum-to-classical transition in nonlinear dynamical systems [57]. Quantum effects can be observed only if decoherence is kept to a minimum. The magnitude of the detuning of the standing wave from the atomic transition will determine the amount of decoherence introduced into the system because the less the standing wave is detuned the more incoherent transitions (e.g. spontaneous emission) will occur. Other sources of decoherence (or mechanisms that act like decoherence) include spectral, phase and amplitude noise of the standing wave but have been found to be negligible or will be discussed in later sections.

2.5. Loading and observation of atoms in a region of regular motion

The concept of loading atoms into a region of regular motion and subsequently observing them is of key importance for the experimental realization of the driven pendulum in atom optics. The fundamental ideas will be illustrated utilizing the example of period-2 regions of regular motion. Atoms inside such a region take two modulation periods to complete one

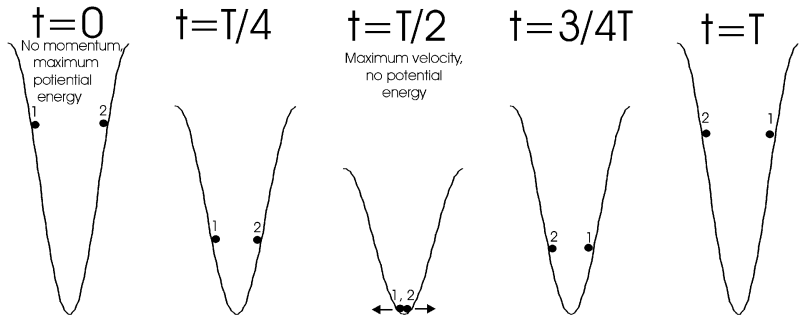

Figure 5. Diagram of period-2 resonances for atoms in an amplitude modulated sinusoidal potential. Groups 1 and 2 correspond to atoms contained in the period-2 regions of regular motion (located left and right of the island of regular motion at the origin in the Poincaré section in figure 3). The position of these two groups as well as the potential is shown for four phases of the modulation. Atoms that are part of the regions of regular motion start with zero velocity at the top of the potential well. After half of the modulation period they have reached the bottom of the well and have reached their maximum velocity.

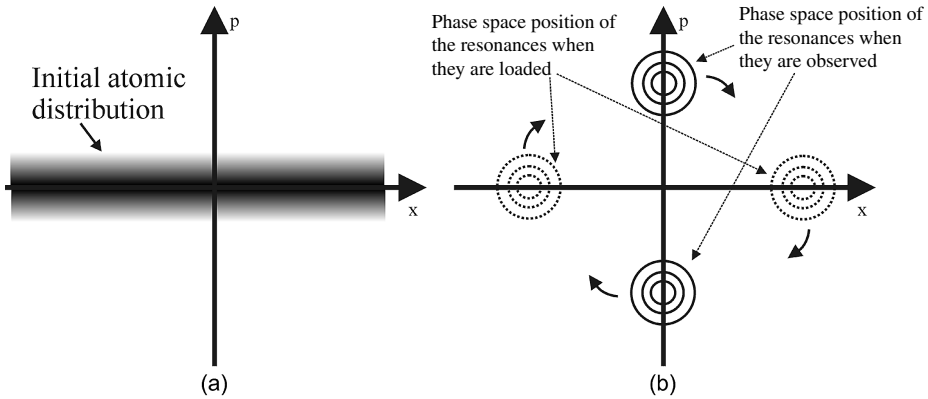

Figure 6. Part (a) shows the initial distribution of the atoms in phase space. The pictures illustrates that the resonances need to be placed on the position axis for effective loading to occur. The position of the resonances for loading and observation in phase space can be seen in (b). To be able to resolve the regions of regular motion using a CCD camera it is important that the resonances have maximum velocity. Therefore they should be located on the momentum axis for observation.

oscillation and return to their initial position. The sinusoidal well does not constitute a harmonic potential. Therefore the oscillation frequency is a function of the initial position of the particle. Atoms whose position inside the well corresponds to an oscillation frequency in the unmodulated well equal to half of the modulation frequency are contained in a resonance. Figure 5 shows the optical potential for four different phases (fractions of a modulation period) of the intensity modulation. The two balls correspond to atoms contained in each of the two period-2 resonances. Atoms are randomly spaced inside the potential well with zero mean momentum when the standing wave is turned on (figure 6(a)). To load the two period-2 regions of regular motion the start phase of the amplitude modulation is chosen so that the regions of regular motion are located on the position axis, as shown at $t = 0$ in figure 5 and in the corresponding Poincaré section in figure 6(b). The initial atomic distribution shown in figure 6(a) has maximum overlap with the regions of regular motion for the appropriate starting phase. For period-2 resonances the appropriate starting phase is maximum modulation amplitude. (For period-1 resonances the appropriate starting phase is zero modulation amplitude, with the amplitude either increasing or decreasing.) Atoms that were loaded into either region of regular motion oscillate inside the well (groups 1 and 2 in figure 5 correspond to atoms contained in the region of regular motion). After one modulation period atom groups 1 and 2 have exchanged their positions (after half a modulation period for period-1 resonances). Atoms whose initial position corresponds to an oscillation frequency which vastly differs from half the modulation frequency will not be part of this regular motion but will be part of a different phase space feature, e.g. they will bounce chaotically inside the potential well and will form the chaotic background of atoms in the atomic momentum distribution. After the atoms have interacted with the modulated standing wave for a selected number of modulation periods, the standing wave is turned off at such a time that the atoms inside the region of regular motion are at the bottom of the well having maximum velocity. The appropriate interaction time is $n + \frac{1}{2}$ periods of the modulation (n is an integer) for a period-2 region of regular motion (and $n + \frac{1}{4}$ or $n + \frac{3}{4}$ periods of the modulation for a period-1 region of regular motion). The atomic position distribution is imaged after sufficient time of free flight. At that time atoms belonging to different islands of regular motion will have spatially separated. In fact the position distribution after sufficient free evolution corresponds approximately to the momentum distribution before the evolution. This has been observed when conducting theoretical simulations (see section 3.2.4).

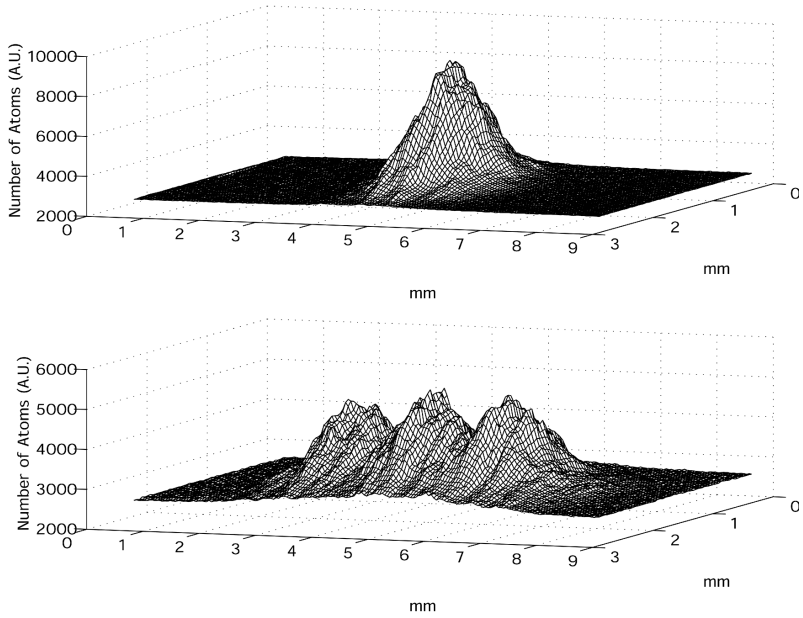

Figure 7. Spatial distributions of the atoms obtained after a 10 ms ballistic expansion interval. The upper distribution results when no interaction potential is applied. The lower distribution shows three distinct peaks in the atomic position distribution in which the atoms have interacted for 7.5 modulation periods with a $\omega/2\pi = 500$ kHz, $\varepsilon = 0.13$, $\kappa \approx 0.5$ modulated standing wave (scaled Planck's constant $\bar{k} = 0.06$). The peaks result from two period-2 islands of regular motion and the central island of stability.

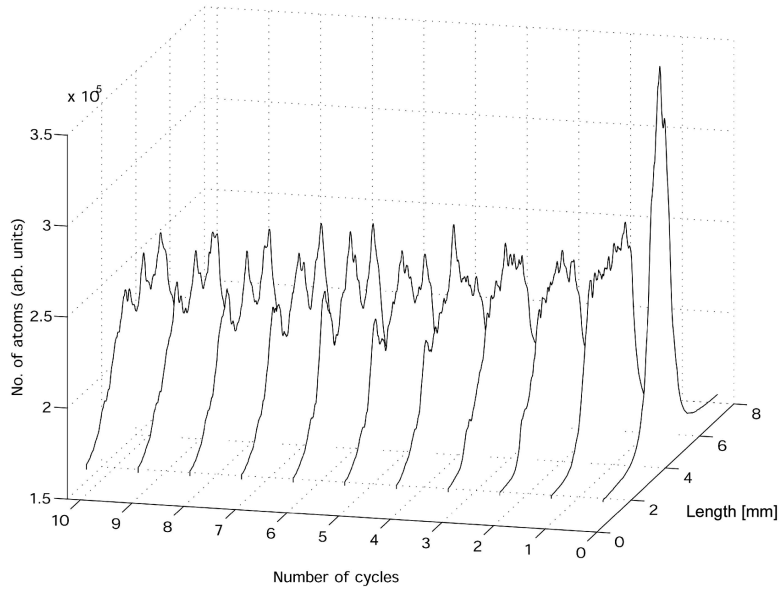

Figure 8. Phase space resonances as a function of the interaction time with the modulated standing wave measured in modulation periods. Resonances start to emerge after 4.5 modulation periods (cycles). These data were obtained at modulation frequency $\omega/2\pi = 500$ kHz, modulation parameter $\varepsilon = 0.13$ and scaled well depth $\kappa \approx 0.5$. The resonances move with approximately 22 recoil momenta.

Ballistic expansion is applied to resolve the dynamics of the atoms as it is impossible to observe the spatial position of the atoms in each individual well. Exact velocity measurements can be made by taking pictures of the distribution after different times and calculating the distance the resonances have moved during that time.

Figure 7 shows spatial distributions obtained after a 10 ms ballistic expansion interval. The upper distribution results when no interaction potential is applied. The lower distribution shows peaks in the atomic momentum distribution that correspond to period-2 regions of regular motion. Here the atoms interact for 7.5 modulation periods with the standing wave (using modulation frequency $\omega/2\pi = 500$ kHz, modulation parameter $\varepsilon = 0.13$ and scaled well depth $\kappa \approx 0.5$).

Why do regions of regular motion constitute peaks in the atomic momentum distribution? Immediately after the loading phase, when the atomic density inside the chaotic region is equal to the density inside the islands of regular motion (both equal to the initial atomic density), regions of regular motion do not constitute a feature in the atomic momentum distribution. However, after sufficient time, atoms in the chaotic region can spread over a larger volume (filling the entire chaotic region)

which leads to a smaller atomic density in the chaotic region. This results in a significant atomic-number signal-to-noise ratio between the regions of regular motion and the chaotic region in the atomic momentum distribution. One needs to wait for approximately 4.25 cycles for the atoms to distribute so that the resonances can be observed. This is apparent in both the experiment and the theoretical simulations. When this has occurred resonances can emerge from the background of the chaotic region. Figure 8 shows the emergence of peaks in the atomic momentum distribution corresponding to the resonances as a function of the interaction time with the standing wave measured in modulation periods. These data were taken for modulation frequency $\omega/2\pi = 500$ kHz, modulation parameter $\varepsilon = 0.13$ and scaled well depth $\kappa \approx 0.5$. One can see that the resonances start to emerge at 4.5 cycles and then remain stable.

3. Theoretical description of the driven pendulum in atom optics

3.1. The quantum master equation

Quantum mechanically, the state of the system is described by a density operator ρ. In order to describe spontaneous emission as well as the motion induced by the standing wave it is necessary to use a quantum master equation [58]. Considering only motion in the direction of the standing wave, and working in the interaction picture, it is given by

$$\dot{\rho} = -\frac{\mathrm{i}}{\hbar}[H, \rho] + \Gamma\mathcal{L}_1\rho. \tag{10}$$

Here H is the Hamiltonian for the centre-of-mass and internal state of the atom, given by

$$H = \frac{p_x^2}{2m} + \hbar\delta\sigma^\dagger\sigma + \frac{\hbar}{2}[\Omega(x,t)\sigma^\dagger + \Omega^\dagger(x,t)\sigma]. \tag{11}$$

Here $\Omega(x,t)$ is the position- and time-dependent Rabi frequency operator for the atom in the standing wave and δ is the detuning of the standing wave. The atomic operators are defined in terms of $\sigma = |a\rangle\langle b|$, where $|a\rangle$ and $|b\rangle$ correspond to ground and excited states, respectively.

The superoperator $\mathcal{L}_1$ describes the incoherent evolution due to the coupling to the vacuum field modes at rate Γ and is given by

$$\mathcal{L}_1 = \int \mathrm{d}^2\vec{n}\,\phi(\vec{n})\mathcal{D}[\mathrm{e}^{\mathrm{i}kn_x x}\sigma]. \tag{12}$$

Here k is the wavenumber of the spontaneously emitted light, $\vec{n}$ is a unit vector describing the direction of the spontaneously emitted photon and $\phi(\vec{n})$ is the dipole radiation distribution for this direction:

$$\phi(\vec{n}) = \frac{3}{8\pi}\left(1 - \frac{(\vec{d}\cdot\vec{n})^2}{\vec{d}\cdot\vec{d}}\right), \tag{13}$$

where $\vec{d}$ is the atomic dipole vector. The superoperator $\mathcal{D}$ is defined for arbitrary operators A and B by

$$\mathcal{D}[A]B \equiv ABA^\dagger - (A^\dagger AB + BA^\dagger A)/2. \tag{14}$$

Only the x component n_x appears in the superoperator in equation (12) because only motion in the x direction is of importance for the experiments. This is the direction of propagation of the light beams, so the dipole vector (which is parallel to the polarization vector of the light) is perpendicular to the x direction. This enables the integral in equation (12) to be simplified to

$$\mathcal{L}_1 = \int \mathrm{d}u\, W(u)\mathcal{D}[\mathrm{e}^{\mathrm{i}kux}\sigma], \tag{15}$$

where

$$W(u) = \begin{cases} \frac{3}{8}(1+u^2) & \text{for } |u| \leqslant 1 \\ 0 & \text{for } |u| > 1. \end{cases} \tag{16}$$

Note that u can be interpreted as the x component of the momentum kick to the atom, in units of $\hbar k$.

To derive the equations that are simulated by the quantum trajectory simulations discussed in section 3.2.2 a technique is used similar to that introduced by Graham *et al* [33] for a similar system, but a more complete derivation is given here, including justifications for the approximations made using the parameters of the experiment. The resulting equations are related to those of Dyrting and Milburn [59], but they are derived using a different technique and include different approximations.

The master equation (10) for the two-level atom in a light field can be written as

$$\dot{\rho} = \Gamma\left(\mathcal{B}\sigma\rho\sigma^\dagger - \frac{1}{2}\{\sigma^\dagger\sigma, \rho\}\right) - \frac{\mathrm{i}}{2}[\Omega(x,t)\sigma^\dagger + \sigma\Omega^\dagger(x,t), \rho] - \mathrm{i}\delta[\sigma^\dagger\sigma, \rho] - \frac{\mathrm{i}}{2\hbar m}[p^2, \rho], \tag{17}$$

where, for an arbitrary operator R,

$$\mathcal{B}R = \int \mathrm{d}^2\,\vec{n}\phi(\vec{n})\mathrm{e}^{\mathrm{i}kn_x x}R\mathrm{e}^{-\mathrm{i}kn_x x}. \tag{18}$$

Explicitly using the internal state basis a, b one obtains

$$\dot{\rho}_{aa} = \Gamma\mathcal{B}\rho_{bb} - \frac{\mathrm{i}}{2}[\Omega^\dagger(x,t)\rho_{ba} - \rho_{ab}\Omega(x,t)] - \frac{\mathrm{i}}{2\hbar m}[p^2, \rho_{aa}], \tag{19}$$

$$\dot{\rho}_{ab} = -\frac{\Gamma}{2}\rho_{ab} - \frac{\mathrm{i}}{2}[\Omega^\dagger(x,t)\rho_{bb} - \rho_{aa}\Omega^\dagger(x,t)] + \mathrm{i}\delta\rho_{ab} - \frac{\mathrm{i}}{2\hbar m}[p^2, \rho_{ab}], \tag{20}$$

$$\dot{\rho}_{bb} = -\Gamma\rho_{bb} - \frac{\mathrm{i}}{2}[\Omega(x,t)\rho_{ab} - \rho_{ba}\Omega^\dagger(x,t)] - \frac{\mathrm{i}}{2\hbar m}[p^2, \rho_{bb}]. \tag{21}$$

In a typical experiment $|\Omega(x,t)| \leqslant \Omega \approx 4.65 \times 10^9\ \mathrm{s}^{-1}$ and $\delta \approx 44 \times 10^9\ \mathrm{s}^{-1}$ ($\delta/2\pi \approx 7$ GHz). Thus the experiment is in the well-detuned regime where $\Omega \ll \delta$. As a result, most of the time the atom will be in the ground state with $\rho_{bb} \sim (\Omega/\delta)^2$, as will be shown. As long as one is not interested in evolution faster than on the timescale Γ^{-1}, one can slave ρ_{ab} and ρ_{bb} to ρ_{aa}. Specifically, it can be seen from equation (20) that ρ_{ab} will quickly come to equilibrium (at a rate $\Gamma/2$) with respect to the value of ρ_{aa}, which evolves slowly. Setting $\dot{\rho}_{ab} = 0$ thus gives

$$\rho_{ab} \simeq \frac{\mathrm{i}[\rho_{aa}\Omega^\dagger(x,t) - \Omega^\dagger(x,t)\rho_{bb}]}{\Gamma - 2\mathrm{i}\delta}. \tag{22}$$

Since $\Omega(x,t)$ is time-dependent, this expression can be valid only if the rate of decay, $\Gamma/2$, is much greater than the rate of variation of $\Omega(x,t)$. In a typical experiment $\Gamma/2 \simeq 19\times10^6\ \mathrm{s}^{-1}$ while the angular modulation frequency is typically an order of magnitude smaller and the recoil frequency is $3.8\times10^3\ \mathrm{s}^{-1}$. In deriving equation (22) it is also assumed that the kinetic energy is much less than $\hbar\delta$ and $\hbar\Gamma$ and so can be ignored compared to them. Since the $1/e$ momentum half-width is of the order of seven recoil momenta, the kinetic energy divided by $\hbar$ is of the order of $10^5\ \mathrm{s}^{-1}$. Thus the above assumptions are justified.

Substituting equations (22) into (21) and (19) gives the following coupled equations:

$$\begin{aligned}\dot\rho_{aa} = {}& \frac{1}{\Gamma^2+4\delta^2}\{\mathrm{i}\delta[\Omega^\dagger(x,t)\Omega(x,t),\rho_{aa}]\\ & -\Gamma\{\Omega^\dagger(x,t)\Omega(x,t),\rho_{aa}\}/2+\Gamma\Omega^\dagger(x,t)\rho_{bb}\Omega(x,t)\}\\ & -\frac{\mathrm{i}}{2\hbar m}[p^2,\rho_{aa}]+\Gamma\mathcal{B}\rho_{bb} \qquad (23)\end{aligned}$$

$$\begin{aligned}\dot\rho_{bb} = {}& \frac{1}{\Gamma^2+4\delta^2}\{-\mathrm{i}\delta[\Omega(x,t)\Omega^\dagger(x,t),\rho_{bb}]\\ & -\Gamma\{\Omega(x,t)\Omega^\dagger(x,t),\rho_{bb}\}/2+\Gamma\Omega(x,t)\rho_{aa}\Omega^\dagger(x,t)\}\\ & -\frac{\mathrm{i}}{2\hbar m}[p^2,\rho_{bb}]-\Gamma\rho_{bb}. \qquad (24)\end{aligned}$$

These are the equations which are simulated by the quantum trajectories in section 3.2.2.

The evolution described by the master equation (10) is not obviously related to that generated by the Hamiltonian (1). Most importantly, the real particle is an atom with two internal states whereas the ideal particle has no internal states. To see the relation between the two models it is necessary to adiabatically eliminate the upper level of the atom [60, 61]. It is most convenient to move into the interaction picture with respect to the ground-state potential $H_0=\frac{\hbar}{4\delta}\Omega(x,t)\Omega^\dagger(x,t)$ by defining the unitary transformation operator

$$U_0(t)=\mathrm{e}^{-\mathrm{i}H_0t} \qquad (25)$$

such that

$$\tilde\rho = U_0^\dagger(t)\rho U_0(t). \qquad (26)$$

This transformation is applied to the master equation (10). Using the same approximations as above one obtains after some calculation [61]

$$\begin{aligned}\dot\rho = {}& \frac{\Gamma}{\Gamma^2+4\delta^2}(\mathcal{B}\Omega^\dagger(x,t)\rho\Omega(x,t)-\tfrac12\{\Omega(x,t)\Omega^\dagger(x,t),\rho\})\\ & -\mathrm{i}\frac{\delta}{\Gamma^2+4\delta^2}[\Omega(x,t)\Omega^\dagger(x,t),\rho]\\ & -\frac{\mathrm{i}}{16\delta^3}[\Omega^4(x),\rho]-\frac{\mathrm{i}}{2\hbar m}[p^2,\rho]. \qquad (27)\end{aligned}$$

For the experimental parameters, the second-to-last term is only about 1% as large as the dominant Hamiltonian term that scales as Ω^2/δ, and can thus be safely ignored. For $\delta\gg\Gamma$ this equation is identical to equation (29).

The adiabatic elimination is valid only if the detuning δ is much greater than the maximum of the Rabi frequency $\Omega(x,t)$ which is valid for most of the experiments. In the experiment the modulated standing wave Rabi frequency has the form

$$\Omega(x,t)=\Omega\sqrt{1-2\varepsilon\sin\omega t}\,\sin kx, \qquad (28)$$

which gives the master equation

$$\dot\rho=-\frac{\mathrm{i}}{\hbar}[H,\rho]+\lambda\mathcal{L}_2\rho. \qquad (29)$$

Here the Hamiltonian is

$$H=\frac{p_x^2}{2m}+\frac{\hbar\Omega_{\mathrm{eff}}}{4}(1-2\varepsilon\sin\omega t)\sin^2(kx), \qquad (30)$$

which is the same as in equation (1), with $\Omega_{\mathrm{eff}}=\Omega^2/\delta$. The effective damping rate is $\lambda=\Gamma(\Omega/2\delta)^2$ and the superoperator $\mathcal{L}_2$ is

$$\lambda\mathcal{L}_2=\lambda\int\mathrm{d}u\,W(u)\mathcal{D}\big[\mathrm{e}^{\mathrm{i}kux}\sqrt{1-2\varepsilon\sin\omega t}\,\sin kx\big] \qquad (31)$$

$$=\frac{\Gamma}{\delta}\frac{\Omega_{\mathrm{eff}}}{4}(1-2\varepsilon\sin\omega t)\int\mathrm{d}u\,W(u)\mathcal{D}[\mathrm{e}^{\mathrm{i}k(u+1)x}-\mathrm{e}^{\mathrm{i}k(u-1)x}]. \qquad (32)$$

3.2. Simulation methods

To obtain reliable quantum simulations two different methods were developed. The atomic dynamics can be modelled using either the master equation or quantum trajectories. Quantum trajectories and the master equation are closely connected. In quantum trajectories an ensemble of states $|\psi_i\rangle$ is found using a stochastic Schrödinger equation (for example equation (45)). The resulting approximate density matrix ρ_{app} is given by

$$\rho_{\mathrm{app}}=\frac{1}{n}\sum_{i=1}^{n}|\psi_i\rangle\langle\psi_i|. \qquad (33)$$

where

$$\rho=\rho_{\mathrm{app}}+\mathrm{O}\Big(\frac{1}{\sqrt{n}}\Big). \qquad (34)$$

Both methods have been tested and found to give essentially identical results, strengthening the validity of the presented theory. Although this tutorial only contains simulations for the dynamics of cold atoms using quantum trajectories, a short summary of the master equation method is also presented. To allow a comparison with classical physics a method to obtain classical simulations is also presented. An introduction into simulation methods for the evolution of a Bose–Einstein condensate using the Gross–Pitaevskii equation will be given in [62].

3.2.1. Simulations using the master equation. Since the Hamiltonian given by equation (30) is periodic in x, it would be natural to consider using the momentum states as a basis for simulating the evolution. However, as the final expression (32) for $\mathcal{L}_2$ indicates, spontaneous emission following the absorption of a photon from the standing wave enables a transfer of momentum of any amount between $-2\hbar k$ and $+2\hbar k$ (because the momentum kick is projected onto the x axis). This means that an exact one-dimensional simulation of the master equation would require a dense set of momentum states.

In practice, this dense set is not necessary as the initial conditions have a finite momentum spread which will smear out any fine structure. In fact, the initial conditions in the experimental set-up (rubidium MOT) have a momentum

spread of order $7\hbar k$ which means that features of order $\hbar k$ are not resolvable. It therefore makes sense to approximate the continuous momentum transfer due to spontaneous emission by discrete momentum transfer in units of $\hbar k$ in order to take advantage of the symmetry of the Hamiltonian. This is achieved by replacing $\mathcal{L}_2$ by

$$\mathcal{L}_3 = (1 - 2\varepsilon \sin \omega t) \sum_{u=-1,0,1} V(u)\mathcal{D}[e^{ik(u+1)x} - e^{ik(u-1)x}], \tag{35}$$

where $V(u)$ is a discrete approximation to $W(u)$. This is similar to the approach of [63] but is more rigorous.

Approximating $W(u)$ by $V(u)$ is not a unique procedure. Here the method of choosing $V(u)$ such that the zeroth, first, and second moments agree is adopted. That is,

$$\int W(u)\,du = 1 = V(-1) + V(0) + V(1), \tag{36}$$

$$\int W(u)u\,du = 0 = -V(-1) + V(1), \tag{37}$$

$$\int W(u)u^2\,du = \tfrac{2}{5} = V(-1) + V(1). \tag{38}$$

The first condition here is just that V is normalized. The second is that V reproduces the correct mean momentum kick $\langle \Delta p \rangle$ in spontaneous emission (i.e. zero). The third is that V reproduces the correct mean squared momentum kick $\langle (\Delta p)^2 \rangle = (2/5)(\hbar k)^2$. The three conditions imply

$$V(-1) = \tfrac{1}{5}, \qquad V(0) = \tfrac{3}{5}, \qquad V(1) = \tfrac{1}{5}. \tag{39}$$

Under this approximation, the master equation in the momentum basis can be written as

$$\dot{\rho} = -\frac{i}{\hbar}[H, \rho] + \lambda \mathcal{L}_3 \rho, \tag{40}$$

where

$$H = \frac{1}{2m}\sum_n (p_0 + \hbar k n)^2 |n\rangle\langle n| + \frac{\hbar \Omega_{\text{eff}}}{16}(1 - 2\varepsilon \sin \omega t)(R^2 + L^2 - 2I), \tag{41}$$

where $|n\rangle$ is the momentum state $|p_0 + \hbar k n\rangle$ (where p_0 is an arbitrary momentum) and

$$\mathcal{L}_3 = \tfrac{1}{5}(1 - 2\varepsilon \sin \omega t)\{\mathcal{D}[R^2 - I] + 2\mathcal{D}[R - L] + \mathcal{D}[I - L^2]\}. \tag{42}$$

Here R is a unitary operator (corresponding to e^{-ikx}) which raises the momentum by $\hbar k$, and L (corresponding to e^{ikx}) similarly lowers it by $\hbar k$,

$$R = L^{-1} = L^\dagger = \sum_n |n+1\rangle\langle n| \tag{43}$$

and $I = \sum_n |n\rangle\langle n|$.

Since all of the operators in the master equation (40) can be represented by matrices in the $|n\rangle$ basis, it is a simple matter to solve the equation using a suitable numerical environment such as MATLAB. The initial-state matrix $\langle n|\rho(0)|n\rangle$ is found by assuming a Gaussian initial momentum distribution of $1/e$ half-width of $6.5\hbar k$ which forms the diagonal elements of $\rho(0)$. The different density matrices are evolved and the results are combined to gain a more accurate result. The final momentum distribution after an interaction time t is obtained by calculating

$$\langle n|\rho(t)|n\rangle \tag{44}$$

which is equal to the number of atoms having momentum $p_0 + \hbar k n$. To obtain smoother results a new set of momentum states is chosen, still spaced by $\hbar k$, but shifted in momentum by fractions of $\hbar k$ compared to the original set.

3.2.2. Simulations using quantum trajectories. Without making the approximations of adiabatic elimination of the upper level of the atom, and discretizing the spontaneous-emission recoil, it would be numerically intractable to solve the initial master equation (10). That is because of the size of the state matrix. However, it is possible to simulate the evolution of that equation stochastically, by taking a large ensemble of quantum trajectories for the state vector. This can be done as the number of elements of the state vector is roughly equal to the square root of the number of elements of the state matrix.

The theory of quantum trajectories [64] shows that it is possible to simulate incoherent transitions using Monte Carlo methods [59], so this was done to obtain the second quantum mechanical simulations. A stochastic Schrödinger equation developed for atom optics by Dum *et al* [65] and Mølmer *et al* [66] is used to include incoherent transitions.

Rather than simulate the exact dynamics of the original master equation (10) the approach introduced here follows Dyrting and Milburn [59] in simulating an approximate master equation. The approximate master equation (equations (23) and (24)) is similar to that of equation (29) in that the atom experiences a potential. However, it is potentially a better approximation than that equation because the excited state of the atom $|b\rangle$ is retained.

In the quantum jump simulations the atom is always in state $|b\rangle$ or $|a\rangle$, and the potential it sees depends on which state it is in. Thus the atom has a quantum centre-of-mass state $|\psi\rangle$ and an internal state which can be either a or b but not a superposition of both. One advantage of this approximation over the full master equation (10) is that it has a clear classical analogue, as will be discussed in section 3.2.3.

In the scaled units of equation (2), the stochastic equation for the state vector $|\psi\rangle$ is

$$\mathrm{d}|\psi\rangle = -\frac{i}{k}\,\mathrm{d}\tau\, K|\psi\rangle + \mathrm{d}N_1(\tau) \times \left(\frac{\sqrt{(1 - 2\varepsilon \sin \tau)}\sin(q/2)}{\langle\psi|[\sqrt{(1 - 2\varepsilon \sin \tau)}\sin(q/2)]^2|\psi\rangle} - 1\right)|\psi\rangle + \mathrm{d}N_2(\tau)\left(\frac{\exp(i\bar{p}q/k)}{\sqrt{\langle\psi|\psi\rangle}} - 1\right)|\psi\rangle. \tag{45}$$

Here the non-Hermitian effective Hamiltonian K depends on the internal state $\sigma = a, b$ of the atom:

$$K = \begin{cases} p^2/2 + 2\kappa(1 - 2\varepsilon \sin \tau)\sin^2(q/2)/\nu^* & \text{for } \sigma = a \\ p^2/2 - 2\kappa(1 - 2\varepsilon \sin \tau)\sin^2(q/2)/\nu & \text{for } \sigma = b \end{cases} \tag{46}$$

with

$$\nu = 1 - \frac{i\Gamma}{2\delta}. \tag{47}$$

The imaginary part of ν makes K non-Hermitian. The non-Hermitian part corresponds exactly to the anticommutator (the second term in the curly brackets) in equations (23) and (24). It causes the modulus of the wavefunction to decay. This is because the smooth evolution takes into account only what happens when there are no jumps. The Hermitian part of K corresponds exactly to the commutator (the first term in the curly brackets) in equations (23) and (24). The Hermitian part of K_a (for the ground state) also corresponds exactly to the Hamiltonian which appears in section 3.1, equation (27), which corresponds to the Hamiltonian of equation (29) in the experimentally relevant limit of $\Gamma \ll \delta$ ($\nu \approx 1$).

The point process increments $\mathrm{d}N_1(t)$ and $\mathrm{d}N_2(t)$ are, in any infinitesimal time increment $\mathrm{d}\tau$, equal to either zero or one. The probabilities for the latter are equal to the expectation values of these stochastic processes and are, respectively,

$$E[\mathrm{d}N_1] = \eta \frac{\langle\psi|(1 - 2\varepsilon \sin\tau)\sin^2(q/2)|\psi\rangle}{\langle\psi|\psi\rangle}\,\mathrm{d}\tau \tag{48}$$

$$E[\mathrm{d}N_2] = (\Gamma/\omega)\,\mathrm{d}\tau \tag{49}$$

with

$$\eta = \frac{\Gamma\Omega^2}{4\omega\delta^2|\nu|^2} = \frac{\lambda}{\omega|\nu|^2} = 2 \times \mathrm{Im}\,\frac{2\kappa}{\hbar\nu^*}. \tag{50}$$

The jumps (when $\mathrm{d}N_1 = 1$ or $\mathrm{d}N_2 = 1$) cause a discontinuous change in $|\psi\rangle$ given by equation (45), and are accompanied by a change in the internal state of the atom as follows:

$$\begin{aligned} a &\overset{\mathrm{d}N_1=1}{\rightarrow} b \quad \text{absorption,} \\ b &\overset{\mathrm{d}N_1=1}{\rightarrow} a \quad \text{stimulated emission,} \\ b &\overset{\mathrm{d}N_2=1}{\rightarrow} a \quad \text{spontaneous emission.} \end{aligned} \tag{51}$$

In the absence of these jump processes the modulus of the wavefunction decays smoothly as a result of the non-Hermitian part of the effective Hamiltonian K. From equation (50) it is clear that the rate of these jumps is related to the non-Hermitian part of the effective Hamiltonian K. When the modulus squared drops below a preset random number, a jump is assumed to occur and $\mathrm{d}N_1(\tau) = 1$. This is explained in detail in [65]. These jumps correspond to the third term in the curly brackets in equations (23) and (24).

The second jump process (spontaneous emission) can occur only when the atom is in the excited state b. For as long as the atom is in the excited state, the time until a spontaneous emission has an exponential waiting time distribution with mean ω/Γ. This is explained in detail in [59]. These jumps correspond to the first term in equations (23) and (24), proportional simply to Γ.

When a spontaneous emission occurs, the atom receives a random momentum kick represented by $\bar{p}$ in equation (45). It is given by [59]

$$\bar{p} = \hbar k \sin\phi \sin\theta, \tag{52}$$

where ϕ and θ are the Euler angles for the direction of spontaneous emission relative to the atomic dipole moment (which is orthogonal to the direction of motion x). They are generated as follows: $\phi \in [0, 2\pi)$ is a random angle with uniform distribution and θ is given by

$$\theta = \arccos\left[2\cos\left(\frac{\arccos(2y-1) + 4\pi}{3}\right)\right], \tag{53}$$

where $y \in [0, 1]$ is a random number with uniform distribution.

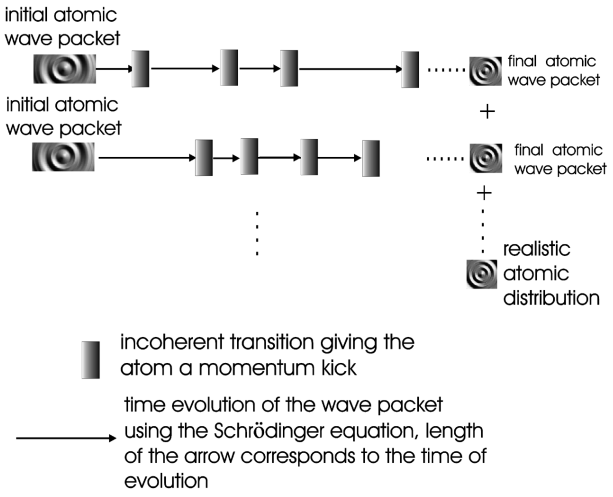

Figure 9. Graphical representation of the quantum trajectory method. The error scales with the number of trajectories n as $1/\sqrt{n}$.

For the initial states squeezed minimum uncertainty wavepackets were used with a momentum width which corresponds to the experimental spread in momentum of the initial cloud. The wavepackets are initially equally spaced inside one well of the standing wave. The smooth evolution part of the stochastic Schrödinger equation is solved numerically using the split-operator method [67]. In this method the nonunitary Schrödinger equation:

$$\mathrm{i}\hbar\frac{\mathrm{d}}{\mathrm{d}\tau}|\psi\rangle = K|\psi\rangle \tag{54}$$

has a solution (for $\delta\tau$ short enough to neglect the time dependence of K) equal to

$$|\psi(\tau + \delta\tau)\rangle = \exp\left(-\frac{\mathrm{i}(T+V)\delta\tau}{\hbar}\right)|\psi(\tau)\rangle, \tag{55}$$

where $T = p^2/2$ depends only on p and $V = K - T$ depends only on q. Using the approximation

$$\begin{aligned} \exp\left(-\frac{\mathrm{i}(T+V)\delta\tau}{\hbar}\right) &\approx \exp(-\mathrm{i}T\delta\tau/2\hbar) \\ &\times \exp(-\mathrm{i}V\delta\tau/\hbar)\exp(-\mathrm{i}T\delta\tau/2\hbar), \end{aligned} \tag{56}$$

which is correct to order $(\mathrm{d}\tau)^2$, the evolution can be simulated very fast by using fast Fourier transforms to transform between the momentum p and position q bases. An adaptive time stepsize method [68] is used to control the stepsize of the method. Once every ς steps the relative error, φ, is calculated as

$$\varphi = \frac{\| \, |\psi_\alpha\rangle - |\psi_\beta\rangle \, \|}{\| \, |\psi\rangle \, \|}, \tag{57}$$

where $\| \, |\psi\rangle \, \|$ is the modulus of $|\psi\rangle$ and

$$\begin{aligned} |\psi_\alpha\rangle &= \exp(-\mathrm{i}T\delta\tau/2\hbar)\exp(-\mathrm{i}V\delta\tau/\hbar)\exp(-\mathrm{i}T\delta\tau/2\hbar)|\psi\rangle, \\ |\psi_\beta\rangle &= \exp(-\mathrm{i}V\delta\tau/2\hbar)\exp(-\mathrm{i}T\delta\tau/\hbar)\exp(-\mathrm{i}V\delta\tau/2\hbar)|\psi\rangle. \end{aligned} \tag{58}$$

If the error lies above a specified tolerance the simulation is restarted ς steps before and the step size is decreased. A value of $\varsigma = 30$ was found to work well. This method is used to prevent unphysical behaviour due to a too large relative error.

Figure 9 shows a graphic representation of the method of quantum trajectories which is used to simulate the experiments.

3.2.3. Classical simulations. In the classical regime one can use Hamilton's equations (equations (7) and (8)) to calculate the dynamics of the system. The Hamiltonian evolution of a system preserves the Poisson bracket relation between the position variable q and the momentum variable p [69]:

$$\{q(t),\, p(t)\}_{q,p} = 1. \tag{59}$$

To prevent unphysical behaviour when using a numerical integration routine a symplectic integrator method is used which intrinsically preserves the Poisson bracket relation [70]. It was slightly changed to include time-dependent systems [71]. The Hamiltonian (which depends on the internal state of the atom) is given by

$$H_\sigma = \begin{cases} p^2/2 + 2\kappa(1 - 2\varepsilon \sin\tau)\sin^2(q/2) & \text{for } \sigma = a \\ p^2/2 - 2\kappa(1 - 2\varepsilon \sin\tau)\sin^2(q/2) & \text{for } \sigma = b. \end{cases} \tag{60}$$

This is identical to the non-Hermitian Hamiltonian K from equation (46) with ν set to unity.

To gain a realistic model incoherent transitions have been included in the classical simulation. This can be done analogously to the quantum trajectory simulations described above using a Monte Carlo simulation. The atom swaps internal states a and b when a jump occurs, as described in equations (51). The probabilities for the point process increments $\mathrm{d}N_1$ and $\mathrm{d}N_2$ are now given by

$$E[\mathrm{d}N_1] = \eta(1 - 2\varepsilon\cos\tau)\sin^2(q/2)\,\mathrm{d}\tau, \tag{61}$$

$$E[\mathrm{d}N_2] = (\Gamma/\omega)\,\mathrm{d}\tau. \tag{62}$$

When a transition takes place the position of the atom remains unchanged and the momentum is changed. When an absorption or stimulated emission takes place ($\mathrm{d}N_1 = 1$) the momentum of the atom changes by ± 1 recoil. In the case of a spontaneous emission the atom receives a random momentum kick $\bar{p}$, calculated in exactly the same way as the quantum case.

3.2.4. Other theoretical considerations. The methods presented above lead to an atomic momentum distribution resulting from the interaction of atoms with a modulated optical standing wave which is turned off and on instantaneously. To obtain more accurate results the interaction caused by a finite turn-on and turn-off time of the standing wave is added into the numerical simulations. This finite turn-on/turn-off time is due to using an acousto-optic modulator in the experiments. The shape and length of the turn-on and turn-off were measured using a 280 MHz bandwidth photodetector. It was found that it is important to match the beginning and end phase of the standing wave in the theoretical simulations closely with the experimental conditions. This was also accomplished using the photodetector mentioned above. An example of a measured modulation signal is shown in figure 10 illustrating the finite turn-on time due to the acousto-optic modulator.

The experimentally measured data consist of atomic position distributions after 10 ms ballistic expansion time, as described in section 2.1. To obtain a theoretical position distribution after 10 ms, the theoretical position distribution is evolved after the standing wave interaction for 10 ms using

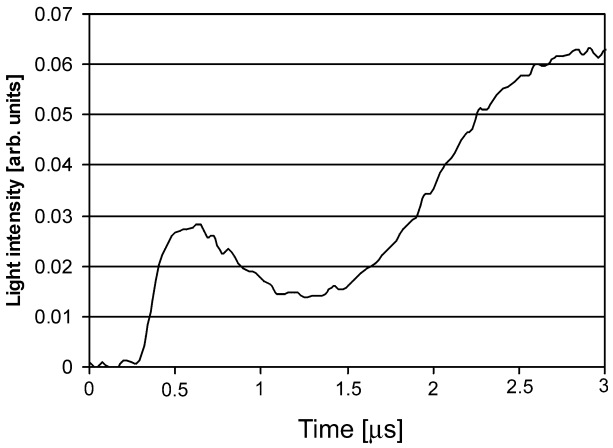

Figure 10. Example of a measured modulation signal using a 280 MHz bandwidth photodetector. The start of the modulated signal is shown illustrating the finite turn-on time of the acousto-optic modulator. The noise which can be seen is not part of the real modulation signal but is due to the low light intensity that enters the photodetector. The light intensity should rise instantaneously to $4\kappa\varepsilon$ and then follow the functional form of $2\kappa(1 - 2\varepsilon\sin(\omega t))$.

a propagator method. The position distribution $\psi(q,t)$ after free evolution of length t is given by

$$\begin{aligned}
\psi(q,t) &= \langle q|\psi(p,t)\rangle = \langle q|\exp\left[\frac{-\mathrm{i}p^2 t}{2\hbar}\right]|\psi(p,0)\rangle \\
&= \int \langle q|p\rangle\langle p|\exp\left[\frac{-\mathrm{i}p^2 t}{2\hbar}\right]|\psi(p,0)\rangle\,\mathrm{d}p \\
&= \frac{1}{\sqrt{2\pi\hbar}}\int \mathrm{d}p\,\exp\left[\frac{-\mathrm{i}p^2 t}{2\hbar}\right]\exp\left[\frac{-\mathrm{i}pq}{\hbar}\right]\psi(p,0) \\
&= \frac{1}{2\pi\hbar}\int \mathrm{d}p \int \mathrm{d}q_0 \exp\left[\frac{-\mathrm{i}p^2 t}{2\hbar}\right]\exp\left[\frac{-\mathrm{i}pq}{\hbar}\right] \\
&\quad \times \exp\left[\frac{\mathrm{i}pq_0}{\hbar}\right]\psi(q_0,0) \\
&= \int \mathrm{d}q_0 G(q,q_0,t)\psi(q_0,0)
\end{aligned} \tag{63}$$

where $G(q,q_0,t)$ is the free evolution propagator which is given by

$$\begin{aligned}
G(q,q_0,t) &= \frac{1}{2\pi\hbar}\int \mathrm{d}p \exp\left[\frac{-\mathrm{i}p^2 t}{2\hbar} + \frac{\mathrm{i}p(q_0 - q)}{\hbar}\right] \\
&= (-2\mathrm{i}t\pi\hbar)^{-1/2}\exp\left[\frac{-(q - q_0)^2}{2\mathrm{i}t\hbar}\right]
\end{aligned} \tag{64}$$

using

$$\int \mathrm{d}x \exp(-ax^2 + bx) = \left(\frac{\pi}{a}\right)^{1/2}\exp\left[\frac{b^2}{4a}\right]. \tag{65}$$

The position distribution after 10 ms turns out to be very similar to the momentum distribution straight after the standing wave interaction as the free evolution effectively transfers all the momentum features into the position distribution. Because of this the experimental results are sometimes referred to as momentum distributions, although they are, strictly speaking, position distributions.

Finally one needs to consider the finite position width of the initial cloud, which will contribute to the final

position distribution. Therefore the final theoretical position probability distribution $|\psi(q,t)|^2$ is convoluted with the initial Gaussian position probability distribution $P_0(q)$ (before the standing wave interaction) to obtain the final theoretical prediction $P(q,t)$:

$$P(q,t) = \int \mathrm{d}q_0 \, |\psi(q-q_0,t)|^2 P_0(q_0). \qquad (66)$$

This is valid only if the initial density operator is an incoherent mixture of wavepackets, which is true for a thermal atomic cloud.

4. Phase space characterization of the driven pendulum in atom optics

4.1. Dependence on the modulation parameter ε and the scaled well depth κ

Using the techniques described in section 2, experimental analysis of size, position and momentum of the regions of regular motion surrounding the phase space resonances and other phase space features was carried out and the experimental results are compared with the applicable theory. This discussion concentrates on experiments with $\bar{k} = 0.1$ (modulation frequency $\omega/2\pi = 300$ kHz) and an interaction time of 7.25 modulation periods, when the modulation parameter ε is varied and the scaled well depth κ is held constant ($\kappa = 1.15$). Figure 11 shows experimental results (black curve) as well as quantum trajectory simulations (grey curve) for the resulting atomic momentum distributions for different values of the modulation parameter ε. Distinct peaks in the momentum distribution correspond to period-1 phase space resonances. Below the experimental data, Poincaré sections (see section 2.3) illustrate the classical phase space. To obtain these Poincaré sections the modulation phase for the classical stroboscopic evolution is chosen such that the period-1 regions of regular motion are located on the momentum axis (modulation phase is maximum modulation amplitude). Two regions of regular motion can be seen which result from period-1 resonances that bifurcate from the origin at $\kappa \approx 1$ (meaning that the resonances start to emerge at that value of κ: a detailed description of the bifurcation sequence will be given in section 5). The islands are encircled by a sea of chaos. It can be seen that the size and the shape of the centre resonance and the two period-1 resonances are strongly dependent on the modulation parameter ε. Figure 11(a) shows the unmodulated case. The central region of bound motion is bound by the classical separatrix. All atoms exhibit regular motion classically. In figure 11(b) two period-1 resonances have emerged for modulation parameter $\varepsilon = 0.22$. Chaotic motion can be seen in the Poincaré section. With increasing values of ε the regions of regular motion surrounding period-1 resonances become more pronounced, as can be seen in the experimental data and the quantum simulations. The region of regular motion centred at zero momentum becomes smaller and eventually disappears in the sea of chaos, as can be seen in figures 11(d)–(f). The small regions of regular motion positioned close to the region of unbound motion (librations) are never (for no phase of the standing wave modulation) located on the position axis. This means that they cannot be

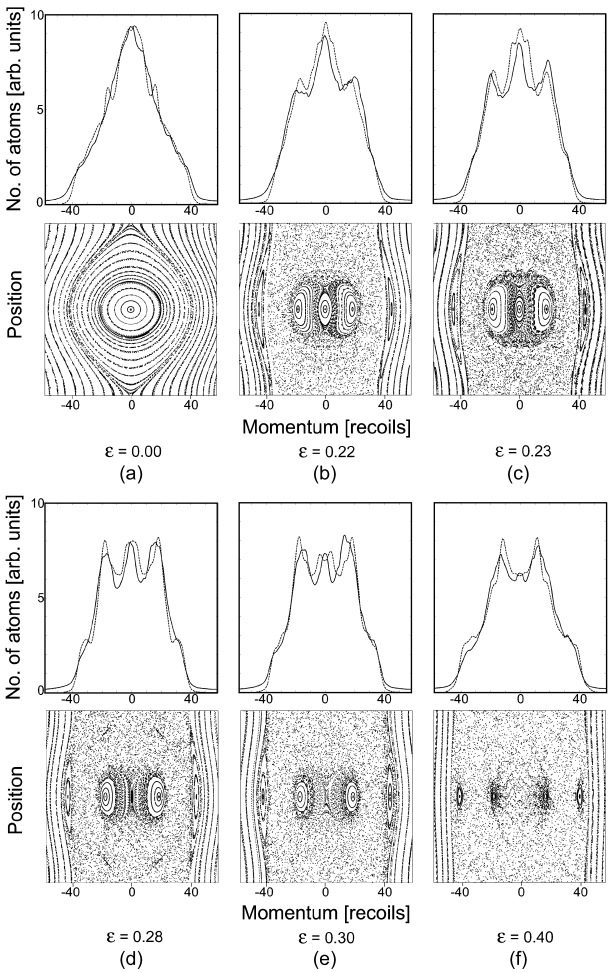

Figure 11. The upper section shows the experimental atomic momentum distributions (black curve) together with a quantum simulation (grey curve) using the trajectory method of section 3.2.2 for different values of the modulation amplitude ε. The lower part contains the corresponding Poincaré sections. The size of the resonances is strongly dependent on the modulation amplitude ε.

observed in the experiment as they need to cross the position axis to be loaded, as explained in section 2.5 (see figure 6(b)). Due to the small initial momentum width, atoms are not loaded into the region of regular unbound motion. Chaos leads to a homogeneous spread which is confined by the region of regular unbound motion. The small shoulders visible in both experimental data and quantum simulations presumably result from this chaotic redistribution. One can see that there is good agreement with both the quantum trajectory simulations and the classical prediction.

Furthermore the phase space was examined for different values of the scaled driving amplitude κ. Figure 12 shows experimental results (black curve) for a range of κ between 1.11 and 1.36 with the scaled Planck's constant $\bar{k}$ kept constant at 0.1 (modulation frequency $\omega/2\pi = 300$ kHz), the modulation amplitude ε kept constant at 0.32 and an interaction time of 7.25 modulation periods. These data were obtained by adjusting the detuning δ of the modulated standing wave. Alternatively an adjustment of the modulation frequency (with constant detuning) or a change of the intensity of the standing wave can be used to vary the scaled well depth κ which would give

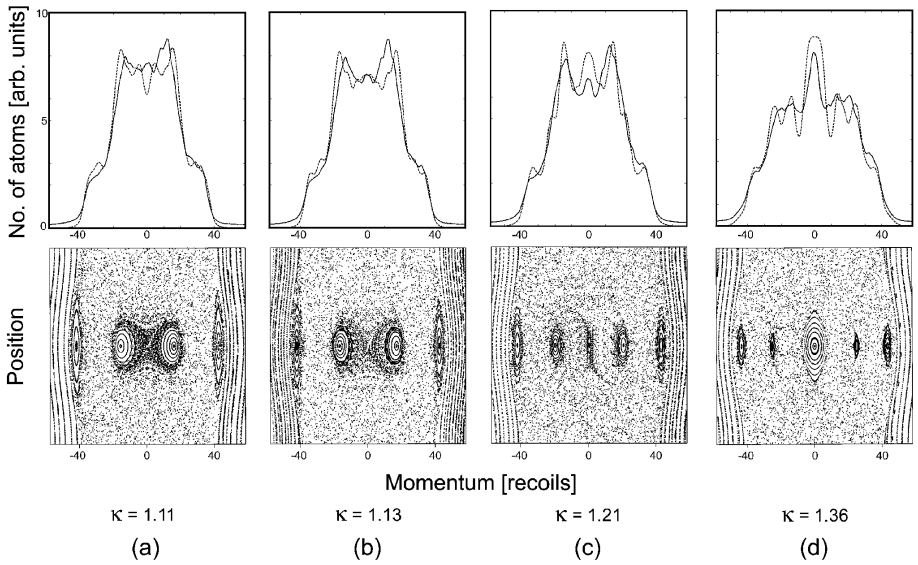

Figure 12. Experimental data (black curve) and quantum trajectory simulation (grey curve) showing resonances and other phase space features as a function of the scaled driving amplitude κ. The velocity of the resonances changes with κ. The corresponding Poincaré sections are shown below.

similar results to that of figure 12. However, a change of the modulation frequency will also change the scaled Planck's constant $\bar{k}$ of the system. Theoretical predictions from the quantum mechanical calculations are also shown (grey curve). The lower section of figure 12 contains the corresponding Poincaré sections. One can see that, with changing values of κ, the velocity of the resonances is changed as is the size of the regions of regular motion. With increasing κ the resonances become faster. A small κ step size between figure 12(a) and (b) was chosen to illustrate this increase in velocity without introducing a significant qualitative change of phase space. Figure 12(c) features the emergence of a centre island. With κ increasing even further the period-1 resonances move out, become smaller as shown in figure 12(d) and will eventually disappear in the sea of chaos.

Slight discrepancies between quantum trajectory simulations and the experimental data could result from non-uniformities in the initial experimental position and momentum distribution and the uncertainty in the determination of the scaled well depth κ and the modulation parameter ε. Furthermore, small errors in the alignment of the optical standing wave relative to the atomic cloud can possibly lead to discrepancies between theory and experiment. In spite of such potential problems the agreement between the experiment and both quantum and classical theories is very good.

Nonlinear dynamics theory predicts that, for every value of κ, there will be a resonance if the ratio of modulation frequency and nonlinear natural frequency is rational. When this occurs the system exhibits a resonance. However, the size of the islands of regular motion resulting from these resonances is very sensitive to system parameters ε and κ. In some cases islands of regular motion are infinitely small, while in others they form stable islands. The quantum simulations predict the formation of observable regions of regular motion for driving amplitudes in the range $\kappa = 1.0$–1.5. In the experiment a maximum size of the regions of regular motion was found for the scaled driving amplitude κ in a range between 1.1 and 1.3 for modulation parameter $\varepsilon = 0.32$, as predicted by theory. It should be noted that the variation of the scaled well depth κ and ε can sometimes result in the occurrence of bifurcations, an example of which is the emergence of the central island in figure 12(c). A full bifurcation sequence was mapped and will be discussed in section 5.

4.2. Resonance momentum

While period-1 resonances were discussed in the preceding section, here the dynamics of period-2 resonances are discussed that occur at lower values of scaled well depth κ. Utilizing period-2 resonances one can obtain a wider range of the momentum of the regions of regular motion because period-2 resonances occur for a smaller value of κ, allowing a larger detuning at a given modulation frequency[2]. Effectively this means higher modulation frequencies are accessible in the experiments, resulting in higher momenta of the resonances as will be explained below. Momentum measurements of the resonances were made for a range of modulation frequencies while keeping scaled well depth κ and modulation parameter ε constant. As long as κ and ε are kept constant, the resonances will appear at the same scaled momentum. The measured momentum p_x of the resonances is proportional to the scaled momentum p multiplied by the modulation frequency ω. Therefore the momentum of the resonances should scale linearly with modulation frequency.

For different values of the modulation frequency ω, the detuning δ was adjusted to obtain the same value of the modulation parameter κ. Then the momentum of the peaks in the atomic momentum distribution resulting from the period-2 regions of regular motion was measured using ballistic expansion. A graph of the experimental results is shown in figure 13. The resonance momenta and their errors shown are obtained

[2] If the detuning becomes too small the adiabatic elimination of the excited state breaks down and the centre-of-mass dynamics become far more complicated.

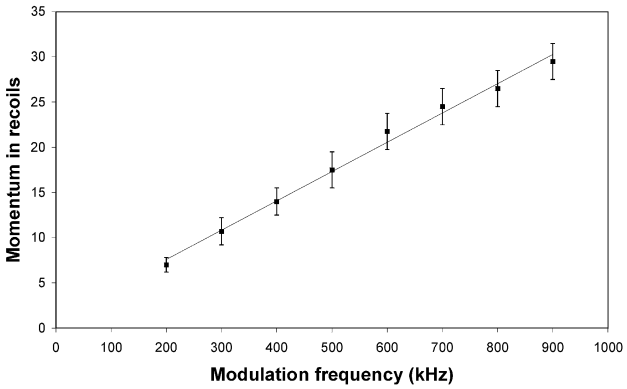

Figure 13. Momentum of the resonances for different values of the modulation frequency $\omega/2\pi$. The modulation parameter ε and the scaled well depth κ are held constant. Results for modulation parameter $\varepsilon = 0.32$, scaled well depth $\kappa \approx 0.3$ and an interaction time of 6.5 modulation periods are shown. A linear fit is well within the error bars. This mechanism could be used for effective momentum preparation of an ensemble of atoms.

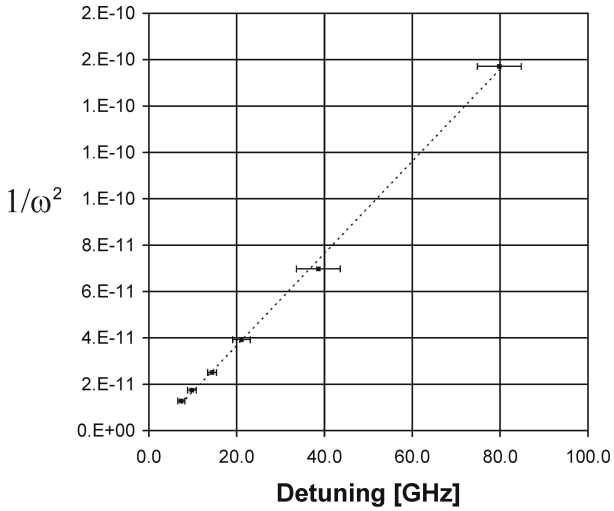

Figure 14. Parameters for the observation of phase space resonances when the modulation parameter ε and the scaled well depth κ are kept constant. The plot confirms that κ is a good qualitative indicator for the atomic momentum distributions.

from a least-squares analysis of time-of-flight data. The error bars also include the momentum error resulting from the finite width of the peaks in the momentum distribution as well as slight asymmetries in their shape. There is a linear relation between the modulation frequency and the momentum of the resonances as predicted by theory.

In fact these results can be interpreted as the experimental proof for the mapping of several different physical experiments into one unique theoretical case using scaled variables. The scaled quantum and classical theories produce a unique result for ε and κ kept constant, while the resonance momentum can be varied experimentally from 0 to many recoils by adjusting the modulation frequency ω and compensating with the detuning δ.

For future studies it would be of interest to carry out a more comprehensive range of momentum measurements and compare that to the appropriate classical and quantum theory. Some introductory results will be shown in section 5.3.

4.3. Location of the resonances in the experimental parameter space

The meaning of the scaled well depth becomes clear when conducting an experiment where the modulation frequency is varied and the appropriate detuning δ is found, so that the shape of the atomic momentum distribution remains unchanged (note, however, that the momentum of the resonances changes as explained above). The scaled well depth κ is inversely proportional to the detuning δ and the square of the modulation frequency ω ($\kappa \sim (\omega^2\delta)^{-1}$). Therefore if there is a linear relationship between $1/\omega^2$ and the detuning δ it is some indication that κ determines the qualitative behaviour (or shape) of the momentum distribution. In figure 14 the inverse squared modulation frequency $1/\omega^2$ is plotted as a function of the detuning δ for the same experiment, as described in figure 13. The error bars result from the visual uncertainty in determining that the shape of the atomic momentum distribution remains unchanged. Note that, although the scaled well depth κ is held constant in this experiment, the scaled Planck's constant $\bar{k}$ is varied. This measurement is only meant as a rough guide as it includes the subjective judgment of the author in determining whether there is a significant change in the shape of the momentum distribution.

4.4. The effects of small-amplitude noise

Exploring the effects of noise on an atom–optical system is of importance as the mechanisms involved are closely related to decoherence. This is an intense area of study due to its importance in the development of new quantum technologies. Goetsch and Graham [72] have undertaken a theoretical study where they analysed the influence of spontaneous emission on the dynamical localization in atomic momentum transfer experiments. Experiments on the effects of noise and dissipation on dynamical localization were carried out by Klappauf *et al* [39], Steck *et al* [73] and by Christensen's group [38, 63]. A short introduction is presented here on how intensity noise affects the atomic momentum distribution of the driven pendulum. To implement this, noise was added to the modulated standing wave by adding a random number between -1 and 1 multiplied by both the full modulation amplitude κ and the noise factor between 0 and 1 to every point of the modulation signal. The random number sequence was generated using the random number generator of the LabView programming environment. This corresponds approximately to adding white noise to the modulation signal limited by the bandwidth of the acousto-optic modulator.

Figure 15 shows an example of experimental results with small noise amplitudes. Figure 15(a) shows the atomic distribution with no added noise. In figure 15(b), 10% amplitude noise (noise factor: 0.1) was added to the standing wave. Although the ratio between the height of the centre resonance and the period-1 resonances changes slightly, the difference between the two cases is nearly negligible. It is remarkable that the peaks in the atomic momentum distribution corresponding to resonances are fairly stable even with quite significant amounts of noise. It was tested that this behaviour is reproducible with different random

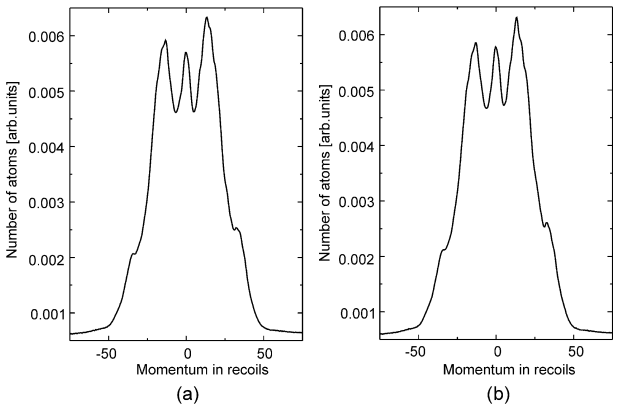

Figure 15. Amplitude noise is introduced to the system. The atomic momentum distribution is remarkably stable. While there was no noise added in part (a), 10% amplitude noise was added to obtain part (b). The data were obtained using an interaction time of 7.25 modulation periods, modulation parameter $\varepsilon = 0.26$, modulation frequency $\omega/2\pi = 300$ kHz and scaled well depth $\kappa \approx 1.20$.

number sequences. A similar behaviour was also observed in experiments with different scaled well depth κ, modulation parameter ε and modulation frequency ω. It can be concluded that small amounts of noise in the modulation amplitude do not significantly change the dynamics of the driven pendulum in atom optics. The effects of large noise amplitudes have not been thoroughly explored yet and could be the subject of further study. Initial experiments have shown interesting features. Different types of noise, for example phase noise and spontaneous emission leading to random kicks, could be investigated.

5. Phase space bifurcations

5.1. Introduction

In this section it will be shown that most of the qualitative aspects of the dynamics of the system can be described using classical perturbation theory if the scaled Planck's constant and the experimental times scales are sufficiently small (in this section $\bar{k} = 0.1, t \sim 7$ modulation periods). An exception may occur for the resonance momentum as explained in section 5.3. However, if the scaled Planck's constant is sufficiently large quantum effects are significant, even on small timescales. This will be shown in section 9. Classical physics predicts the occurrence of a bifurcation sequence in the dynamics of the driven pendulum. This section illustrates that this bifurcation sequence can be found in the dynamics of ultra-cold atoms in a modulated optical lattice. To illustrate this bifurcation sequence the scaled well depth κ is used as the control parameter. For further discussion of bifurcation theory, see for example [43, 74]. Bifurcations have been observed in other Hamiltonian systems such as the absorption spectra of atoms in electric and magnetic fields. Experimental measurements showed that stable periodic electron orbits bifurcated to new orbits of longer period [75, 76].

The scaled well depth κ (for definition see section 2.2) and the momentum coordinate p are scaled with modulation frequency ω. For the experiments which are presented here the modulation frequency was kept constant ($\omega/2\pi = 300$ kHz), so that experiments with different values of κ can be compared using real momentum coordinates. To change the value of κ the detuning δ of the modulated standing wave is adjusted while the intensity I is held constant. The intensity measurement error is +8/–5% and it is a systematic error which is the same for all data presented in this section. The error in the detuning of the standing wave is smaller than 3% and it is a random error given by the accuracy of the wavemeter which was used.

5.2. The bifurcation sequence

Figure 16 shows the bifurcation sequence in terms of Poincaré sections along with corresponding experimental momentum distributions. All the observed resonances bifurcate from the origin, where the oscillation frequency is $\sqrt{\kappa}$. Since a period-$(\frac{n}{m})$ resonance occurs when the period of the oscillation is $\frac{n}{m}$ times the period of the driving, a period-$(\frac{n}{m})$ resonance bifurcates when $\kappa = \frac{m^2}{n^2} + \mathrm{O}(\varepsilon)$, where n and m are integers and ε is the modulation parameter. Detailed analysis shows that the particular perturbation term implies that only resonances with $n \geqslant 2$, and even $m \geqslant 1$, occur. Those with $n = 2$ can be easily seen in Poincaré sections in figure 16, appearing as two symmetrically placed resonance islands. They are also of particular interest experimentally as they can be easily identified in the experimental momentum distribution as two peaks on either side of the centre.

To obtain the dependence of the bifurcation on the modulation parameter ε classical perturbation theory about the origin is used. The state variables (p, q) are assumed to be of order $\sqrt{\varepsilon}$. For κ close to resonance ($\kappa \approx \frac{m^2}{n^2}$), one can use canonical perturbation theory [1, 43] to give a fairly accurate picture of the emerging resonances. The scaled well depth κ is expanded as a series in ε about the resonance:

$$\kappa = \kappa_0 + \varepsilon\kappa_1 + \varepsilon^2\kappa_2 + \cdots, \tag{67}$$

where κ_0 is the value at resonance with $\kappa_0 = \frac{1}{4}$, 1 and $\frac{9}{4}$ for the resonances that are observed experimentally. Near the origin q is small and of the order of $\sqrt{\varepsilon}$, so that $(\sin(\frac{q}{2}))^2$ may be approximated by the first few terms in its Taylor series about zero.

Then to zeroth order in ε

$$H = H_0 = \frac{p^2}{2} + \kappa_0\frac{q^2}{2}, \tag{68}$$

which has action-angle variables (I, θ) where

$$p = \kappa_0^{\frac{1}{4}}\sqrt{2I}\cos(\theta), \qquad q = \frac{\sqrt{2I}}{\kappa_0^{\frac{1}{4}}}\sin(\theta). \tag{69}$$

Hence the Hamiltonian becomes

$$H(I, \theta, \tau) = \sqrt{\kappa_0}I + H_1(I, \theta, \tau) + H_2(I, \theta, \tau) + \cdots; \tag{70}$$

where H_m is $(m+1)$th order in ε. H_m has resonant oscillatory terms $\cos(m\tau - n\theta)$, where n is even, implying mth-order resonances at the origin when $n\sqrt{\kappa_0} = m$.

To investigate the resonance at $\kappa_0 = \frac{1}{4}$ two canonical transformations are used. The first is a near-identity transformation $I' = I + \mathrm{O}(\varepsilon)$, $\theta' = \theta + \mathrm{O}(\varepsilon)$ [1, 43] that

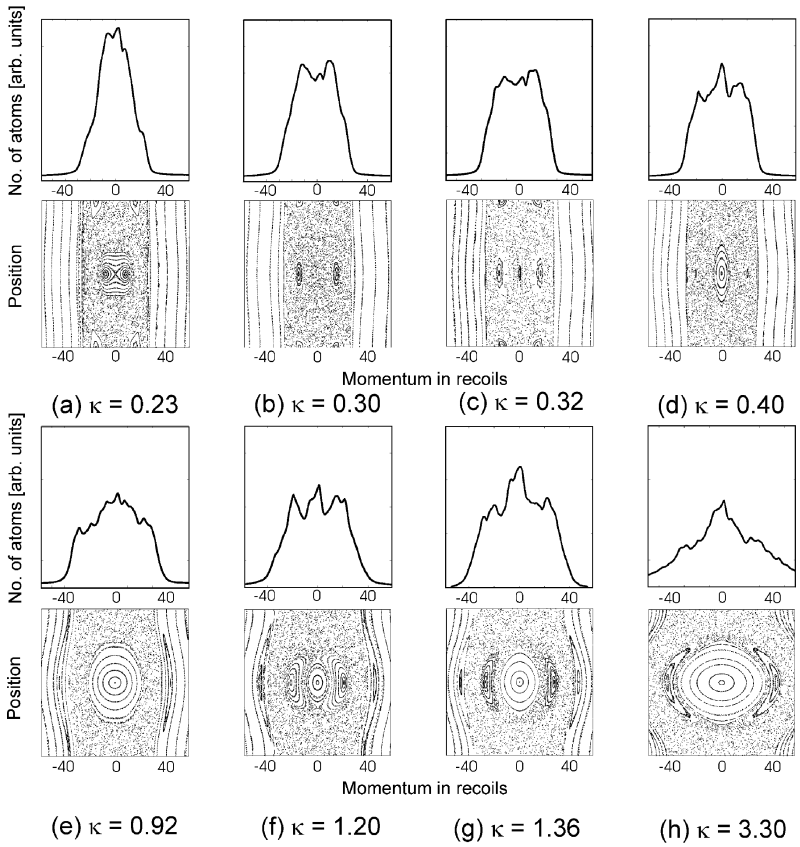

Figure 16. Bifurcation sequence. The upper pictures are the experimentally measured momentum distributions for modulation parameter $\varepsilon = 0.20$ and modulation frequency $\omega/2\pi = 300$ kHz. The corresponding classical Poincaré sections are shown below where the x axis is the momentum coordinate and the y axis is the position coordinate along the standing wave. The resonances appear as distinct peaks in the momentum distribution. When the scaled well depth κ is increased several bifurcations occur in this mixed phase space.

removes all the oscillating terms, except those that are resonant. The transformed Hamiltonian is then

$$H = \sqrt{\kappa_0} I' - \frac{I'^2}{16} + \varepsilon \frac{\sqrt{\kappa_0}}{2} I' \cos(\tau - 2\theta') - \varepsilon \frac{\kappa_1}{2\sqrt{\kappa_0}} I' + \cdots . \tag{71}$$

The second transformation consists of moving to a rotating frame $I' = J$, $\phi = \theta' - \frac{\tau}{2}$. In this rotating frame the Hamiltonian is

$$K = \varepsilon \kappa_1 J - \frac{1}{16} J^2 + \frac{\varepsilon}{4} J \cos(2\phi) + \cdots . \tag{72}$$

Using $\bar{p} = \sqrt{J}\sin(\phi)$ and $\bar{q} = 2\sqrt{J}\cos(\phi)$, the system of equations for $\bar{p}$ and $\bar{q}$ has stable fixed points on the (transformed) momentum axis that correspond to period-2 resonances of the original system. Since at a fixed point ϕ is a constant, so that $\theta = \tau/2 + \text{constant}$, the period of θ is twice the forcing period ($\phi = \tau - 2\theta$ implies a period-2 resonance). Thus they rotate with half the modulation frequency. By including higher-order terms in the Hamiltonian one can show that these fixed points only exist for $\kappa > \frac{1}{4}(1 - \varepsilon + \varepsilon^2 - \varepsilon^3)$ and that they destabilize the origin. They are just apparent in the Poincaré map in figure 16(a). As κ is increased the islands move apart and become separated by a sea of chaos as shown in figure 16(b). Then for $\kappa > \frac{1}{4}(1 + \varepsilon + \varepsilon^2 + \varepsilon^3)$ two unstable fixed points bifurcate into the (transformed) position axis, stabilizing the origin once again. Figure 17 shows a bifurcation diagram where the values of the scaled depth κ for which a bifurcation occurs are plotted as a function of the modulation parameter ε. Between the two curves mentioned above, which are shown in figure 17, the momentum distribution is clearly depressed in the centre, as shown in figure 16(b), whereas for $\kappa > \frac{1}{4}(1 + \varepsilon + \varepsilon^2 + \varepsilon^3)$, at (c) the three distinct islands of regular motion appear clearly as three peaks in the momentum distribution. As κ increases further, the period-2 islands move out, breaking up as they do so, and eventually become indistinguishable from the chaotic sea (figures 16(d) and (e)). In figure 16 many of the Poincaré sections also show librational resonances. As they do not rotate they will not cross the position axis and therefore they are not loaded by the initial atomic momentum distribution in the current experimental set-up. Thus they do not appear in the experimentally measured momentum distribution.

The resonance at $\kappa_0 = 1$ is of second order, meaning that it is only apparent once the first-order oscillatory terms have been removed. These are removed via a near-identity transformation similar to the one described earlier except now $\kappa_0 \neq 1/4$ so that the transformation can be chosen to remove all the first-order oscillatory terms. This introduces further resonant terms of the form $\cos(2\tau - 2\theta)$, giving rise to period-1 resonances as shown in figure 16 parts (f) and (g). Once again to investigate them further two canonical transformations must be made. The second, as before, transforms to a rotating frame, but here $\phi = \theta' - \tau$. What

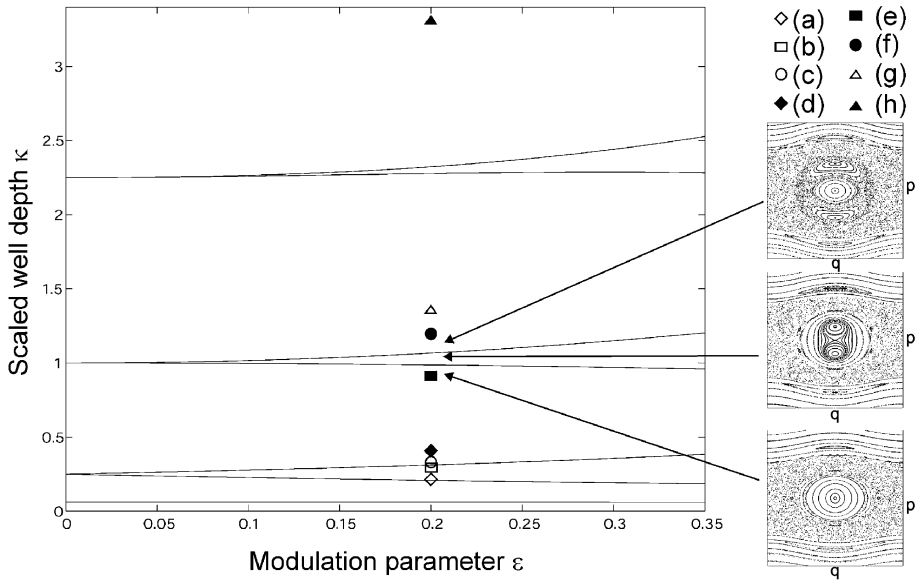

Figure 17. The bifurcation diagram for the driven pendulum in atom optics. When the scaled well depth κ is changed the system undergoes multiple bifurcations. The values of κ where bifurcations occur depend on the modulation parameter ϵ. Three Poincaré sections are plotted. The arrows indicate to which part of the bifurcation diagram they correspond. The x axis in the Poincaré sections is the position coordinate and the y axis is the momentum coordinate. Symbols illustrating the corresponding parts of figure 16 are shown.

follows is similar to the $\kappa = \frac{1}{4}$ case. Two similar bifurcations stabilizing, and then destabilizing, the origin take place for

$$\kappa = 1 + \frac{5\varepsilon^2}{3} \qquad \text{and} \qquad \kappa = 1 - \frac{5\varepsilon^2}{3}. \tag{73}$$

They are now of the order of ε^2 apart, which makes the individual bifurcations difficult to see experimentally.

The pattern is repeated again for the third-order resonance at $\kappa = \frac{9}{4}$, due to the presence of $\cos(3\tau - 2\theta)$ terms. The bifurcation curves are of the order of ε^3 apart and they are given by

$$\kappa = \frac{9}{4} + \frac{81\varepsilon^2}{64} + \frac{81\varepsilon^3}{256} \qquad \text{and} \qquad \kappa = \frac{9}{4} + \frac{81\varepsilon^2}{64} - \frac{81\varepsilon^3}{256} \tag{74}$$

($\phi = 3\tau - 2\theta$ implies a period-2/3 resonance). As one expects the momentum separation between regions of unbound regular motion becomes larger when the value of κ is increased. This is due to the wells becoming effectively deeper. Figure 17 represents the experimental regime where it was possible to map the bifurcation sequence. The bifurcation curves shown, for $\kappa \approx 1/4$, 1 and 9/4, are to order ε^3. For a deeper understanding of the bifurcation diagram three Poincaré sections for the $\kappa = 1$ bifurcation are plotted. The arrows indicate the part of the bifurcation diagram which they represent. The symbols in figure 17 indicate the corresponding parts of figure 16.

The lower experimental limit of the scaled well depth κ for this sequence is determined by the momentum width of the initial atomic cloud. The kinetic temperature of the cloud was approximately 10 μK. If the initial momentum spread of the atomic cloud is much wider than the momentum width of the resonances, resonances cannot be resolved anymore in the experimentally measured position distribution. This is because the resonance features then become submerged in the chaotic background. Immediately after the loading phase, when the atomic density inside the chaotic region is equal to the density inside the islands of regular motion (both equal to the initial atomic density), resonances do not constitute a feature in the atomic momentum distribution. However, after sufficient time, atoms in the chaotic region can spread over a larger volume (filling the entire chaotic region) that leads to a smaller atomic density in the chaotic region. This results in a significant atomic-number signal-to-noise ratio between the regular region and the chaotic region in the atomic momentum distribution. For values of κ far below 0.2 the initial atomic momentum distribution extends past the resonances, over the chaotic region and into the region of regular unbound motion. This problem could be overcome by preparing atoms with a lower kinetic temperature as that would imply a decrease in the momentum width. Alternatively one could increase the modulation frequency.

The upper limit of κ is determined by the laser intensity and the detuning of the standing wave. When the detuning of the standing wave becomes too small, incoherent transitions need to be considered and the adiabatic elimination of the excited state in the theory breaks down. The dynamics can no longer be described by the Hamiltonian given in equation (1). Furthermore spontaneous emission will act as a source of dissipation.

To perform an alternative mapping of the experimental results to the bifurcation sequence the rotation frequency of the resonances is measured. This measurement determines the period of the resonances. To conduct these measurements the length of the interaction with the modulated standing wave is varied (which is equivalent to a variation of the endphase of modulation) measured in modulation periods (cycles) and the resulting atomic momentum distribution is recorded. Figure 18 shows the rotation frequency measurements for the resonances bifurcating at scaled well depth $\kappa = 0.25$ (modulation parameter $\varepsilon = 0.20$, modulation frequency $\omega/2\pi = 300\,\text{kHz}$).

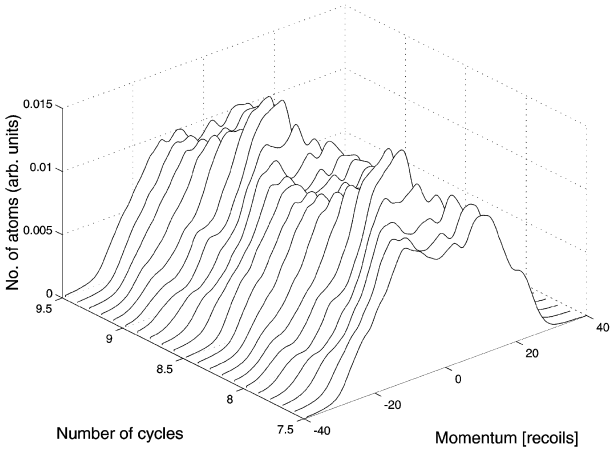

Figure 18. Verification of the value of the period for the resonances at the $\kappa = 0.25$ bifurcation. Atomic momentum distributions are shown for different interaction times with the modulated standing wave measured in cycles. One can see that atoms inside a region of regular motion return to their initial phase space positions after two periods of the standing wave modulation.

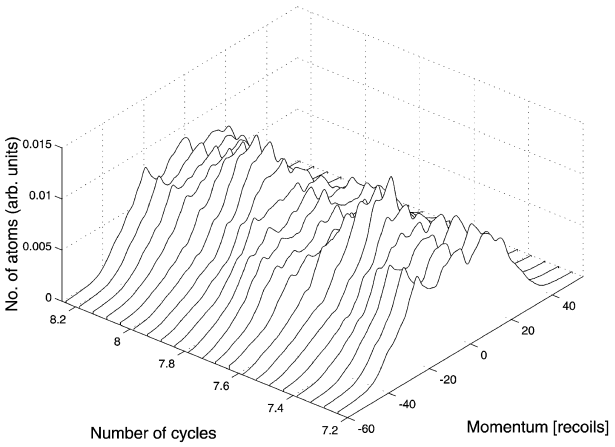

Figure 19. Verification of the value of the period for the resonances at the $\kappa = 1$ bifurcation. Atomic momentum distributions are shown for different interaction times with the modulated standing wave measured in cycles. One can see that atoms inside the region of regular motion return to their initial phase space positions after one period of the standing wave modulation. When the resonances have rotated by 180° (7.7 cycles) with respect to their initial phase space positions (7.2 cycles) the peaks in the momentum distribution have become wider compared to their initial width at 7.2 cycles.

Resonances can be observed clearly when they are located on the momentum axis when the standing wave is turned off (they are at the bottom of the well—see figure 4) and will disappear when located on the position axis at that time (they are at the top of the well—see figure 4). At 7.5 modulation periods one can see two distinct peaks in the atomic momentum distribution resulting from phase space resonances. These have completely disappeared after 8 modulation periods. The resonances can again be seen as distinct peaks in the momentum distribution after 8.5 periods of the standing wave modulation. Therefore it follows that the resonances needed one modulation period to rotate by 180° in phase space (atoms inside the resonance completed half an oscillation period). After two modulation periods the atoms inside the region of regular motion appear

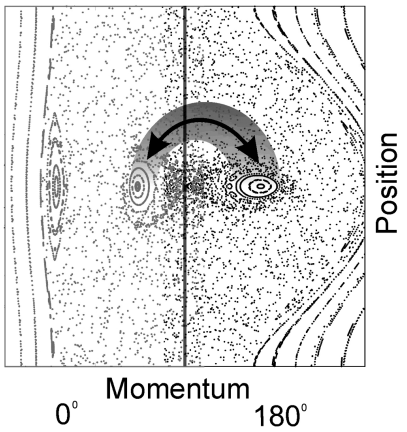

Figure 20. A Poincaré section is shown for scaled well depth $\kappa = 1.2$. While the left-hand side corresponds to 7.2 cycles, the right-hand side shows the corresponding phase space after a 180° rotation at 7.7 cycles. One can see that the momentum width of the resonances has significantly decreased.

again at their initial positions. Hence they are period-2 regions of regular motion.

Figure 19 shows the rotation frequency measurements for the resonances bifurcating at $\kappa \approx 1$ (modulation parameter $\varepsilon = 0.20$, modulation frequency $\omega/2\pi = 300$ kHz) which exhibits different features compared to figure 18. This allows one to distinguish between different bifurcation regimes. After 7.2 cycles one can see three distinct peaks in the atomic momentum distribution resulting from regions of regular motion and the centre island of stability. A quarter period later the resonances have rotated onto the position axis and therefore are no longer visible. Another quarter period later atoms inside the region of regular motion have rotated by 180° and are now located on the momentum axis. Note that the peaks in the atomic momentum distribution corresponding to the regions of regular motion have become wider and that their intensity has decreased as compared to the distribution at 7.2 periods of the standing wave modulation. To understand this phenomenon one needs to consider the corresponding Poincaré sections as illustrated in figure 20. The left-hand side shows the phase space after 7.2 cycles, while the phase space after 7.7 cycles is shown on the right-hand side. Phase space volume is preserved in Hamiltonian systems. However, the shape of the resonances has changed significantly. The momentum width of the resonance after 7.7 periods is larger compared to the one at 7.2 cycles. This results in the experimentally observed broadening of the resonances. It can also be seen that the resonance is slightly faster after 7.7 cycles than after 7.2 cycles. Intuitively this can be understood when considering that, at 7.7 cycles, the well depth has its maximum amplitude. Therefore the gradient is higher for a particle 'rolling' down the well, allowing it to acquire a larger momentum, compared to the situation at 7.2 cycles where the well depth is at minimum. From the discussion above it follows that these resonances need one modulation period to return to their initial position at $\kappa \approx 1$, making them period-1 resonances.

The rotational frequency for the period-$(2/3)$ resonances that are shown in figure 16(h) was also measured. Their period was successfully confirmed.

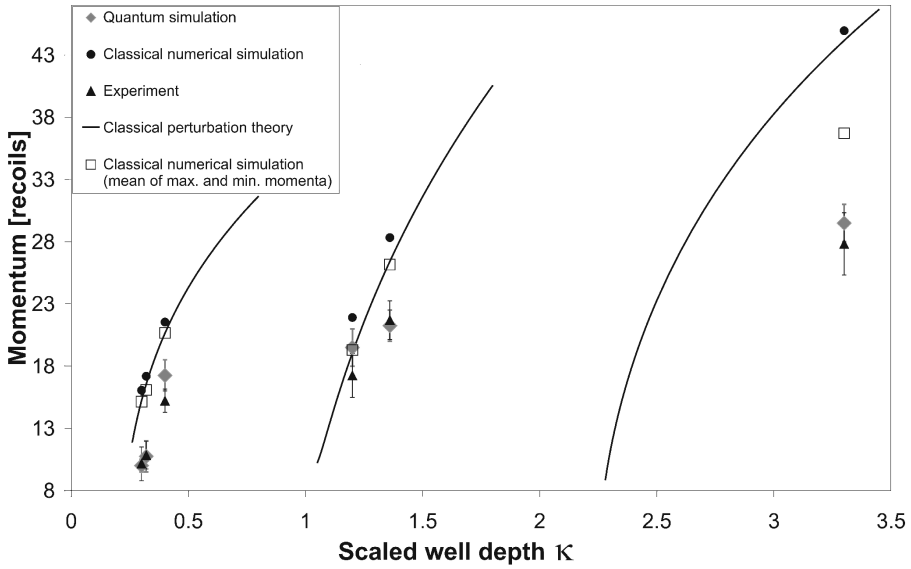

Figure 21. Momenta of resonances in different bifurcation regimes. The momentum of different resonances is plotted as a function of the scaled well depth κ. These are compared with predictions from the quantum simulation, momentum of the fixed point in the Poincaré section (classical numerical simulation) when positioned on the momentum axis and results from classical perturbation theory. Also plotted is the mean of the minimum and maximum momentum of the island of regular motion when positioned on the momentum axis obtained from the classical numerical simulation.

5.3. Experimental resonance momenta in the bifurcation sequence and quantum and classical predictions

Figure 21 compares the experimental results with predictions from quantum trajectory simulations and the classical description. The momentum of the centre of the peak in the atomic momentum distributions was measured both for the experimental data and the quantum simulations. The error bars for the experimental data result from the readout uncertainty due to asymmetries in the experimentally measured momentum distribution. These asymmetries are most likely due to non-uniformities in the initial spatial distribution of the MOT. Other possible error sources include an imperfectly zeroed magnetic field in the interaction region. The momenta of resonances in the quantum simulation exhibit some readout uncertainty because the peaks in the momentum distribution do not necessarily have a symmetric Gaussian shape. This readout uncertainty is reflected in the error bars for the quantum simulations.

These results are compared with the momentum of the resonances when they are located on the momentum axis, as calculated from numerical solutions of the equations describing the classical system and also from classical perturbation theory. To zeroth order in ε, the momentum p of the period-$(\frac{n}{m})$ resonances is found by setting the nonlinear frequency $\omega(H)$ of the unperturbed system equal to $\frac{m}{n}$ so that the momentum is given by

$$\omega(p^2/2) = \frac{m}{n}. \tag{75}$$

Here $\omega(H)$ is given by

$$\omega(H) = \frac{\pi\sqrt{\kappa}}{2F\left(\pi/2, \sqrt{\frac{H}{2\kappa}}\right)} \tag{76}$$

where $F(\pi/2, \kappa)$ is the complete elliptic integral of the first kind. Canonical perturbation theory, here performed to order ε^2 and including the first three Fourier coefficients of the perturbation, can be used to refine the result. As can be seen in figure 21 there is satisfactory agreement between the experimental results and the quantum simulations. The results taken from the Poincaré sections (numerical solution of Hamilton's equations) and the analytical classical results from perturbation theory are in good agreement. However, the classical predictions show a larger resonance momentum than the quantum simulations and the findings of the experiment. While the classical theory predicts the momentum of the fixed point (when positioned on the momentum axis), the quantum simulations directly predict the full momentum distribution as measured in the experiment. Part of the above discrepancy could result from the fact that the fixed points are positioned asymmetrically towards the faster side of the region of regular motion which, in turn, gives rise to the peak in the experimentally measured momentum distribution. However, if one assumes the mean of maximum and minimum momenta occupied by the region of regular motion (when positioned on the momentum axis) as a classical momentum approximation for the experimentally observed momentum peak, the classical resonance momenta are still significantly faster than the experimentally measured values. These results suggest a possible explanation in terms of the theory of quantum slow motion [44], but more rigorous and detailed investigation would be needed to confirm this. The theory of quantum slow motion shows that the complicated quantum dynamics of the atomic wavepacket on a classical resonance given by the quantum Liouville equation can be replaced by the wavepacket's (in fact, the corresponding classical probability distribution's) classical dynamics with a modified potential within certain limits. The theory predicts atoms starting near a classical phase space resonance to move slower than one would expect classically.

6. Atomic momentum preparation and ensemble beamsplitting

6.1. Introduction

The study of quantum nonlinear dynamics can have some important applications for atom optics experiments. Sometimes it can be important for experiments to have the capability to prepare an ensemble of atoms with adjustable mean momentum and momentum spread. Furthermore an integral element of many atom optics experiments is an atomic beamsplitter as it enables atomic coherence effects to be probed. A typical application is an atom interferometer [77]. A range of experimental methods have been devised to provide these essential capabilities. Probably the first atomic beamsplitter was the Stern–Gerlach experiment which separated atoms according to their spin state in a static magnetic field [78]. Nanofabrication technology enabled the production of micro-gratings which were used to diffract an atomic beam [79]. Furthermore diffraction of atoms at an optical standing wave was utilized [80–82] and a reflection light grating was proposed to facilitate atomic diffraction utilizing a standing evanescent wave [83]. Recently coherent beamsplitting of a Bose–Einstein condensate was demonstrated by diffracting atoms at a pulsed optical standing wave [84] and by optically induced Bragg diffraction [85]. A way to use a time-modulated potential to split an atomic wavefunction coherently was illustrated by a group led by Jean Dalibard where atoms are reflected at an intensity modulated [86] or pulsed [87] evanescent wave.

In this section solutions are presented that involve the interaction of atoms with an amplitude modulated standing wave which operates outside the Raman–Nath regime because the transverse motion of the atom during its passage through the standing wave is not negligible. These methods are carried out with light having large detuning from the atomic resonance frequency to prevent decoherence due to incoherent absorption and spontaneous-emission processes which would add dissipation to the system and destroy existing atomic coherence. Two experimental methods are presented using different dynamical features which can be utilized for momentum preparation and ensemble beamsplitting. It should be noted that, in contrast to the atomic beamsplitters presented above, here the beamsplitting is an ensemble effect, meaning that an atom goes either one way or the other depending on its initial position (at least for relatively small values of Planck's constant for which results are presented below). The beamsplitter outputs are not due to atoms being in a superposition of moving in both directions simultaneously. However, the process is non-dissipative (due to large detuning from the atomic resonance and the short experimental timescales) and therefore no random processes destroy the atomic coherence.

6.2. Momentum preparation and ensemble beamsplitter using regular dynamics

In section 4.2 it was shown that the momentum of the resonances is determined by the value of the modulation frequency when the modulation amplitude ε and the modulation parameter κ are kept constant. It was also shown that it is possible to cover a wide momentum range by adjusting the modulation frequency ω. As an example figure 13 shows a velocity range from 7–30 recoil momenta. This provides the opportunity for rough momentum selection. Note that one disadvantage of this method is the fact that the momentum spread of the atoms contained in the resonances is proportional to the modulation frequency.

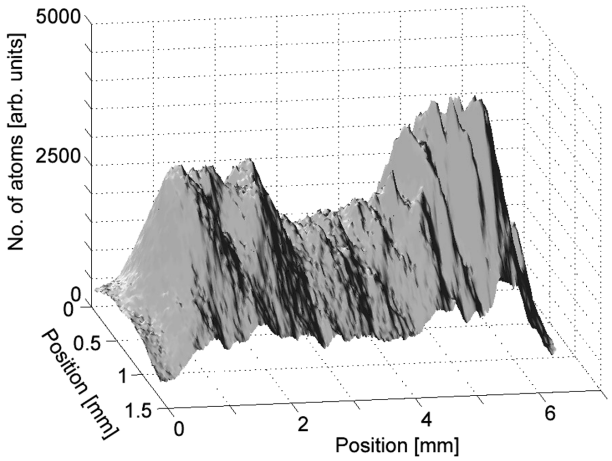

Figure 22. Peaks in the atomic momentum distribution resulting from atoms loaded into regions of regular motion of the quantum driven pendulum. Up to around 65% of the atoms can be loaded into distinct peaks in the atomic momentum distribution. These data were obtained at modulation parameter $\varepsilon = 0.27$, modulation frequency $\omega/2\pi = 900$ kHz and scaled well depth $\kappa \approx 0.25$.

Furthermore the scaled theory predicts that the momentum of the resonances is slightly dependent on the modulation amplitude ε, as shown in figure 11. The resonance momentum is also strongly dependent on the scaled well depth κ, as can be seen in figures 12 and 21. The disadvantage of trying to change the resonance momentum by means of changing either ε or κ is that the size of the regions of regular motion (amplitude of the peak in the atomic momentum distribution) as well as the momentum spread change dramatically when changing these two parameters. Therefore changing either of these parameters does not represent an efficient solution to control the momentum of an atomic ensemble.

A far more efficient way was developed to control the momentum of an atomic ensemble. The momentum of the resonances and their associated peaks in the atomic momentum distribution can be well controlled by changing the interaction time with the modulated standing wave (endphase of the modulation). Choosing an appropriate scaled well depth κ and modulation parameter ε one can load up to 65% of all atoms into distinct peaks in the atomic momentum distribution. This determines the efficiency of the method to be presented. Figure 22 shows an experimental atomic position distribution after 10 ms ballistic expansion time. Here the two resonances were measured to move with a momentum of 30.25 recoils. The method to be introduced here does not rely on changing any of the parameters $\kappa, \omega, \hbar$ or ε. In the method the modulated standing wave is turned off at different times, not necessarily when the resonances are positioned on the momentum axis. This corresponds to a rotation of the resonances by up to 45° from the observation position on the momentum axis, as can be seen in figure 23. Each set of equal numbers corresponds to a

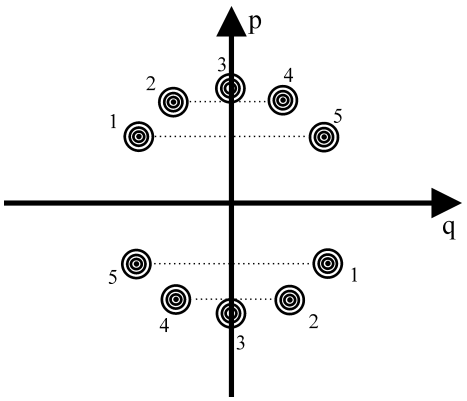

Figure 23. Rather than turning the standing wave off when the resonances are positioned on the momentum axis (position 3), the standing wave can be turned off slightly before or after that time. This corresponds to a rotation of the resonances by up to 45° (positions 1, 2, 4, 5) in phase space. Note the symmetry of positions 2 and 4, and 1 and 5.

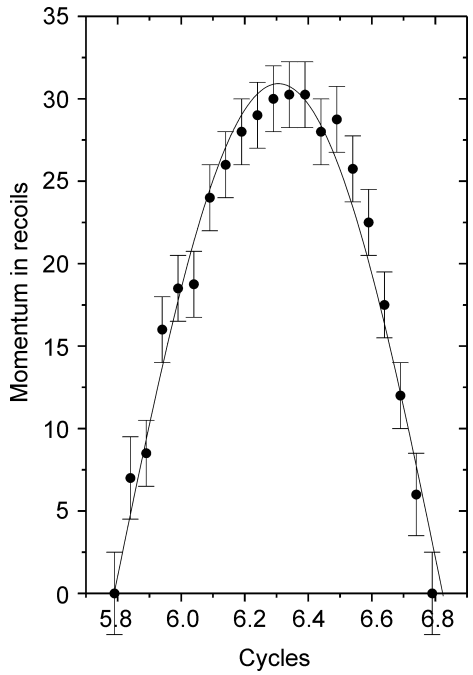

Figure 24. Experimental data showing the momentum of the distinct peaks in the atomic momentum distribution for different end phases of the modulated standing wave. 6.37 cycles correspond to turning off the standing wave at a modulation minimum. The data shown here were obtained at modulation frequency $\omega/2\pi = 900$ kHz, modulation parameter $\varepsilon = 0.27$ and scaled well depth $\kappa \approx 0.25$. A sinusoidal fit is within the error bars.

certain rotation of the resonances due to turning off the standing wave at a different modulation phase. Using this method a momentum range of 35 recoils was achieved which could be extended even further by increasing the modulation frequency. Figure 24 shows the experimentally obtained momenta for different end phases of the modulation signal. The curve is approximately symmetric around 6.37 cycles (rather than 6.5 cycles, accounting for the finite turn-on time of the acousto-optic modulator) at which time the resonances are positioned on the momentum axis. A sinusoidal fit is included to show

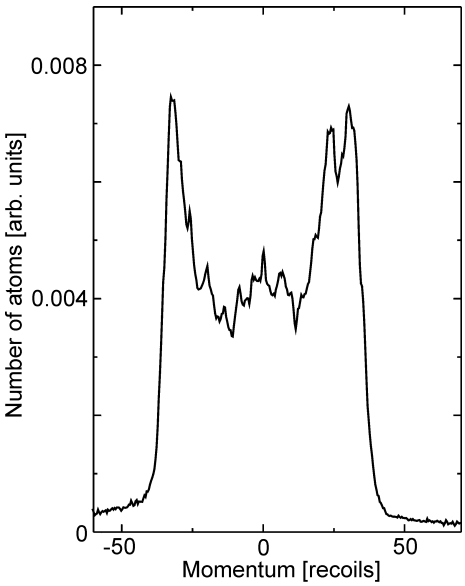

Figure 25. Atomic momentum distribution resulting from the chaotic transients of the system. The peaks have a momentum of 33 recoils and the data were obtained at modulation frequency $\omega/2\pi = 360$ kHz, modulation parameter $\varepsilon = 0.30$, scaled well depth $\kappa = 0.31$ and after an interaction time of 1.75 modulation periods.

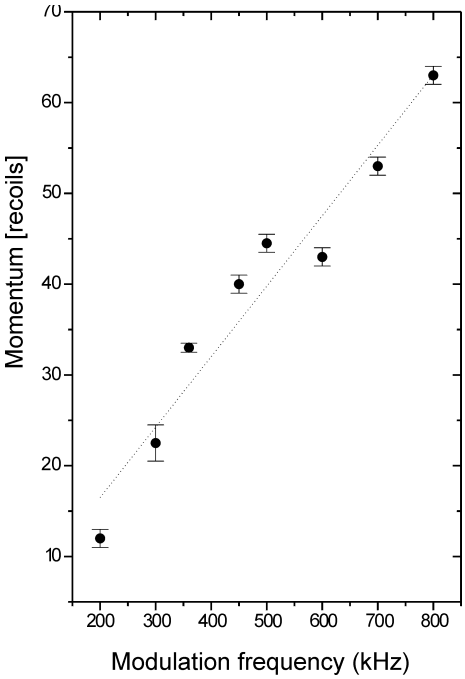

Figure 26. Control of the momentum of the chaotic transients using the modulation frequency. Momenta between 10–70 recoils can be achieved. The momentum is approximately a linear function with respect to the modulation frequency.

that this momentum control mechanism can be explained by the rotation of the resonances in phase space. Note the two-cycle symmetry of this experiment, due to the fact that the resonances which are utilized are period-2 resonances. Figure 18 shows multiple momentum distributions after different interaction times, providing an example for this momentum control mechanism.

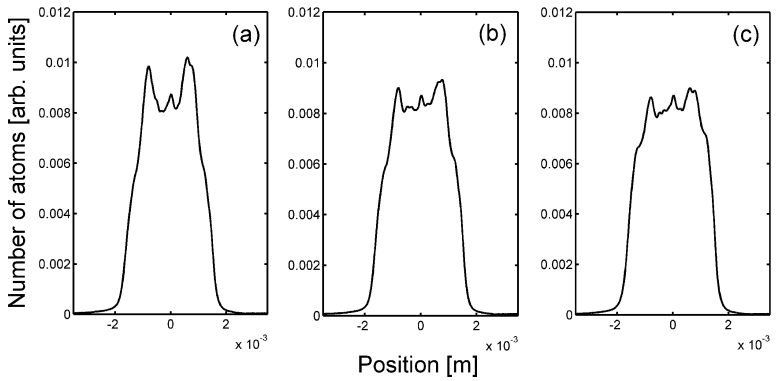

Figure 27. Atomic position distribution after different interaction times with the modulated standing wave. Period-1 regions of regular motion correspond to peaks in the position distribution after 6.25 modulation periods as shown in (a). (b) shows the position distribution after 10.25 modulation periods. Period-1 regions of regular motion can still be observed after 99.25 modulation periods, as shown in (c).

6.3. Momentum preparation and ensemble beamsplitter using transient dynamics

In the discussion of dynamical resonances it is important to avoid confusion with transient dynamics which are exhibited in the dynamics of atoms in an amplitude modulated standing wave in a similar experimental set-up. Such transient dynamics can also be used to implement momentum preparation and ensemble beamsplitting. Figure 25 shows a typical momentum distribution which results from transient dynamics of the system. Two distinct peaks contain up to approximately 60% of all atoms. These particular data were taken at a modulation frequency $\omega/2\pi = 360$ kHz, modulation parameter $\varepsilon = 0.30$ and scaled well depth $\kappa \approx 0.31$. While phase space resonances need at least 4.5 cycles to become apparent in the atomic momentum distribution, the transients occur after only 1.75 modulation periods (cycles) with an Hamiltonian of the form $I_0(1 + 2\varepsilon \sin \omega t)$ (starting phase of the modulation zero going up). The dynamics can be explained classically by following the trajectories of atoms initially equally spaced inside a potential well [88]. Only considering atoms equally spaced on one side of the well, e.g. in between the intensity minimum and the left maximum of one well, a significant number of atoms climb to the right maximum of the potential well after one modulation period. While the potential starts rising again the atoms 'surf' down the well for the final 0.75 periods of the modulation. Solving Hamilton's equations one can see that these atoms form a narrow velocity band, which can be observed in the final atomic momentum distribution. The same applies for atoms initially spaced on the other side of the well forming the second distinct peak in the atomic momentum distribution after interacting with the modulated standing wave. As can be seen from figure 25 these peaks have a small momentum spread, making them a good means to prepare atoms with a certain momentum.

It was found experimentally that the transients can be observed only for certain values of light intensity, detuning and modulation frequency. An approximate condition is given by

$$\sqrt{\frac{I}{\delta}}\frac{1}{\omega} = \varsigma \tag{77}$$

where I is the light intensity, δ is the detuning of the standing wave, ω is the modulation frequency and ς is an atom-specific constant (dependent on saturation intensity, spontaneous lifetime, wavenumber of the standing wave and mass of the atom). This relation was obtained by changing the modulation frequency and detuning of the modulated standing wave. The condition is the equivalent of requiring the scaled well depth κ to be constant ($\kappa = 0.3$).

The momentum of the transient peaks is a function of the modulation frequency. One can easily vary the momentum from 12 to over 60 recoil momenta by adjusting the modulation frequency (and detuning). Figure 26 shows the momentum of the transient peaks as a function of the modulation frequency. A significant momentum range can be covered by changing the modulation frequency. The momentum is approximately a linear function with respect to the modulation frequency. Characterization of the coherence properties of both momentum preparation methods was outside the scope of the work presented here and could be a subject of future studies.

7. Long term dynamics and dynamics due to selective loading

7.1. Long term dynamics

The observation of resonances for a minimum length of interaction time with the modulation potential is a prerequisite to observe dynamical tunnelling (dynamical tunnelling will be discussed in detail in section 9) as it is necessary to observe at least a significant part of the tunnelling period to have sufficient evidence for tunnelling to occur. Tunnelling periods strongly depend on a number of system parameters. Theoretical calculations have shown that 100 periods of the modulation frequency are sufficient to observe at least one tunnelling period. Figure 27 shows three atomic position distributions for scaled well depth $\kappa \approx 1.1$, modulation parameter $\varepsilon = 0.25$ and modulation frequency $\omega/2\pi = 300$ kHz with the two period-1 regions of regular motion as distinct peaks in the atomic momentum distribution. In figure 27(a) the atoms have interacted for 6.25 periods of the modulated standing wave. After an interaction time of 10.25 modulation periods the atomic position distribution has already changed shape as the peaks corresponding to period-1 regions of regular motion are smaller. This is shown in figure 27(b). There is a smooth transition between the atomic position distributions shown

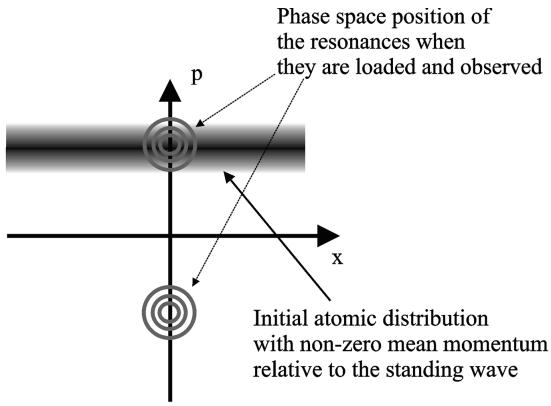

Figure 28. Poincaré section for selective loading of only one region of regular motion. The required initial atomic momentum distribution has non-zero mean momentum.

in figures 27(a) and (b). This can be seen for a different set of parameters in figure 8. Peaks in the atomic position distribution corresponding to regions of regular motion can still be observed after 99.25 modulation periods, as shown in figure 27(c). There is no significant difference between the position distributions for an interaction time of 10.25 modulation periods and 99.25 modulation periods, indicating that the dynamics have approximately equilibrated after 10.25 modulation periods and that the system is sufficiently isolated from noise to experimentally observe regions of regular motion even after 99.25 modulation periods. The observation of regions of regular motion for such a long interaction time is an important step towards the observation of dynamical tunnelling.

7.2. Experimental set-up for selective loading

In order to observe dynamical tunnelling selective loading of only one region of regular motion is necessary. To load both regions of regular motion the starting phase of the standing wave modulation is chosen in such a way that the resonances are located on the position axis in the Poincaré section (atom groups 1 and 2 have zero velocity, see figures 5 and 6). To selectively load only one resonance, the starting phase of the standing wave is adjusted such that the resonances are located on the momentum axis. For a period-1 region of regular motion the starting phase needs to be either maximum or minimum modulation amplitude. Atoms can be prepared with a mean momentum relative to the standing wave equal to the momentum of one of the regions of regular motion when it is located on the momentum axis. If the width of the initial distribution is sufficiently small only one of the regions of regular motion will be loaded. Figure 28 shows the required position of the regions of regular motion in a Poincaré section along with the initial atomic distribution whose mean momentum is equal to the momentum of one of the regions of regular motion. The experimental set-up used to achieve this is shown in figure 29. It is similar to the one shown in figure 1 but differs after the beam has passed through acousto-optic modulator AOM_2. Rather than coupling the beam straight into the vacuum chamber, a polarizing beamsplitter cube is used to produce two beams of equal intensity, which are needed to produce the optical standing wave. A half-wave plate is

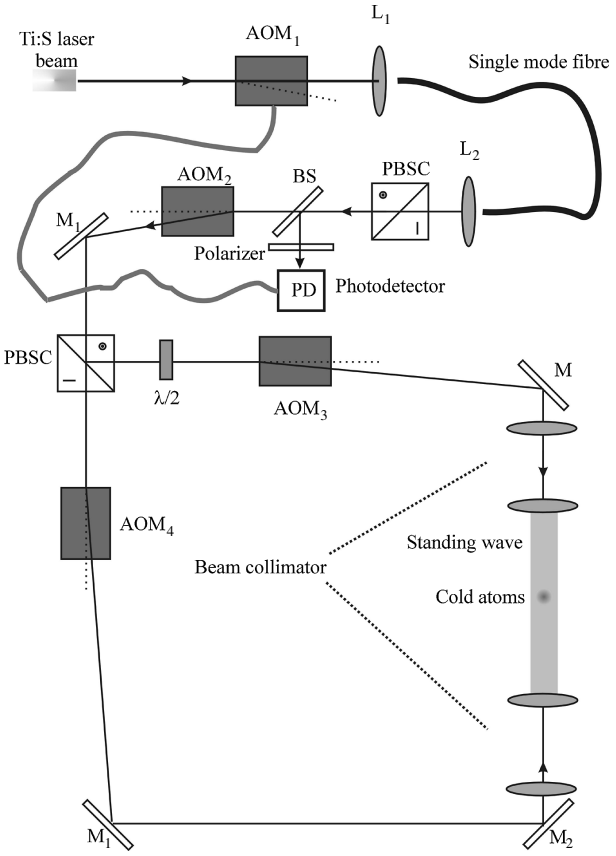

Figure 29. Set-up for selective loading of only one region of regular motion. A polarizing beamsplitter cube is used to produce the two arms of the standing wave that is produced using a configuration similar to that of a Sagnac interferometer. Acousto-optic modulators AOM_3 and AOM_4 are used to induce a small frequency difference in the two arms, resulting in a slowly moving standing wave. The half-wave plate ($\lambda/2$) is used to obtain the same polarization in both arms. Telescopes on both sides of the vacuum chamber ensure the appropriate beam diameter for both beams.

inserted into one of the beams to obtain the same polarization in both arms. There are several ways to prepare the atomic cloud with a non-zero velocity relative to the inertial frame of the standing wave. Here a method is used giving the standing wave a constant velocity relative to the initial stationary cloud of cold atoms. This is achieved by detuning one of the beams relative to the other. The velocity of the standing wave c_{st} is given in terms of the detuning $(\omega_1 - \omega_2)$ by the following condition:

$$c_{st} = \frac{\omega_1 - \omega_2}{2k} \tag{78}$$

where k is the wavenumber and ω_1 and ω_2 are the frequencies of the two counterpropagating beams. For the experiments $\omega_1 - \omega_2 \approx 200$ kHz is required, which is achieved by utilizing an acousto-optic modulator in each counterpropagating beam (AOM_3 and AOM_4) and detuning them relative to each other. The detuning (and therefore the velocity of the standing wave) is adjusted using an IntraAction dual-frequency-synthesizer driver (model DFE). The frequency stability is 1 ppm, which is achieved using a temperature compensated crystal oscillator. The frequency is set in one channel at 40 MHz and can be

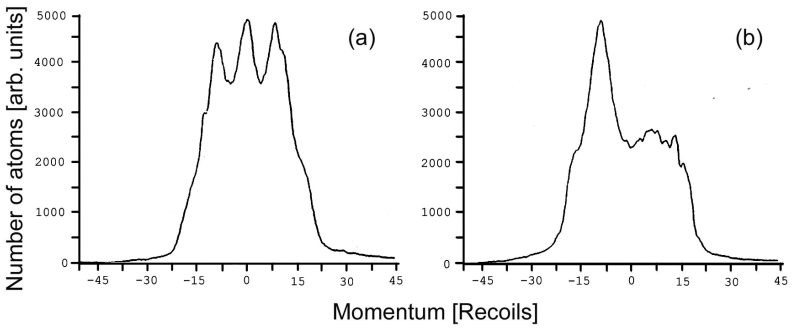

Figure 30. (a) Atomic momentum distribution with three distinct peaks corresponding to two period-1 regions of regular motion (left and right peak) and the central island of stability (centre peak). (b) Selective loading of one region of regular motion. The pedestal corresponds to atoms which are loaded into the classical chaotic region.

adjusted in the other from 30–50 MHz in steps of 0.1 kHz. The two beams are overlapped inside the vacuum chamber to form a standing wave. The atomic dynamics proved to be very sensitive to the overlap of the two beams, so great attention was given to the alignment procedure. There are two important factors in the procedure. First it is important to achieve maximum overlap of the atomic cloud and the standing wave, and second it is important that the standing wave beams are as parallel as possible and that they have maximum overlap with each other. Typically the first beam is aligned by blowing the atoms out of the trap with the same procedure as outlined in section 2.1. To overlap both laser beams, apertures on both sides of the vacuum chamber were used for initial alignment. In the next step a set of two mirrors on the side of the vacuum chamber where the other beam originates is used for further alignment. A piece of lens tissue is placed on one of the two mirrors (M_1) and one of the beams is walked with the other mirror (M_2) such that the two spots overlap on M_1. Then the procedure is carried out with the lens tissue on M_2 and M_1 is used for aligning the other beam, trying to obtain overlap on M_2. Multiple iterations of this procedure lead to a fairly accurate overlap of the two beams. Light emerging from the unused port of the polarizing beamsplitter cube forms several distinct spots in the far field. Overlap of these spots was utilized as an additional alignment aid. Finally the diffraction spots of the back-reflected light through acousto-optic modulator AOM_2 are observed just before the single-mode optical fibre and used for final alignment.

7.3. Selective loading of one region of regular motion

Experimental results illustrating selective loading of one region of regular motion are shown in figure 30. Figure 30(a) shows an atomic momentum distribution with three distinct peaks resulting from two period-1 regions of regular motion and the central island of stability for scaled well depth $\kappa \approx 1.25$, modulation parameter $\varepsilon = 0.31$ and modulation frequency $\omega/2\pi = 300$ kHz. In figure 30(b) the initial phase of the standing wave modulation is changed so that the regions of regular motion are initially located on the momentum axis and a slowly moving standing wave is used with a frequency difference $\omega_1 - \omega_2 = 243$ kHz, where ω_1 and ω_2 are the frequencies of the two counterpropagating beams. The momentum distribution has the form of a pedestal with only one distinct peak at negative momentum. This peak corresponds to one period-1 region of regular motion. This was confirmed by changing the interaction time with the modulated standing wave by half a modulation period so that the peak rotates in phase space, now having positive momentum. The way in which selective loading is implemented here also results in loading of the classical chaotic region of phase space (see figure 28). The pedestal in the atomic momentum distribution corresponds to atoms which are part of the classical chaotic region of phase space.

Extensive experiments were undertaken studying the dynamics of atoms which were initially loaded into only one region of regular motion using the method described above. The purpose was to test whether it is possible to observe dynamical tunnelling using a thermal Rb cloud with a kinetic temperature of 8 μK and the loading scheme as described above. To obtain experimentally accessible timescales for the observation of one tunnelling period it is important to maximize the scaled Planck's constant $\bar{k}$. This can be achieved by choosing a small value of the modulation frequency $\omega/2\pi$. However, the momentum of the resonances scales linearly with the modulation frequency (as illustrated in section 4.2, see figure 13), so that there is a limit on how small the modulation frequency can be chosen before the peaks in the atomic momentum distribution cannot be resolved anymore. Using a longer ballistic expansion time (up to 20 ms) the limit was found to be a modulation frequency of approximately 100 kHz. Figure 31(a) shows two atomic position distributions for scaled well depth $\kappa \approx 1.35$, modulation parameter $\varepsilon = 0.32$ and modulation frequency $\omega/2\pi = 200$ kHz. A ballistic expansion time of 15 ms is used to improve the resolution of the peaks in the atomic position distribution. The two arms of the standing wave have a frequency difference $\omega_1 - \omega_2 = 180$ kHz. The black curve is taken for an interaction time of 8 modulation periods and the grey curve is taken after 100 modulation periods. After 100 modulation periods the peak corresponding to the initially loaded region of regular motion has a decreased amplitude while the momentum distribution has a larger amplitude at positive momentum. This could possibly be a signature of dynamical tunnelling but may also be due to diffusion processes. In (b) the grey curve is the position distribution after 100 modulation periods and the black curve was taken after 100.5 modulation periods. These data were taken to test the period-1 character of motion which is apparent as some atoms reverse their momentum.

A few comments should be made about loading and observation phases of the standing wave modulation.

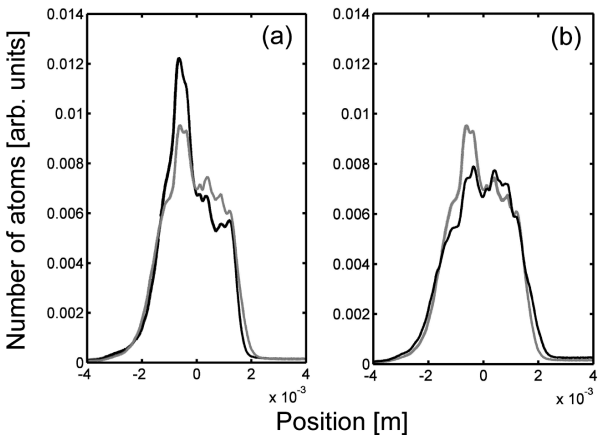

Figure 31. Dynamics due to selective loading of one region of regular motion for scaled well depth $\kappa \approx 1.35$, modulation parameter $\varepsilon = 0.32$ and modulation frequency $\omega/2\pi = 200$ kHz. (a) The black curve is the atomic position distribution measured after an interaction time of 8 modulation periods and the grey curve is taken after 100 modulation periods. In (b) the grey curve is the position distribution after 100 modulation periods and the black curve was taken after 100.5 modulation periods. Some atoms are reversing their momentum, confirming the period-1 character of motion.

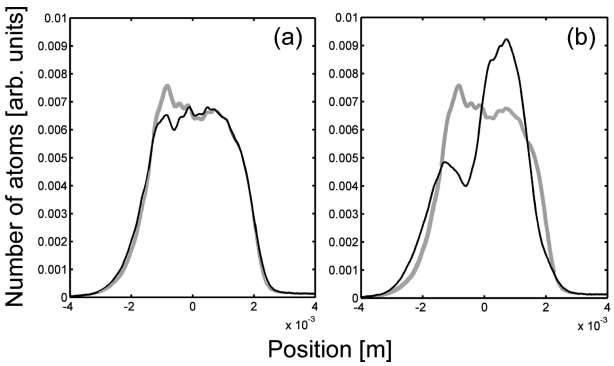

Figure 32. Atomic position distribution after different interaction times with the modulated standing wave for scaled well depth $\kappa \approx 1.35$, modulation parameter $\varepsilon = 0.32$ and modulation frequency $\omega/2\pi = 100$ kHz. In (a) the grey curve corresponds to an interaction time of 10 modulation periods and the black curve corresponds to 100 modulation periods. (b) shows atomic position distributions for 10 modulation periods (grey curve) and 700 modulation periods (black curve). The emergence of the left peak in the black curve is due to the atoms which exhibit unbound and librational motion. For dynamical tunnelling one expects the emergence of a peak on the right. Therefore this second peak does not mimic dynamical tunnelling.

Especially at small values of the modulation frequency it is impossible to avoid loading librational motion and unbound motion along with loading one region of regular motion as the initial atomic momentum distribution has a large width compared to distinct phase space features like period-1 regions of regular motion, and the separation between unbound motion, librational motion and period-1 regions of regular motion is small. Especially for large interaction times this leads to an important effect which needs to be considered carefully when trying to observe dynamical tunnelling. For short interaction times the position distribution after the ballistic expansion time is equivalent to the momentum distribution before the ballistic expansion period. However, for long interaction times atoms which are part of the librational and unbound motion spatially separate from the atoms which are part of the bound motion in each individual well during the interaction time with the standing wave. They form a separate peak in the atomic position distribution. This new peak could be mistakenly interpreted as the occurrence of dynamical tunnelling even though it is only the result of the spatial separation of unbound motion and the convoluted bound single well motion of the many wells of the standing wave. To enable the observation of dynamical tunnelling the loading and observational phase of the standing wave modulation have to be chosen such that this unbound motion peak moves in the opposite direction from the peak which would result from atoms tunnelling into the other region of regular motion. This was experimentally implemented by starting and ending the standing wave modulation at minimum and choosing the sign of the frequency difference between the two standing wave beams such that a region of regular motion with negative momentum is loaded initially. Figure 32(a) shows two position distributions for scaled well depth $\kappa \approx 1.35$, modulation parameter $\varepsilon = 0.32$, modulation frequency $\omega/2\pi = 100$ kHz and a ballistic expansion time of 20 ms. The two arms of the standing wave have a frequency difference $\omega_1 - \omega_2 = 130$ kHz. The grey curve is taken after an interaction time of 10 modulation periods with the modulated standing wave and the black curve corresponds to an interaction time of 100 modulation periods. After 100 modulation periods there seem to be more atoms with positive momentum, which could be an indication of dynamical tunnelling. Figure 32(b) shows two position distributions for the same parameters but now the black curve corresponds to an interaction time of 700 modulation periods. There are two distinct peaks. The one on the left corresponds to unbound and librational motion while the right peaks correspond to the convolution of bound motion in individual wells. The right peak has a smaller width compared to the distribution after 10.25 modulation periods (grey curve) because the ballistic expansion time is only 13 ms compared to a ballistic expansion time of 20 ms for the black curve. As the beginning and end phase of the standing wave as well as the sign of the detuning between the two standing wave arms are appropriately chosen, the emergence of this additional peak does not mimic dynamical tunnelling as it appears with opposite momentum compared to the peak that would result from atoms that tunnel into the other region of regular motion. The big peak on the right corresponds to the convolution of bound motion.

8. Experiments utilizing a sodium Bose–Einstein condensate

8.1. Introduction

Here experiments are described which utilize a sodium Bose–Einstein condensate. The observation of dynamical tunnelling is much easier to achieve utilizing a Bose–Einstein condensate rather than using a thermal cloud of atoms. The condensate can be prepared in an exact quantum state rather than as a statistical ensemble of many states, which is the case for a thermal cloud. This accounts for one of the fundamental differences between

experiments with a thermal atomic cloud and a Bose–Einstein condensate.

The quasi-momentum plays a significant role in the experiments. The quasi-momentum ϑ is approximately equal to the relative velocity v between the wavepacket (before the lattice is turned on) and the lattice, $v = \vartheta/m$ (modulo $2\hbar k/m$) [89], if the standing wave is adiabatically turned on. It was found that it is of importance to populate a state with quasi-momentum equal to zero and small quasi-momentum spread to observe dynamical tunnelling. The details of the relevant Floquet theory are explained in [62]. However, at this point it should be noted that the presence of two highly localized Floquet states of opposite parity can explain the dynamical tunnelling process. As will be discussed in [62] the quasi-eigenenergies of these two contributing Floquet states sensitively depend on the quasi-momentum (or Bloch angle). Therefore the tunnelling period (which is inversely proportional to the separation between these two quasi-eigenenergies) sensitively depends on the quasi-momentum. Using a thermal atomic cloud one obtains a statistical ensemble of many quasi-momenta. Atoms localized in individual wells can be described by a wavepacket in the plane wave basis and therefore they are characterized by a superposition of many quasi-momenta. The resulting quasi-momentum width washes out the tunnelling oscillations. In fact, in another experiment carried out in parallel to the experiments described in this section, Steck *et al* [90] found that the amplitude of the mean momentum oscillations resulting from a tunnelling process between two librational islands of stability decreased when the initial momentum width of the atomic cloud was increased. In that experiment a velocity-selective Raman process was used [91] to produce the initial atomic wavefunction.

8.2. Experimental procedure

A detailed account of the experimental realization of Bose–Einstein condensation is presented in the seminal papers by Anderson *et al* [92] and Davis *et al* [93]. Here only a short overview is presented which contains details relevant to the tunnelling experiments. The experimental procedure to prepare atoms to be localized around one of the regions of regular motion (as a superposition of Floquet states associated with one of the fixed points as explained in [62]) is implemented as follows: sodium atoms are produced in an effusive sodium oven inside a low vacuum chamber ($P = 10^{-9}$ Torr). The atoms are slowed down using a Zeeman slower and loaded into a magneto-optic dark-spot trap [94] which is formed inside a ultra-high vacuum Pyrex cell vacuum chamber ($P = 10^{-11}$ Torr).

The atoms are transferred into a magnetic quadrupole field. Atoms in the $3S_{1/2}$, $F = 1, m_F = -1$ state are trapped, compressed and then cooled by rf-induced evaporation. A time-averaged orbiting potential (TOP) [95] trap is utilized to prevent Majorana spin flips. After the Bose–Einstein condensate has formed with approximately 3×10^6 sodium atoms, the condensate is adiabatically expanded, resulting in trapping frequencies which are $2\omega_x = \sqrt{2}\omega_y = \omega_z = 2\pi \times 33$ Hz, which, using a scattering length of 2.8 nm, result in calculated Thomas–Fermi diameters of 83, 57 and 42 μm, respectively. The expansion was performed to ensure

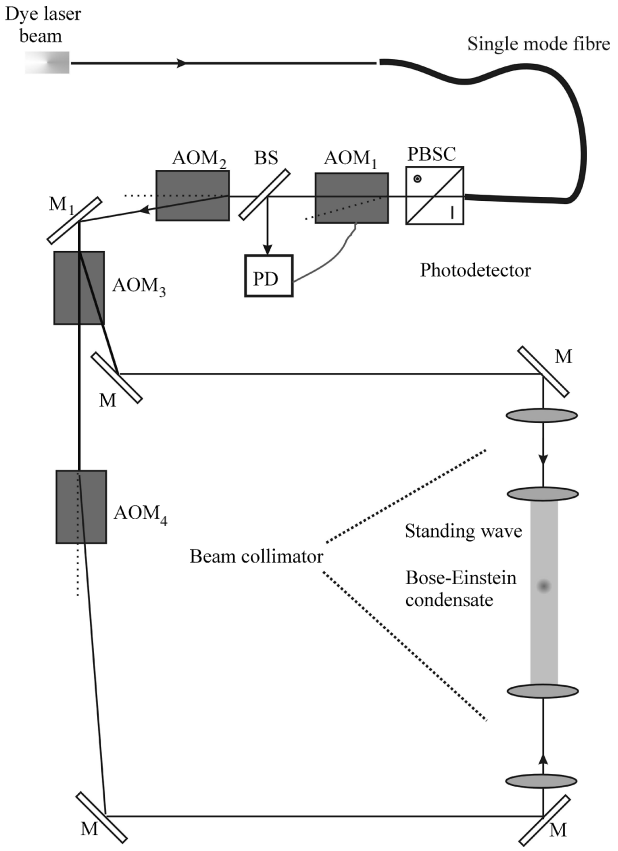

Figure 33. Set-up for the optical standing wave. A dye laser passes through a single-mode polarization preserving optical fibre and through a polarizing beamsplitter cube. A small amount of light is reflected from the main beam and its intensity is measured using a photodetector whose signal is connected to a feedback circuit which controls acousto-optic modulator AOM_1, resulting in an intensity-stabilized laser beam. AOM_2 provides the intensity modulation and AOM_3 acts as a beamsplitter. The standing wave can be shifted using AOM_4. Telescopes on both sides of the vacuum chamber focus the beams into the centre of the vacuum chamber and produce the desired beam waist.

that the atomic density is low, resulting in negligible mean field interaction. The mean field energy was calculated to be approximately 400 Hz compared to a kinetic energy of the order of 10^5 Hz.

A schematic diagram of the experimental set-up for the modulated standing wave is shown in figure 33. The standing wave is produced by a dye laser operating at a wavelength $\lambda = 589$ nm. The laser beam passes through a single-mode polarization preserving fibre. After passing through the fibre, the light is passed through an acousto-optic modulator AOM_1 which deflects a small amount of light which is varied in order to stabilize the light intensity. It is controlled by a feedback circuit which receives a signal from the photodetector (PD) measuring the intensity of the light. Intensity fluctuations are reduced to approximately 5% (of the total intensity). The light is passed through a second acousto-optic modulator AOM_2 which provides the required intensity modulation. A third 80 MHz acousto-optic modulator AOM_3 is used as beamsplitter to provide two beams used for the configuration which makes up the optical standing wave. Finally a fourth 80 MHz modulator AOM_4 equates the frequency in both arms and provides the capability to shift the optical standing wave.

The condensate is released from the magnetic trap and a 1D standing wave lattice is adiabatically turned on along x with a turn-on time of 50 μs. An approximate criterion for adiabaticity is that the ramping time should be much longer than the inverse bandgap frequency (separation between the lowest and the third lowest band) divided by (2π) [89]. Although the turn-on signal is programmed to be a linear ramp, the start and end part of it are smoothed out due to the transfer function of the acousto-optic modulator. According to calculations[3] a true 50 μs linear turn-on is significantly less adiabatic than what was observed in the experiments presented here. However, when including the transfer function of the AOM into theoretical simulations the adiabaticity of the turn-on increases significantly. The atoms are loaded into the bottom of the lowest band (quasi-momentum equal to 0) of the optical lattice. It was verified that >99% of the atomic population is in the lowest band using the following measurement. The standing wave is turned on adiabatically as described above and the momentum distribution is measured as a function of the interaction time with the unmodulated standing wave. If the atoms are truly loaded into the ground state the atomic momentum distribution will be independent of the interaction time as the ground state is an eigenstate of the system. If the turn-on is not perfectly adiabatic a small portion of the atoms will be in an excited band (most likely the second excited band as it has the same parity as the ground state). Since the excited band has a different energy, its phase will precess with respect to the ground state and, depending on when the lattice is turned off, a different momentum distribution will result. This measurement is very sensitive to the excited population because it incorporates an interference effect. Both the ground band ($n = 1$) and the excited band ($n = 3$) have some projection onto the $p = 0$ plane wave state (the central peak in the diffraction pattern). Therefore the $p = 0$ population should scale approximately as $|a_1 + a_3 \exp(\mathrm{i}(E_1 - E_3)t/\hbar)|^2$, where a_1 and a_3 are the projections of the $n = 1$ and 3 band onto the $p = 0$ plane wave state and E_1 and E_3 are the eigenenergies for bands 1 and 3, respectively. A 10% peak-to-peak variation was detected in the $p = 0$ peak, which corresponds to about 0.5% population in the excited state.

The Gaussian lattice beams are detuned ~14 GHz above the atomic D2 resonance ($\lambda = 589$ nm) and have a waist $w \approx 250$ μm, leading to an intensity variation of less than 5% across the atomic cloud. The waist of the standing wave is set by observing the beam profile of one of the (for this purpose attenuated) standing wave beams using a CCD camera that is focused halfway between the two opposite chamber windows. The telescope through which the laser beam passes is adjusted to obtain the appropriate beam waist. The procedure is repeated for the other beam.

The scaled well depth κ is determined by measuring the oscillation frequency of the atoms in the unmodulated standing wave. To measure the oscillation frequency the standing wave is adiabatically turned on so that the BEC localizes at the bottom of each well. Then the standing wave is suddenly shifted and the resulting oscillations are analysed by measuring the atomic momentum distribution after various interaction times. A one-dimensional band structure calculation [96] is carried out with the condition to produce a lattice with the energy separation between the two lowest bands equal to Planck's constant times the oscillation frequency of the atoms in the unmodulated case. From this calculation the scaled well depth κ is determined. The induced phase shift is chosen to be very small ($0.08 \times 2\pi$ or 1.02 ns) so as to involve only the lowest two bands in the oscillation. The uncertainty in the measurement of the scaled well depth κ is due to uncertainty in measuring the oscillation frequency and to variations in the laser intensity and was determined to be 10% (all reported uncertainties are one standard deviation combined systematic and statistical uncertainties). For the parameters which were used in the experiment the standing wave contains approximately between three and five bound states, depending on whether the modulation is at minimum or maximum. Detailed studies of the dynamics of Bose–Einstein condensates in optical lattices, which study these mechanisms in more detail, were undertaken by Denschlag *et al* [89].

Selective loading of one region of regular motion requires a sudden[4] phase shift of the standing wave so that the wavepacket, which was initially localized at the bottom of the well, is placed approximately halfway up one side of each well when the amplitude modulation of the standing wave is commenced. To induce the phase shift a circuit with switchable and variable path length is utilized to drive acousto-optic modulator AOM_4, as shown in figure 34. The RF source is connected to a 50/50 power splitter. The path lengths between each of the two outputs and the RF amplifier are different. The pathlength is variable in one arm. The two arms are connected to RF switches. The switches have two outputs each, one of them leading to a 50 Ω dummy load and the other to the RF amplifier. The TTL control input to the switches C determines whether the output occurs at output O1 or O2 of each switch. O1 of the first switch and O2 of the second switch are connected to the 50 Ω load and O2 of the first switch and O1 of the second switch are connected to the RF amplifier. By turning on or off a TTL pulse at the control input C of each switch one can therefore choose whether the RF signal travelling through arm 1 or 2 is connected to the RF amplifier and fast switching between the two arms is possible. The phase shift between the two signals is visualized on a fast oscilloscope and the variable path length is adjusted to provide a pathlength difference of typically 2.68 ns (using an 80 MHz acousto-optic modulator, this corresponds to a phase shift of $0.21 \times 2\pi$), which will place the initial wavepacket just below halfway up each standing wave well. This overlaps it with one region of regular motion.

Each individual well contains a minimum uncertainty wavepacket with an rms position and momentum spread of 0.6 in scaled units (calculated using the numerical solution of the Gross–Pitaevskii equation). To load selectively only the region around one resonance, the position of the standing wave is suddenly shifted by inducing an appropriate phase shift with acousto-optical modulator AOM_4 (see figure 33) as explained before. Shortly (100–300 ns) before the phase shift (at $t = 0$), modulation of the intensity of the standing wave commenced at a modulation frequency $\omega/2\pi = 220$–320 kHz. The start phase of the modulation of the standing wave is chosen so that

[3] Personal communication: Paul Julienne, National Institute of Standards and Technology.

[4] Sufficiently fast so that the atoms find themselves stationary halfway up one side of the well after the phase shift has occurred.

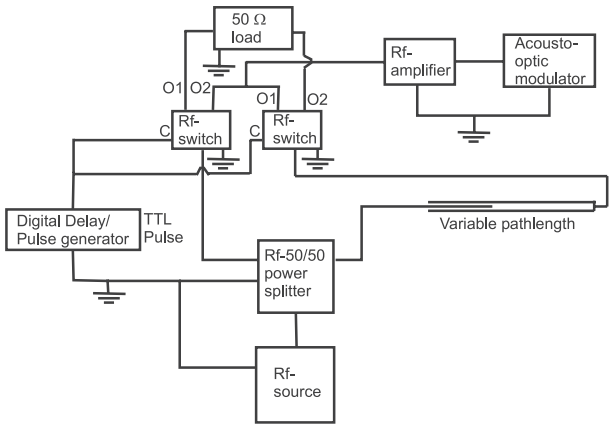

Figure 34. RF circuit with switchable and adjustable pathlength. The signal from the RF source is divided equally by a power splitter into two arms with different pathlengths. The pathlength in one arm can be adjusted. A digital delay/pulse generator is connected to the control input C of two RF switches, which are located in both arms. Output O1 of the first switch and O2 of the second switch are connected to a 50 Ω load and O2 of the first switch and O1 of the second switch are connected to the RF amplifier. By turning on or off a TTL pulse at the control input C of each switch one can therefore choose whether the RF signal through arm 1 or 2 is connected to the RF amplifier and fast switching between the two arms is possible. The RF amplifier is connected to acousto-optic modulator (AOM_4 in figure 33).

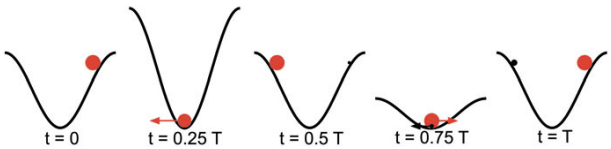

Figure 35. Schematic of period-1 resonances of an atom in an amplitude modulated sinusoidal potential. These resonances correspond to atomic motion that remains phased to the modulation frequency. The anharmonicity of the sinusoidal potential is compensated by the amplitude modulation for atoms around these resonances, creating the regions of regular period-1 motion shown. The appearance of the second ball depicts tunnelling into the initially empty resonance. T is the modulation period.

the resonances are located on the position axis of the Poincaré section, as shown in figure 6(b) (start phase of the standing wave modulation is zero modulation amplitude with amplitude increasing). Therefore the wavepacket overlaps with one of the regions of regular motion and selective loading can occur. The modulation frequency is chosen to optimize both the overlap between the wavepacket and the region of regular motion, and to make the typical action of a particle small enough to observe quantum effects. After the atoms have interacted with the modulated standing wave for a selected number of modulation periods, the standing wave is turned off with the modulation phase chosen so that the resonance lies on the momentum axis at that time. At that phase (n + 0.25 or 0.75 periods) the atoms, contained inside the region of regular motion, are at the bottom of the well, moving with maximum momentum, $\pm p_0$ (see figure 4). The atomic momentum distribution is measured with absorption imaging after 1.5 ms of free flight. The momentum distribution appears as a set of 'diffraction' peaks at integer multiples of $2\hbar k$ due to the atomic coherence over the multiple wells of the optical lattice.

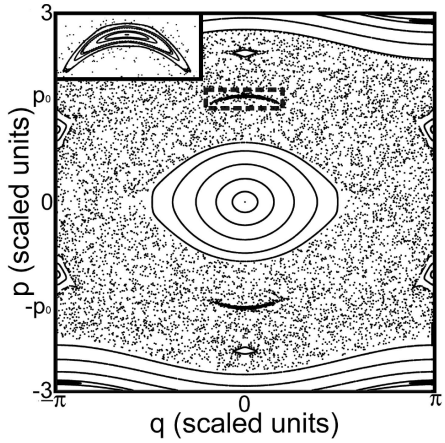

Figure 36. Poincaré section for position q and momentum p of a classical particle in an amplitude modulated optical lattice, for a scaled well depth $\kappa = 1.66$ and a modulation parameter $\varepsilon = 0.29$, showing a mixed phase space. The central region consists of small-amplitude stable motion. Chaos separates this region from two period-1 resonances located above and below the centre along $q = 0$. The upper region of regular motion is magnified in the inset at the top left. Further out in momentum are two stable regions of motion known as librations, which have a period of twice the modulation period. At the edges are bands of regular motion corresponding to above-barrier motion.

9. Dynamical tunnelling

9.1. Introduction

The divergence of quantum and classical descriptions of particle motion is clearly apparent in quantum tunnelling [97, 98] between two regions of classically stable motion. An archetype of such nonclassical motion, studied since the earliest days of quantum mechanics, is tunnelling through an energy barrier. In the 1980s a new kind of tunnelling was predicted. Called dynamical tunnelling [97–100], it involves no potential energy barrier, yet a constant of motion other than energy still classically forbids this quantum-allowed motion. This process should occur, for example, in periodically driven, nonlinear, Hamiltonian systems with one degree of freedom [41, 101, 102]. Such systems may be chaotic and may contain phase space regions of stable, regular motion embedded in a sea of chaos. In 1993 Dyrting *et al* [41] predicted it to occur between such stable regions in the dynamics of cold atoms in an amplitude modulated standing wave. Tunnelling between discrete states is coherent and reversible—that is, the particle oscillates between the states, which is the process described here. Coherent tunnelling oscillations are especially significant, as the system must pass through states corresponding to superpositions of distinct classical motions.

A more intuitive explanation of dynamical tunnelling is given by Heller [103] using the thought experiment of a weightless ball bouncing between two semicircular mirrors. The two mirrors are positioned so that there are two open gaps that would allow the ball to escape from the cavity without it having to tunnel through either of the mirrors (there is no energy barrier preventing it leaving through one of the open gaps). When one follows the classical trajectory of the ball (for example by elementary ray tracing) one finds that its classical trajectory is confined in between the two

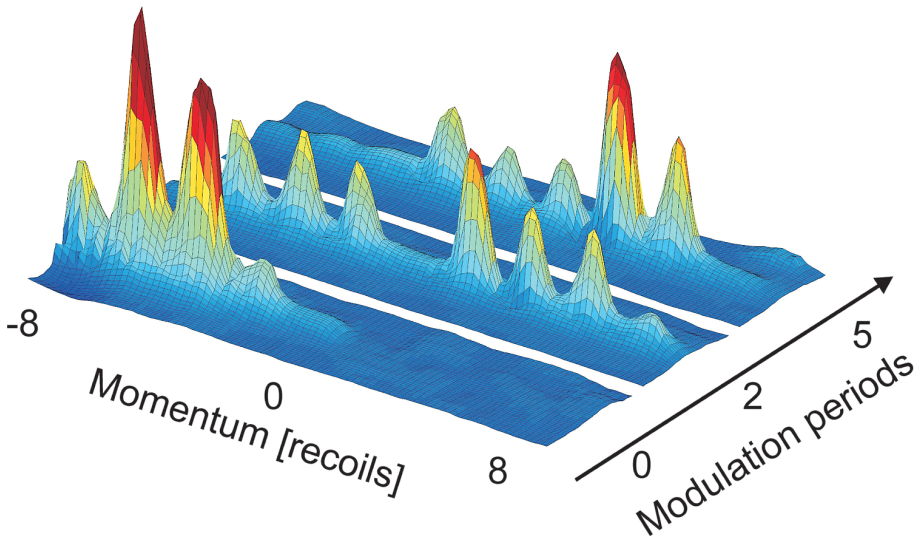

Figure 37. Three atomic momentum distributions of the Bose–Einstein condensate oscillating within the wells of an optical lattice. The pictures are taken after 0.25, 2.25 and 5.25 modulation periods. Classically one would expect most of the atoms to remain in a state with negative momentum, as shown after 0.25 modulation periods. However atoms tunnel into the state with opposite momentum, as shown after 2.25 and 5.25 modulation periods. After 2.25 modulations periods the atoms are in a superposition of two classically distinguishable motions. The results were obtained with a modulation parameter $\varepsilon = 0.29$, scaled well depth $\kappa = 1.66$, modulation frequency $\omega/2\pi = 250$ kHz and a phase shift $\Delta t = 2.68$ ns.

(This figure is in colour only in the electronic version)

mirrors. However, according to quantum mechanics the ball will eventually tunnel out of the cavity as its trajectories can access a classically forbidden region. This is an example of dynamical tunnelling. Dyrting *et al* [41] showed that the system under study here, where particles oscillate in a well, the depth of which is modulated, should also exhibit dynamical tunnelling. A particle oscillates inside the well in phase with the modulation of the well depth and it can tunnel into a motion 180° out of phase with its initial motion.

In this section the observation of dynamical tunnelling of ultra-cold atoms, from a Bose–Einstein condensate, in an amplitude modulated optical standing wave will be described. Atoms tunnel coherently back and forth between their initial state of oscillatory motion (corresponding to an island of regular motion) and the state oscillating 180° out of phase with the initial state. Figure 35 shows a schematic of period-1 resonances of an atom in an amplitude modulated sinusoidal potential. Initially only one region of regular motion is loaded. The appearance of the second ball depicts dynamical tunnelling into the initially empty resonance. T is the modulation period.

9.2. Experiments illustrating dynamical tunnelling

The Poincaré section in figure 36 is plotted for parameters $\kappa = 1.66$ and $\varepsilon = 0.29$ where some of our experiments were conducted. Islands of regular motion (boomerang-shaped rings—see inset) surround period-1 resonances (fixed points) where the atomic motion remains exactly in phase with the modulation. Note that, for small changes in scaled well depth κ and the modulation parameter ε (within the experimental uncertainties), the period-1 regions of regular motion can split into two closely spaced period-2 regions. For initial momentum and position width of the wavepacket reflecting the Heisenberg uncertainty limit in the experiment, such behaviour would be indistinguishable from period-1 motion.

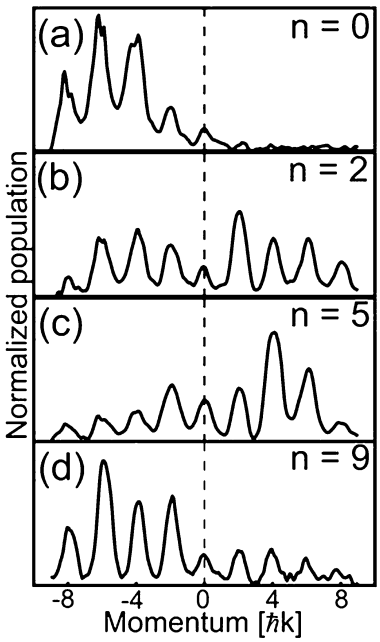

Figure 38. Atomic momentum distributions after $n + 0.25$ modulation periods showing dynamical tunnelling. The parameters for this experiment are $\varepsilon = 0.29$, $\kappa = 1.66$, $\omega/2\pi = 250$ kHz and $\Delta t = 2.68$ ns.

Figure 37 depicts momentum distributions which are taken after 0.25 (front), 2.25 (middle) and 5.25 (back) modulation periods for modulation parameter $\varepsilon = 0.29$, scaled well depth $\kappa = 1.66$, modulation frequency $\omega/2\pi = 250$ kHz and a phase shift of $\Delta t = 2.68$ ns $(0.21 \times 2\pi)$ which was used to selectively load only one region of regular motion. With this value of the modulation frequency $\omega/2\pi$ one obtains a scaled Planck's

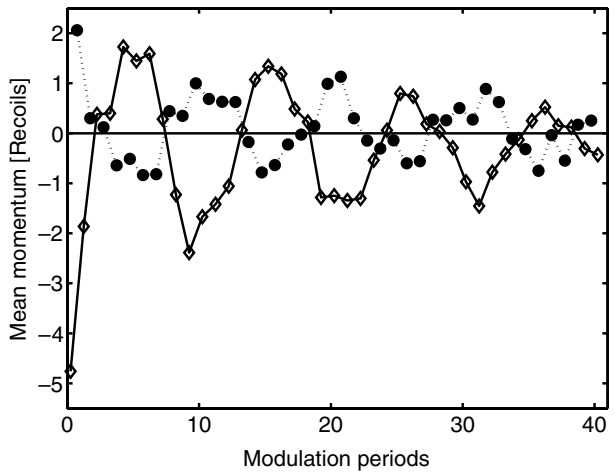

Figure 39. Mean momentum as a function of the interaction time with the modulated standing wave measured in modulation periods, n. The two curves correspond to two different ending phases ($n + 0.25$ (diamonds, solid curve), $n + 0.75$ (circles, dotted curve)) of the modulation (parameters as in figure 38).

constant $\bar{k} = 0.8$. For a more quantitative comparison two-dimensional plots showing atomic momentum distributions for different interaction times with the modulated standing wave are shown in figure 38. To obtain these plots the two-dimensional momentum distribution was integrated over the y coordinate perpendicular to the standing wave. The momentum distribution after 0.25 modulation periods is centred at negative momentum and consists mainly of a pair of diffraction peaks at -4 and $-6\hbar k$. Classically the atoms should remain in the resonance, leaving the stroboscopically measured momentum distribution unchanged. On the contrary, after 2.25 modulation periods about half of the atoms have appeared with opposite momenta, which corresponds to the other resonance. By 5.25 modulation periods most of the atoms are in the other resonance. At 9.25 modulation periods the atoms have returned to the original resonance, as shown in figure 38(d). This transfer of atoms back and forth between the regions of regular motion is dynamical tunnelling.

In figure 39 the mean atomic momentum is plotted after different interaction times with the modulated standing wave measured in modulation periods. The solid curve/diamonds (dotted curve/circles) correspond to turning off the standing wave at the maximum (minimum) of the amplitude modulation (see figure 35 at $t = 0.25T$ and $0.75T$, respectively). Atoms inhabiting only one region of regular motion are at the bottom of the well at both turn-off phases. However, they move in opposite directions for the two different turn-off phases if they are part of a single period-1 island. Classically the mean momentum should approximately remain constant for a given turn-off phase. However, an oscillation of the mean momentum can be observed for each set of data points, indicating the occurrence of dynamical tunnelling. The tunnelling process is coherent as atoms tunnel back and forth between the two states of motion. The period-1 character of the motion is verified by the reversal of the momentum between the full and dotted curves in figure 39, which are separated in time by 0.5 modulation periods. By Fourier transforming the data, the tunnelling period is found to be 10.3(2) modulation periods where the uncertainty is statistical. The period of the tunnelling oscillation agrees well with numerical simulations of the three-dimensional Gross–Pitaevskii equation and Floquet theory within the experimental uncertainty (dominated by the uncertainty in κ). This will be discussed in detail in [62]. Luter and Reichl [104] and Averbukh *et al* [105] have also given a theoretical analysis of the experiments. It should be noted that the mean momenta of the circle and the diamond data points in figure 39 are slightly different for the same number of modulation periods. Classical theory predicts slightly different momenta of the fixed points when viewed at the phases corresponding to figure 35 at $t = 0.25T$ and $0.75T$. The atoms in the region of regular motion have experienced a larger gradient just before the standing wave is turned off at maximum ($t = 0.25T$). Therefore they are slightly faster at that modulation endphase compared to a turn-off at minimum ($t = 0.75T$). This is explained in more detail in section 5.2 and can be seen in the Poincaré section in figure 20.

In figure 40 the atomic momentum distributions corresponding to the solid curve (diamonds) of figure 39 are displayed as a function of the number of modulation periods. Because all atoms start on one side of the potential well, at 0.25 modulation periods essentially all atoms have negative momentum. By 1.25 periods the atoms that were loaded into the chaotic region have begun to spread out, forming a broad background, while the other atoms are bound inside the region of regular motion. For subsequent pictures the coherent oscillation between the two regions of regular motion is evident. One should note that there is no significant (above-background) zero momentum peak even in the case of approximately zero mean momentum (when the atoms have tunnelled halfway). This indicates that at half the tunnel period the system is in a coherent superposition of two distinguishable classical motions: one with positive momenta and one with equal but opposite momenta. This is to be expected, because quantum Floquet analysis shows that atoms tunnel from one region of regular motion into the other and it is impossible for them to enter the central island of stability at $(p, q) = (0, 0)$ (see [62]).

Classical simulations using a Gaussian phase space distribution corresponding to the experimental wavepacket (which is always bigger than the classical region of regular motion) show that, for all experimental conditions, there is no behaviour similar to the observed oscillatory quantum tunnelling.

The decay of the tunnelling oscillations (as can be seen in figure 39) may be due to a number of factors. One likely cause for the decay is spatial variations of κ, which lead to a dephasing of the tunnelling oscillations. The contribution of multiple Floquet states could lead to complicated multi-frequency oscillations, with an envelope for the tunnel oscillations appearing as decay, as observed for some parameters in our simulations. A significantly large initial quasi-momentum width of the initial wavepacket could also explain the decay as the tunnelling frequency is a function of the quasi-momentum as explained in [62]. Another reason for the observed decay could be spontaneous emission. However, the effects of spontaneous emission should be very small on the timescales of the experiments (160 μs). The photon scattering

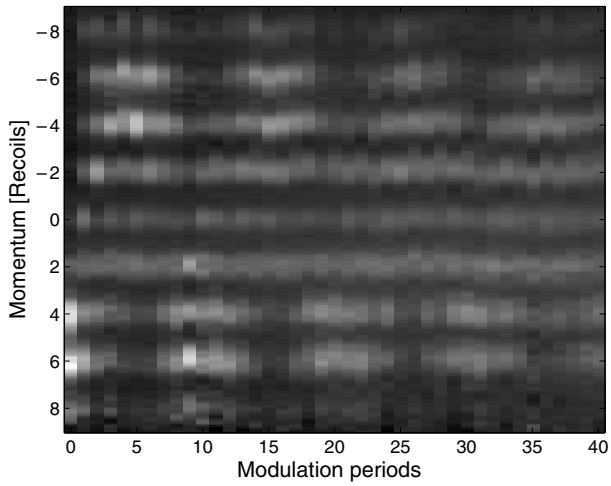

Figure 40. Momentum distributions as a function of the number of modulation periods ($n + 0.25$) showing the tunnelling oscillation between the negative and the positive momentum state. Note that the zero momentum state remains mostly unpopulated, even when the mean momentum is zero. The colour map ranges from black to white for atomic populations ranging from small to large (parameters as in figure 38).

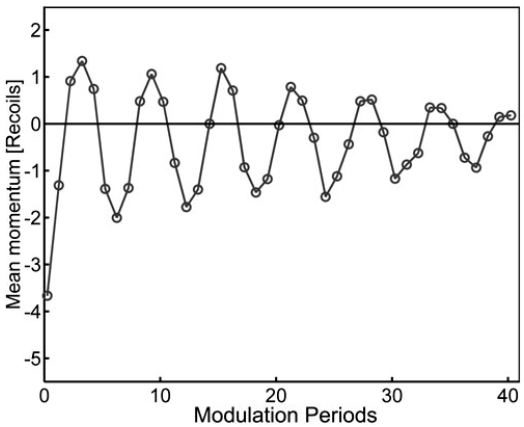

Figure 41. Stroboscopically measured mean momentum as a function of the number of modulation periods ($n + 0.25$) for $\varepsilon = 0.30$, $\kappa = 1.82$, $\omega/2\pi = 222$ kHz and $\Delta t = 2.6$ ns. A tunnelling period of approximately 6 modulation periods is observed.

rate γ_p [48] at the spatial standing wave maximum (for $\varepsilon = 0$) is given by

$$\gamma_p = \frac{1}{\tau}\rho_{ee} = \frac{1}{2\tau}\frac{I}{I + I_{\text{sat}}(1 + 4\delta^2\tau^2)} = 2.32 \times 10^3 \text{ Hz} \quad (79)$$

where τ is the spontaneous lifetime in the excited state, ρ_{ee} is the excited state element of the density matrix, I is the light intensity, δ is the detuning and I_{sat} is the saturation intensity. For this calculation typical experimental parameters were chosen ($\kappa = 1.66$, $I = 6.37 \times 10^4$ W m^{-2} and $I_{\text{sat}} = 110$ W m^{-2}). Atom–atom interactions should also be small (mean field ≈ 400 Hz) on relevant timescales (kinetic energy $\sim 10^5$ Hz).

Quantum theory predicts dynamical tunnelling to occur for various values of the scaled well depth κ, the modulation parameter ε and modulation frequency ω and also predicts

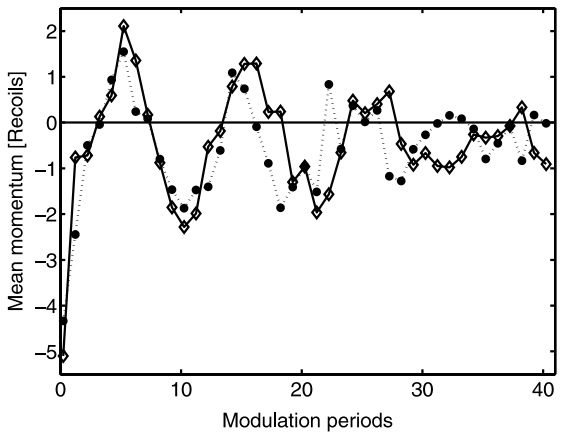

Figure 42. Stroboscopically measured mean momentum as a function of the number of modulation periods ($n + 0.25$) for two sets of parameters. The dotted curve (circles) is plotted for $\varepsilon = 0.28$, $\kappa = 1.66$, $\omega/2\pi = 250$ kHz and $\Delta t = 2.8$ ns and the solid curve (diamonds) is plotted for the same parameters but with a scaled well depth $\kappa = 1.49$. When the scaled well depth κ is decreased the tunnelling period actually increases.

a strong sensitivity of the tunnelling period and amplitude on these parameters. As shown in figure 41, for $\varepsilon = 0.30$, $\kappa = 1.82$, $\omega/2\pi = 222$ kHz and $\Delta t = 2.6$ ns a tunnelling period of 6 modulation periods with a significantly longer decay time than in figure 39 is found. With this value of the modulation frequency $\omega/2\pi$ one obtains a scaled Planck's constant $\bar{k} = 0.9$. In figure 42 the dotted curve (circles) is plotted for $\varepsilon = 0.28$, $\kappa = 1.66$ and $\omega/2\pi = 250$ kHz, $\Delta t = 2.8$ ns and the solid curve (diamonds) is plotted for the same parameters but with the scaled well depth $\kappa = 1.49$. Surprisingly an increase in the tunnelling period is observed when κ is decreased and when all other parameters are held constant. This is the opposite of what one would expect for spatial, barrier tunnelling. Theoretical simulations [62] show the same result and the physics behind this phenomenon will be discussed in [62]. To obtain the black curve all parameters are held constant and the light intensity is reduced.

10. Conclusion and outlook

The driven pendulum in atom optics is an ideal environment to explore quantum nonlinear dynamics. The dynamics can be qualitatively well described by classical theory provided that the experimental timescales and the scaled Planck's constant of the system are sufficiently small. This follows from the thorough experimental investigation of the dynamics of the driven pendulum in atom optics which was carried out and described in this tutorial. However, the observation of dynamical tunnelling illustrates a dramatic divergence of quantum and classical physics. By varying the Hamiltonian parameters and the initial conditions dynamical tunnelling was observed for a variety of mixed phase space configurations. Due to the ability to control the scaled Planck's constant the atom-optics-driven pendulum provides an effective means to explore the borderland between quantum and classical physics and the experiments illustrate that one needs to consider the wave nature of atoms to accurately explain the atomic dynamics, especially for large experimental timescales and a large scaled Planck's constant.

This tutorial presents experimental results and theoretical techniques pertaining to the atom-optics-driven pendulum. The parameter space that determines the observed phase space dynamics was characterized. The origin of distinct peaks in the atomic momentum distribution was explained and it was shown how to obtain these peaks experimentally. Experimental evidence is presented for how the size and amplitude of the regions of regular motion depends on the modulation frequency ω, the scaled well depth κ, the modulation parameter ε and the scaled Planck's constant $\bar{k}$ of the system. The experimental system which is described here can be described by a truly two-dimensional phase space spanned by position and momentum along the standing wave. Experimental proof is presented that the atom-optics-driven pendulum can be accurately modelled by quantum trajectory theory. Chaotic transients of the driven pendulum are investigated. The momenta of the resulting peaks in the atomic momentum distribution scale linearly with the modulation frequency ω. Phase space resonances and chaotic transients provide new ways to manipulate atoms. Experimental methods were developed in which the momentum of an ensemble of atoms can be controlled very accurately and experimental results were presented illustrating this. It was shown that the quantum chaotic mixed phase space provides a range of possibilities for effective quantum phase space preparation. It was illustrated that up to approximately 65% of all atoms can be loaded into distinct peaks in the atomic momentum distribution, allowing efficient atomic momentum control. The results presented here could be useful for atom interferometry, splitting of a Bose–Einstein condensate and other areas of atom optics. A bifurcation sequence was mapped and explained using classical perturbation theory for the relevant nonlinear Hamiltonian. The experimental results are in good agreement with the theoretical predictions of classical perturbation theory, highlighting that the dynamics of the driven pendulum can be described by classical perturbation theory as long as the experimental timescales and Planck's constant are sufficiently small. The mapping of the atomic momentum distributions to the bifurcation diagram was confirmed by measuring the rotation frequency of the regions of regular motion from which the distinct peaks in the atomic momentum distribution result. The experimentally measured resonance momenta agree well with the quantum simulations. However, they are significantly slower than the classical prediction. This behaviour could be linked to quantum slow motion but more experiments will be needed to confirm that. When the scaled Planck's constant of the system becomes sufficiently large, one can use the dynamics of the driven pendulum in atom optics to observe dynamical tunnelling between two macroscopically distinguishable states of motion. This was illustrated using a Bose–Einstein condensate. The observed tunnelling process is coherent and multiple full tunnelling oscillations are observed which are centred at approximately zero mean momentum. The tunnelling amplitude and frequency is found to be sensitive to the scaled well depth κ, the modulation parameter ε and the scaled Planck's constant $\bar{k}$ of the system as predicted by quantum theory.

What are the future directions for the experiments presented in this tutorial? Although the driven pendulum is found to be not very sensitive to amplitude noise (small noise amplitudes) the effects of large noise amplitudes have not been thoroughly explored yet and could be subject of further study. Different types of noise, for example phase noise and spontaneous emission leading to random kicks, could be investigated. A more comprehensive measurement and analysis of the resonance momenta could test the theory of quantum slow motion. The experiments could be extended to include two-dimensional potentials about which little is known in both the classical and the quantum domain. The observation of dynamical tunnelling of atoms in a modulated standing wave opens the door to further studies in quantum nonlinear dynamics. A thorough scan of the scaled Planck's constant in the dynamical tunnelling experiments combined with detailed theoretical analysis could help to better understand the quantum–classical transition. By carefully following the evolution of wavepackets loaded into the chaotic region from a Bose–Einstein condensate, 'quantum chaos' can be probed with the unprecedented resolution afforded by minimum uncertainty wavepackets. By introducing decoherence in a controlled manner, one can systematically investigate the role of decoherence in dynamical tunnelling and explore the classical limit of chaotic systems. Decoherence plays an integral role in the classical behaviour of most systems and its role in highly nonlinear dynamical systems is still unclear. It can be introduced in different ways into the driven-pendulum experiments by the addition of specific noise to the modulation of the optical standing wave or by changing the detuning of the standing wave increasing the amount of spontaneous emission and therefore producing random recoil kicks on the atoms. Furthermore, when utilizing a Bose–Einstein condensate decoherence can be introduced using mean-field interactions and incoherent collisions by using a denser condensate. Ultimately, it will be possible to test whether the introduction of decoherence into a system is equivalent to approaching the limit of Planck's constant going to zero (with classical noise) and methods can be developed to control decoherence in nonlinear quantum systems.

Acknowledgments

Antoine Browaeys, Hartmut Häffner, Kristian Helmerson, Cathy Holmes, Callum McKenzie, William D Phillips, Steven Rolston, Andrew Truscott, Ben Upcroft and Howard Wiseman significantly contributed to the research which has been presented in this tutorial. Some of the results that are discussed in this tutorial have been published previously in a more compressed form in [88, 106–109]. The dynamical tunnelling experiments have been carried out at the National Institute of Standards and Technology in Gaithersburg, USA. The corresponding author (WKH) would like to thank NIST for their hospitality.

References

[1] Reichl L E 1992 *The Transition to Chaos: in Conservative Classical Systems: Quantum Manifestations* (Berlin: Springer)
[2] Einstein A 1917 Zum Quantensatz von Sommerfeld und Epstein *Verh. Dtsch. Phys. Ges.* **19** 82
[3] Berry M V 1987 Quantum chaology *Proc. R. Soc.* A **413** 183–98

[4] Nakamura K 1997 *Quantum versus Chaos, Questions Emerging from Mesoscopic Cosmos* (Dordrecht: Kluwer)
[5] Zurek W H 2001 Sub-Planck structure in phase space and its relevance for quantum decoherence *Nature* **412** 712–17
[6] Gutzwiller M C 1970 Energy spectrum according to classical mechanics *J. Math. Phys.* **11** 1791–806
[7] Bohigas O 1991 *Chaos and Quantum Physics* (Amsterdam: Elsevier)
[8] Bohigas O, Giannoni M J and Schmit C 1984 Characterization of chaotic quantum spectra and universality of level fluctuation laws *Phys. Rev. Lett.* **52** 1–4
[9] Guhr T, Müller-Groeling A and Weidenmüller H A 1998 Random-matrix theories in quantum physics: common concepts *Phys. Rep.* **299** 189–425
[10] Mehta M L 1991 *Random Matrices and the Statistical Theory of Energy Levels* 2nd edn (San Diego, CA: Academic)
[11] Fishman S, Grempel D R and Prange R E 1982 Chaos, quantum recurrences and Anderson localization *Phys. Rev. Lett.* **49** 509–12
[12] Marcus C M, Rimberg A J, Westervelt R M, Hopkins P F and Gossard A C 1992 Conductance fluctuations and chaotic scattering in ballistic microstructures *Phys. Rev. Lett.* **69** 506–9
[13] Blumel R, Fishman S and Smilansky U 1986 Excitation of molecular rotation by periodic microwave pulses. A testing ground for Anderson localization *J. Chem. Phys.* **84** 2604–16
[14] Richter A 2001 Wave dynamical chaos: an experimental approach in billiards *Phys. Scr.* T **90** 212–22
[15] Sridhar S 1991 Experimental observation of scarred eigenfunctions of chaotic microwave cavities *Phys. Rev. Lett.* **67** 785–8
[16] Lin W A and Ballentine L E 1990 Quantum tunnelling and chaos in a driven anharmonic oscillator *Phys. Rev. Lett.* **65** 2927–30
[17] Tomsovic S and Ullmo D 1994 Chaos-assisted tunneling *Phys. Rev.* E **50** 145–62
[18] Dembowski C, Gräf H-D, Heine A, Hofferbert R, Rehfeld H and Richter A 2000 First experimental evidence for chaos-assisted tunneling in a microwave annular billiard *Phys. Rev. Lett.* **84** 867–70
[19] Frischat S D and Doron E 1998 Dynamical tunnelling in mixed systems *Phys. Rev.* E **57** 1421–43
[20] Latka M, Grigolini P and West B J 1994 Chaos-induced avoided level crossing and tunneling *Phys. Rev.* A **50** 1071–81
[21] Mouchet A, Miniatura C, Kaiser R, Grémaud B and Delande D 2001 Chaos-assisted tunneling with cold atoms *Phys. Rev.* E **64** 016221
[22] Bayfield J E and Koch P M 1974 Multiphoton ionisation of highly excited hydrogen atoms *Phys. Rev. Lett.* **33** 258–661
[23] Jensen R V, Susskind S M and Sanders M M 1991 Chaotic ionization of highly excited hydrogen atoms: comparison of classical and quantum theory with experiment *Phys. Rep.* **201** 1–56
[24] Timp G, Behringer E, Tennant D M and Cunningham J E 1992 Using light as a lens for submicron, neutral-atom lithography *Phys. Rev. Lett.* **69** 1636
[25] Adams C S, Sigel M and Mlynek J 1994 Atom optics *Phys. Rep.* **240** 143–210
[26] Anderson B P and Kasevich M A 1998 Macroscopic quantum interference from atomic tunnel arrays *Science* **283** 1686–9
[27] Wilkinson S R, Bharucha C F, Madison K W, Niu Q and Raizen M G 1996 Observation of atomic Wannier–Stark ladders in an accelerating optical potential *Phys. Rev. Lett.* **76** 4512–5
[28] Deutsch I H and Jessen P S 1998 Quantum-state control in optical lattices *Phys. Rev.* A **57** 1972–86
[29] Deutsch I H, Alsing P M, Grondalski J, Gose S, Haycock D L and Jessen P S 2000 Quantum transport in magneto-optical double-potential wells *J. Opt. B: Quantum Semiclass. Opt.* **2** 633–44
[30] Deutsch I H, Brennen G K and Jessen P S 2000 Quantum computing with neutral atoms in an optical lattice *Fortschr. Phys.* **48** 925–43
[31] Milburn G J 2000 Quantum computing using a neutral atom optical lattice: an appraisal *Fortschr. Phys.* **48** 957–64
[32] Greiner M, Mandel O, Esslinger T, Hänsch T W and Bloch I 2002 Quantum phase transition from a superfluid to a mott insulator in a gas of ultracold atoms *Nature* **415** 39–44
[33] Graham R, Schlautmann M and Zoller P 1992 Dynamical localization of atomic-beam deflection by a modulated standing light wave *Phys. Rev.* A **45** R19–22
[34] Moore F L, Robinson J C, Bharucha C, Williams P E and Raizen M G 1994 Observation of dynamical localization in atomic momentum transfer: a new testing ground for quantum chaos *Phys. Rev. Lett.* **73** 2974–7
[35] Moore F L, Robinson J C, Bharucha C F, Sundaram B and Raizen M G 1995 Atom optics realization of the quantum δ-kicked rotor *Phys. Rev. Lett.* **75** 4598–601
[36] Robinson J C, Bharucha C, Jahnke R, Georgakis G A, Raizen M G, Niu Q and Sundaram Bala 1995 Study of quantum dynamics in the transition from classical stability to chaos *Phys. Rev. Lett.* **74** 3963–6
[37] Robinson J C, Bharucha C F, Madison K W, Moore F L, Sundaram Bala, Wilkinson S R and Raizen M G 1996 Can a single-pulse standing wave induce chaos in atomic motion? *Phys. Rev. Lett.* **76** 3304–7
[38] Ammann H, Gray R, Shvarchuck I and Christensen N 1998 Quantum delta-kicked rotor: experimental observation of decoherence *Phys. Rev. Lett.* **80** 4111–15
[39] Klappauf B G, Oskay W H, Steck D A and Raizen M G 1998 Observation of noise and dissipation effects on dynamical localization *Phys. Rev. Lett.* **81** 1203–6
[40] Ghose S, Alsing P M and Deutsch I H 2001 Atomic motion in magneto-optic double-well potentials: a testing ground for quantum chaos *Phys. Rev.* E **64** 056119
[41] Dyrting S, Milburn G J and Holmes C A 1993 Nonlinear quantum dynamics at a classical second order resonance *Phys. Rev.* E **48** 969–78
[42] Arnold V I 1979 *Mathematical Methods of Classical Mechanics* (New York: Springer)
[43] Lichtenberg A J and Liebermann M A 1988 Regular stochastic motion *Applied Mathematical Sciences* vol 38 (New York: Springer)
[44] Hug M and Milburn G J 2001 Quantum slow motion *Phys. Rev.* A **63** 023413
[45] Truscott A 1998 Trapping and cooling rubidium atoms using stabilised diode lasers *PhD Thesis* The University of Queensland
[46] Yu J, Gagne C M, Valentine C, Yuan R L and Pillet P 1992 Narrowband frequency control of an injection-locked diode laser battery *J. Physique* **2** 1615–22
[47] Truscott A G, Heckenberg N R and Rubinsztein-Dunlop H 1999 Frequency stabilised grating feedback laser diode for atom cooling applications *Opt. Quantum Electron.* **31** 417–30
[48] Metcalf H J and van der Straten P 1999 *Laser Cooling and Trapping* (New York: Springer)
[49] Savage C 1996 Introduction to light forces, atom cooling, and atom trapping *Aust. J. Phys.* **49** 745–64
[50] Truscott A G, Baleva D, Heckenberg N R and Rubinsztein-Dunlop H 1998 Short-term diffusion in σ^+–σ^- optical molasses *Opt. Commun.* **145** 81–5
[51] Hilborn R C 1994 *Chaos and Nonlinear Dynamics* (New York: Oxford University Press)
[52] Sinclair R M, Hosea J C and Sheffield G V 1970 A method for mapping a toroidal magnetic field by storage of phase stabilized electrons *Rev. Sci. Instrum.* **41** 1552–9

[53] Chaiken J, Chevray R, Tabor M and Tan Q M 1986 Experimental study of Lagrangian turbulence in a Stokes flow *Proc. R. Soc.* A **408** 165–74
[54] Bayfield J E and Sokol D S 1988 Excited atoms in strong microwaves: classical resonances and localization in experimental final-state distributions *Phys. Rev. Lett.* **61** 2007–10
[55] Zurek W H 1998 Decoherence, chaos, quantum-classical correspondence, and the algorithmic arrow of time *Phys. Scr.* T **76** 186–98
[56] Zurek W H 2001 Decoherence, einselection, and the quantum origins of the classical *Preprint* quant-ph/0105127
[57] Habib S, Shizume K and Zurek W H 1998 Decoherence, chaos and the correspondence principle *Phys. Rev. Lett.* **80** 4361–5
[58] Lindblad G 1976 On the generators of quantum dynamical semigroups *Commun. Math. Phys.* **48** 119–30
[59] Dyrting S and Milburn G J 1995 Dissipative nonlinear quantum dynamics in atom optics *Phys. Rev.* A **51** 3136–47
[60] Warszawski P and Wiseman H M 2001 Adiabatic elimination in compound quantum systems with feedback *Phys. Rev.* A **63** 013803
[61] Atkins D J, Wiseman H M and Warszawski P 2003 Approximate master equations for atom optics *Phys. Rev.* A **67** 023802 (*Preprint* quant-ph/0204074)
[62] Hensinger W K, Mouchet A, Julienne P S, Delande D, Heckenberg N R and Rubinsztein-Dunlop H 2003 Analysis of dynamical tunnelling experiments with a Bose–Einstein condensate, in preparation
[63] Ball G H, Vant K M D, Ammann H and Christensen N L 1999 A study of quantum decoherence via spontaneous emission in a system with Kolmogorov–Arnol'd–Moser tori *J. Opt. B: Quantum Semiclass. Opt.* **1** 357–63
[64] Charmichael H J 1993 *An Open Systems Approach to Quantum Optics* (Berlin: Springer)
[65] Dum R, Zoller P and Ritch H 1992 Monte carlo simulation of atomic master equation for spontaneous emission *Phys. Rev.* A **45** 4879–87
[66] Mølmer K, Castin Y and Dalibard J 1993 Monte Carlo wavefunction method in quantum optics *J. Opt. Soc. Am.* B **10** 524–38
[67] Feit M D, Fleck J A Jr and Steiger A 1982 Solution of the Schrödinger equation by a spectral method *J. Comput. Phys.* **47** 412–33
[68] Tan S M and Walls D F 1994 Quantum effects in atomic reflection *J. Physique* **4** 1897–912
[69] Ruth R D 1983 A canonical integration technique *IEEE Trans. Nucl. Sci.* **30** 2669–71
[70] Forest E and Berz M 1989 *Canonical Integration and Analysis of Periodic Maps using Non-Standard Analysis and Lie Methods* (Berlin: Springer)
[71] Dyrting S 1994 Quantum chaos in atom optics *PhD Thesis* The University of Queensland
[72] Goetsch P and Graham R 1996 Decoherence by spontaneous emission in atomic-momentum transfer experiments *Phys. Rev.* A **54** 5345–8
[73] Steck D A, Milner V, Oskay W H and Raizen M G 2000 Quantitative study of amplitude noise effects on dynamical localization *Phys. Rev.* E **62** 3461
[74] de Aguiar M A M, Malta C P, Baranger M and Davises K T R 1987 Bifurcations of periodic trajectories in non-integrable hamiltonian systems with two degrees of freedom: numerical and analytical results *Ann. Phys., NY* **180** 167
[75] Mao J-M, Rapelje K A, Blodgett-Ford S J, Delos J B, König A and Rinneberg H 1993 Photoabsorption spectra of atoms in parallel electric and magnetic fields *Phys. Rev.* A **48** 2117–26
[76] Main J, Wiebusch G, Welge K, Shaw J and Delos J B 1994 Recurrence spectroscopy: observation and interpretation of large-scale structure in the absorption spectra of atoms in magnetic fields *Phys. Rev.* A **49** 847–68
[77] Keith D W, Ekstrom C R, Turchette Q A and Pritchard D E 1991 An interferometer for atoms *Phys. Rev. Lett.* **66** 2693–6
[78] Gerlach W and Stern O 1922 Der experimentelle Nachweis der Richtungsquantelung im Magnetfeld *Z. Phys.* **9** 349
[79] Keith D W, Schattenburg M L, Smith H I and Pritchard D E 1988 Diffraction of atoms by a transmission grating *Phys. Rev. Lett.* **61** 1580–3
[80] Gould P L, Ruff G A and Pritchard D E 1986 Diffraction of atoms by light: the near-resonant Kapitza–Dirac effect *Phys. Rev. Lett.* **56** 827–30
[81] Moskowitz P E, Gould P L, Atlas S R and Pritchard D E 1983 Diffraction of an atomic beam by standing-wave radiation *Phys. Rev. Lett.* **51** 370–3
[82] Oberthaler M K, Abfalterer R, Bernet S, Keller C, Schmiedmayer J and Zeilinger A 1999 Dynamical diffraction of atomic matter waves by crystals of light *Phys. Rev.* A **60** 456–72
[83] Hajnal J V and Opat G I 1989 Diffraction of atoms by a standing evanescent light wave—a reflection grating for atoms *Opt. Commun.* **73** 119–24
[84] Ovchinnikov Y B, Müller J H, Doery M R, Vredenbregt E J D, Helmerson K, Rolston S L and Phillips W D 1999 Diffraction of a released Bose–Einstein condensate by a pulsed standing light wave *Phys. Rev. Lett.* **83** 284–7
[85] Kozuma M, Deng L, Hagley E W, Wen J, Lutwak R, Helmerson K, Rolston S L and Phillips W D 1999 Coherent splitting of Bose–Einstein condensed atoms with optically induced Bragg diffraction *Phys. Rev. Lett.* **82** 871–5
[86] Steane A, Szriftgiser P, Desbiolles P and Dalibard J 1995 Phase modulation of atomic de Broglie waves *Phys. Rev. Lett.* **74** 4972–5
[87] Szriftgiser P, Guéry-Odelin D, Arndt M and Dalibard J 1996 Atomic wave diffraction and interference using temporal slits *Phys. Rev. Lett.* **77** 4–7
[88] Truscott A G, Friese M E J, Hensinger W K, Wiseman H M, Rubinsztein-Dunlop H and Heckenberg N R 2000 Coherent atomic beam splitter using transients of a chaotic system *Phys. Rev. Lett.* **84** 4023–6
[89] Denschlag J H, Simsarian J E, Häffner H, McKenzie C, Browaeys A, Cho D, Helmerson K, Rolston S L and Phillips W D 2002 A Bose–Einstein condensate in an optical lattice *J. Phys. B: At. Mol. Opt. Phys.* **35** 3095–110
[90] Steck D A, Oskay W H and Raizen M G 2001 Observation of chaos-assisted tunneling between islands of stability *Science* **293** 274–8
[91] Kasevich M, Weiss D S, Riis E, Moler K, Kasapi S and Chu S 1991 Atomic velocimetry selection using stimulatedRamantransitions *Phys. Rev. Lett.* **66** 1542–5
[92] Anderson M H, Ensher J R, Matthews M R, Wieman C E and Cornell E A 1995 Observation of Bose–Einstein condensation in a dilute atomic vapor *Science* **269** 198–201
[93] Davis K B, Mewes M O, Andrews M R, van Druten N J, Durfee D S, Kurn D M and Ketterle W 1995 Bose–Einstein condensation in a gas of sodium atoms *Phys. Rev. Lett.* **75** 3969–73
[94] Ketterle W, Davis K B, Joffe M A, Martin A and Pritchard D E 1993 High densities of cold atoms in a dark spontaneous-force optical trap *Phys. Rev. Lett.* **70** 2253–6
[95] Petrich W, Anderson M H, Ensher J R and Cornell E A 1995 Stable, tightly confining magnetic trap for evaporative cooling of neutral atoms *Phys. Rev. Lett.* **74** 3352–5
[96] Ashcroft N W and Mermin N D 1976 *Solid State Physics* (Philadelphia, PA: Saunders)

[97] Caldeira A O and Leggett A J 1983 Quantum tunneling in a dissipative system *Ann. Phys., NY* **149** 374–456
[98] Tomsovic S 2001 Tunneling and chaos *Phys. Scr.* T **90** 162–5
[99] Davis M J and Heller E J 1981 Quantum dynamical tunneling in bound states *J. Chem. Phys.* **75** 246–54
[100] Heller E J 1999 The many faces of tunneling *J. Phys. Chem.* A **103** 10433–44
[101] Haake F, Kus M and Scharf R 1987 Classical and quantum chaos for a kicked top *Z. Phys.* B **77** 497–510
[102] Sanders B C and Milburn G J 1989 The effect of measurement on the quantum features of a chaotic system *Z. Phys.* B **77** 497–510
[103] Heller E J 2001 Air juggling and other tricks *Nature* **412** 33–4
[104] Luter R and Reichl L E 2002 Floquet analysis of atom-optics tunneling experiments *Phys. Rev.* A **66** 053615
[105] Averbukh V, Osovski S and Moiseyev N 2002 Controlled tunneling of cold atoms: from full suppression to strong enhancement *Phys. Rev. Lett.* **89** 253201
[106] Hensinger W K, Truscott A G, Upcroft B, Heckenberg N R and Rubinsztein-Dunlop H 2000 Atoms in an amplitude-modulated standing wave—dynamics and pathsways to quantum chaos *J. Opt. B: Quantum Semiclass. Opt.* **2** 659–67
[107] Hensinger W K, Upcroft B, Milburn G J, Heckenberg N R and Rubinsztein-Dunlop H 2001 Multiple bifurcations in atom optics *Phys. Rev.* A **64** 063408
[108] Hensinger W K, Truscott A G, Upcroft B, Hug M, Wiseman H M, Heckenberg N R and Rubinsztein-Dunlop H 2001 Experimental study of the quantum driven pendulum and its classical analogue in atom optics *Phys. Rev.* A **64** 033407
[109] Hensinger W K, Häffner H, Browaeys A, Heckenberg N R, Helmerson K, McKenzie C, Milburn G J, Phillips W D, Rolston S L, Rubinsztein-Dunlop H and Upcroft B 2001 Dynamical tunneling of ultra-cold atoms *Nature* **412** 52–5